Electronic Thesis and Dissertation Repository

6-25-2018 9:00 AM

The Development of a Temporomandibular Force Simulator to Study Craniofacial Strain In-Vitro

Kenneth KC Ip
The University of Western Ontario

Supervisor
Ferreira, Louis M.
The University of Western Ontario Joint Supervisor
Moore, Corey C.
The University of Western Ontario

Graduate Program in Biomedical Engineering
A thesis submitted in partial fulfillment of the requirements for the degree in Master of Engineering Science
© Kenneth KC Ip 2018

Follow this and additional works at: https://ir.lib.uwo.ca/etd

 Part of the Biomechanics and Biotransport Commons, Musculoskeletal Diseases Commons, and the Other Medical Specialties Commons

Abstract

An in-vitro musculoskeletal loading simulator was developed to replicate the internal forces of mastication, and then employed in a comparison of clinically relevant facial fracture repairs. Muscle forces are simulated by pneumatic pistons via 3D printed mounts that are reverse-engineered from CT scan to match muscle attachment sites, which are adhered to bone in order to simulate native stress distributions. Bite force and bone strain pattern of the craniofacial structure under load were measured using a force sensor and strain gauges respectively. In a series of five fresh-frozen cadaveric heads, it was found that strain patterns of the craniofacial structure were different between internal and external loading. In a zygomatic complex fracture with an intact zygomatic arch, an infraorbital rim plate made no difference in strain pattern. However, with a fractured arch, a repair done without an infraorbital rim plate better restored the strain pattern of an intact craniofacial structure.

Keywords: mastication, in-vitro simulator, craniofacial, biomechanics, strain, muscle loading, zygomatic complex fracture

Co-Authorship Statement

Chapter 1:   Kenneth Ip – manuscript preparation

Corey Moore – manuscript review

Louis Ferreira – manuscript review

Chapter 2:   Kenneth Ip – study design, data collection, manuscript preparation

Peng You – study design, data collection

Yara Hosein – study design

Corey Moore – study design, manuscript review

Louis Ferreira – study design, manuscript review

Chapter 3:   Kenneth Ip – statistical analysis, manuscript preparation

Corey Moore – manuscript review

Louis Ferreira – manuscript review

Chapter 4:   Kenneth Ip – manuscript preparation

Nikolas Knowles – manuscript review

Corey Moore – manuscript review

Louis Ferreira – manuscript review

Acknowledgements

I would like to thank both my supervisors, Dr. Louis Ferreira and Dr. Corey Moore, for their guidance throughout my graduate studies. Dr. Ferreira, your enthusiasm filled the lab with energy and your experience kept me on the right track. Dr. Moore, you set an example through your open-hearted mentorship in the lab, clinic, and OR. Your talent, diligence, and humbleness inspired me to be a better student.

Dr. Peng You, I will never forget the many Sundays we spent in the lab; I deeply appreciate your hard work and patience. Team HULC, I am grateful for your help and companionship on this journey.

Without the gracious gifts from those who donated their bodies, the in-vitro work presented here would never have been possible. Thank you for the precious opportunity to learn through your legacy.

To my family: Mom, Dad, and Kat, thank you for your unconditional love and support.

Table of Contents

List of Tables

List of Figures

List of Appendices

Chapter 1

1   Background

1.1   Anatomy of the Human Masticatory System

1.1.1 Introduction

The human masticatory system is comprised of bones, muscles, ligaments, and articular capsules. Like in orthopedic biomechanics, performing in-vitro experimental research can increase our understanding of the human masticatory system. Forces generated by such complex systems are poorly understood. In addition, current research on diseases, implants, and appliances in otorhinolaryngology, as well as in the oral and maxillofacial domain, rely on the accuracy of a physical simulator to replicate clinically relevant forces expected in the human masticatory system. This project aims to develop a biomechanical simulator that can reproduce physiological muscle loads in the masticatory system and to employ it to study a clinically relevant model of fracture treatment.

1.1.2 Craniofacial Structure

The human skull is made up of the neurocranium (braincase) and the viscerocranium (facial skeleton). The braincase consists of eight bones jointed together with sutures; it provides mechanical protection for the brain and brain stem. The facial skeleton provides structural support to the face. It consists of 12 bones, all jointed together with sutures except for the mandible (jaw). The mandible is allowed to move about the temporomandibular joints.

1.1.3 Temporomandibular Joint (TMJ)

The temporomandibular joint (TMJ) is the only bilateral joint in the human body. The mandible is connected to the sides of the cranium via these joints. It allows three-dimensional motion of the mandible with six degrees of freedom; the mandible can both rotate and translate about the TMJ. The joint is encapsulated and an articular disc, the TMJ disc, rests between the articulating surfaces.

The mandible has three main movements. Elevation and depression of the mandible correspond to its closing and opening, respectively. Protrusion and retraction correspond to the forward and rearward movement of the mandible. Lastly, laterotrusion is the side-to-side movement of the mandible.

1.1.4 Midface Buttress

Bones in the midface form a thin-walled, light weight structure that directs and dissipates loads in the facial skeleton. It is theorised that these loads are transmitted through vertical, horizontal, and sagittal buttresses in the midface, which are areas with increased bone thickness. There are three main vertical buttresses (pillars), and they are the anterior medial naso-maxillary buttress, lateral zygomatico-maxillary buttress, and posterior pterygo-maxillary buttress (Hardt &Kuttenberger, 2010). These three vertical buttresses transmit masticatory loads from the facial skeleton to the neurocranium (Figure 1A). Horizontal buttresses provide support for vertical buttresses in resisting buckling loads (Figure 1B). The three main horizontal buttresses are the supraorbital-frontal, infraorbital, and alveolar buttresses.

A)

Anterior Medial Naso-Maxillary Buttress

Lateral Zygomatico-Maxillary Buttress

Posterior Pterygo-Maxillary Buttress

B)

Supraorbital-Frontal Buttress

Infraorbital Buttress

Alveolar Buttress
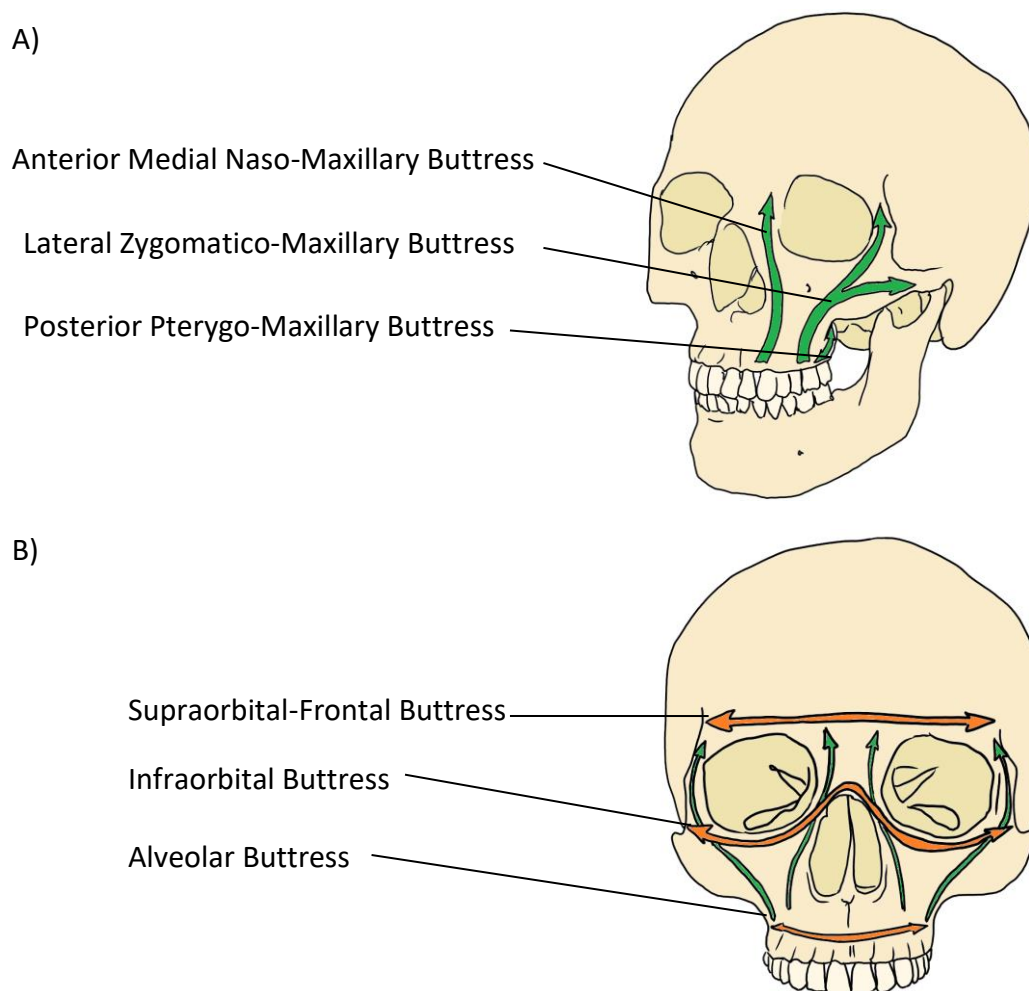
Figure 1. Buttresses in the midface (Hardt &Kuttenberger, 2010)**. A) Vertical buttresses. B) Horizontal buttresses.**

1.1.5 Zygomatic Complex Fracture

Fracture in the midface represents a significant portion in trauma cases (Ozkaya et al., 2009). Zygomatic complex fracture is one of the most common fractures in the midface (Bogusiak &Arkuszewski, 2010; Erdmann et al., 2008). This type of fracture typically results from assaults and motor vehicle accidents, and is more prevalent in males than in females (Ozkaya et al., 2009). Zygomatic complex fracture involves the zygoma and its surrounding bones: frontal, temporal, and maxilla. These fractures commonly occur at suture lines between these bones, which are the zygomaticomaxillary suture, zygomaticofrontal suture, and the zygomaticotemporal suture (Figure 2). In addition,

zygomatic complex fractures often occur in combination with other types of midface fractures (Erdmann et al., 2008), which increase the complexity and difficulty of repair. Although there is no consensus on a universal classification system, sub-types of zygomatic complex fracture are typically classified by the locations of fractures and whether a fracture is displaced (Hwang &Kim, 2011; Knight, Ph, North, &Chir, 1961; Kristensen &Tveterås, 1986; Zingg et al., 1992). In a dipod fracture, two of the three connections between the zygoma and its neighbouring bone are displaced; in a tripod fracture, all three connections are displaced.

The two sub-types of zygomatic complex fracture that will be investigated are the type 1 and type 2 fracture (Figure 3). The type 1 fracture is a dipod fracture where the zygomaticofrontal and zygomaticomaxillary sutures are fractured. The type 2 fracture is a tripod fracture where all three connections are fractured.
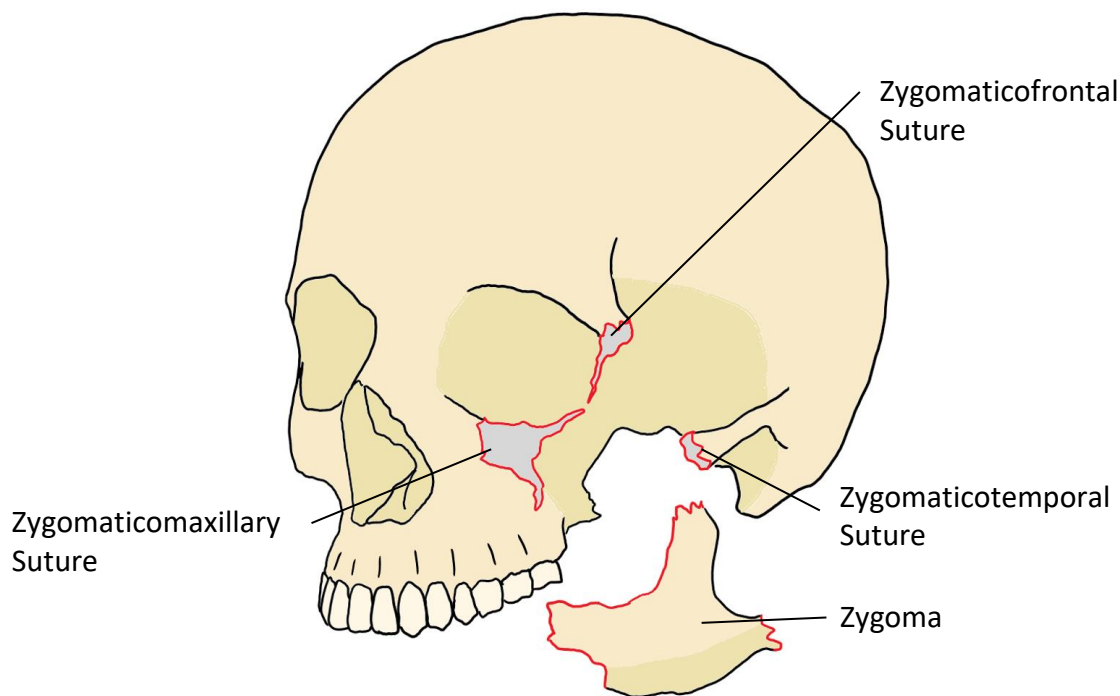
Figure 2. The zygomaticofrontal, zygomaticomaxillary, and zygomaticotemporal sutures are the three connections to the zygoma.

A) Type 1 Fracture   B) Type 2 Fracture
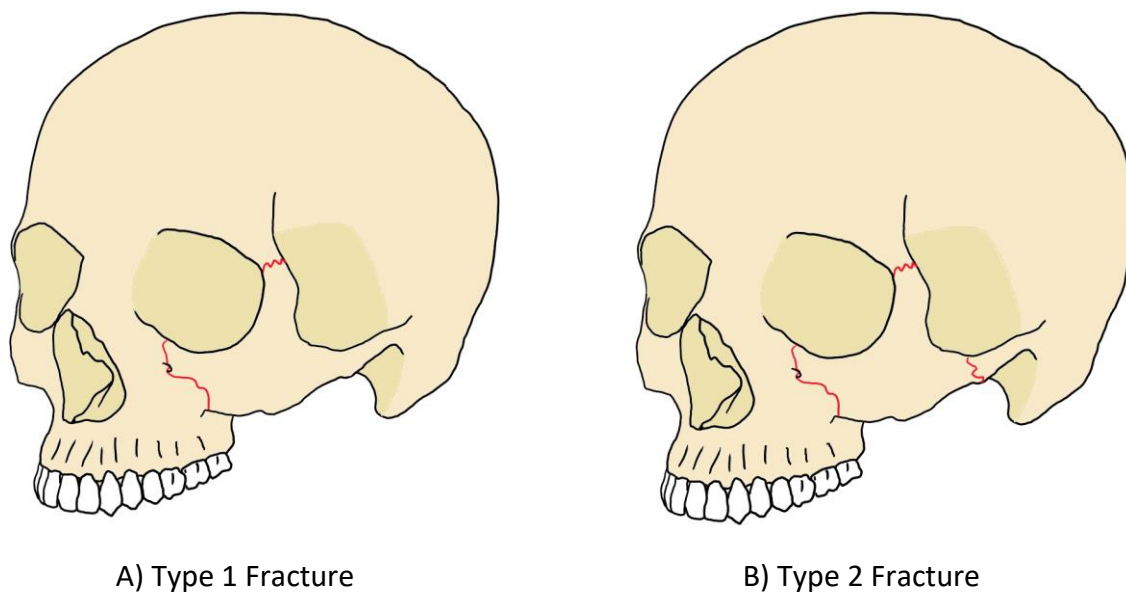
Figure 3. A) Type 1 zygomatic complex fracture and B) type 2 zygomatic complex fracture.

1.1.6 Fracture Fixation

The zygomatic complex provides attachments for suspensory ligaments for the eyeball, muscles, and gives the face width, height, and projection (Jank et al., 2003). Improper reduction and healing of a zygomatic complex fracture can have a detrimental impact on facial aesthetics and ocular function (Miloro, Ghali, Larsen, &Waite, 2011).

A fracture either goes through direct healing or indirect healing (Hak, Toker, Yi, &Toreson, 2010). Direct healing, also known as primary healing, is characterised by a repair process similar to bone remodelling. This mode of healing only take place where there is no relative movement between the bone fragments. Indirect healing, also known as secondary healing, can take place when there is relative movement between the fragments. Indirect healing is characterised by the formation of bony callus where vasculature and bony material regrow. As long as the strain in the fracture gap is less then 2% (up to 10% depending on the bone type), bone healing can still take place (Perren, 2002). Large relative movements between the bone fragments can disrupt normal healing process and may result in non-union fractures.

From earlier description of buttresses in the midface, the zygomatic complex structure experiences complex loadings and plays a crucial role in the load transfer in the craniofacial structure. Depending on the extent of a zygomatic complex fracture, the load acting on the structure may cause excessive relative movements in the fracture and impede healing. Common indicators for when surgery is required are: deformed cheek, pressure on the infraorbital nerve, and restricted range of motion in mouth opening (Chakranarayan, Thapliyal, Sinha, &Suresh, 2009). Surgical management of type 1 and type 2 zygomatic complex fractures generally involves the use of titanium mini bone plates to provide rigid fixation (Figure 4). In a type 2 fracture, a plate is placed across the zygomaticotemporal suture on the zygomatic arch. In both type 1 and 2 fractures, a plate is placed across the zygomaticofrontal suture on the lateral orbital rim, and an "L" shaped plate (L-plate) is placed on the zygomatic buttress. However, the need for a second plate placed along the zygomaticomaxillary suture on the infraorbital rim is controversial (Barry, Ryan, &Stassen, 2007; Eski et al., 2006; Maturo &Lopez, 2008). Proponents for the use of the infraorbital rim plate argued that the plate is essential in providing rotational stability for the zygomatic complex (Holmes &Matthews, 1989; Ramesh Candamourty &, M. F. Baig , M. R. Muthusekar, Manoj Kumar Jain, 2015; Rana et al., 2012; Wood, 1980; Zingg et al., 1991). Opponents of the use of the infraorbital rim plate argued that the L-plate on the zygomatic buttress alone can provide stability along the entire zygomaticomaxillary suture (Chakranarayan et al., 2009; Kovács &Ghahremani, 2001). They also pointed out the following clinical risks involved with the infraorbital rim plate, though these risks for complication are generally low (Kubota et al., 2012). Screws could damage the underlying infraorbital nerve (Taicher, Ardekian, Samet, Shoshani, &Kaffe, 1993). Palpability and visibility of the plate were the most common complications (Islamoglu, Coskunfirat, Tetik, &Ozgentas, 2002). Infection around the plate, exposure of the plate, could require the plate to be removed in a secondary surgery (Llandro &Langford, 2015). A single centre study suggested that around 12% of the type 1 and type 2 zygomatic complex fracture cases employed an infraorbital rim plate (Llandro &Langford, 2015); however, this number may vary from centre to centre. The answer to whether there is a need for the infraorbital rim plate, or if the benefit of the plate outweighs the risks, remains inconclusive.
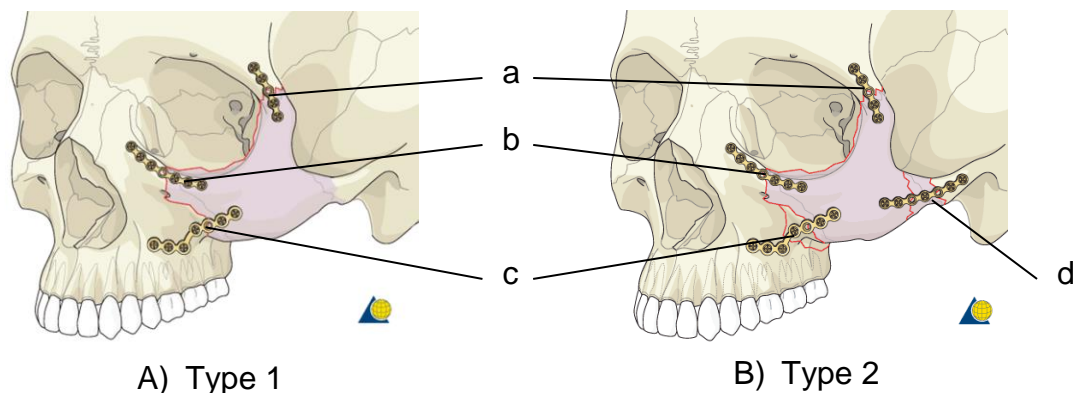
Figure 4. A) Type 1 and B) type 2 fracture repairs. Common plates are a) lateral orbital rim plate, b) infraorbital rim plate, and c) L-plate across the zygomaticomaxillary suture. A d) straight plate is only used in a type 2 fracture. (Reprinted in accordance with AO Foundation Sites General Terms and Conditions)

1.2 Muscles of Mastication

Muscles of mastication are a group of muscles involved in the movement of the mandible. There are more than 20 muscles involved in mastication, the four main muscles are the masseter, temporalis, medial pterygoid, and lateral pterygoid. There is one of each muscle on each side of the face. All except for the lateral pterygoid muscle, elevate the mandible; the lateral pterygoid muscle produces forward movements of the mandible and assists in opening the mandible. The elevator muscles, or jaw-closing muscles, close the mandible and generate bite force. Jaw-opening muscles depress the mandible and open the mouth. The digastric, geniohyoid, and mylohyoid muscles, along with gravitational force acting on the mandible, work together to open the jaw (vanEijden, Korfage, &Brugman, 1997).

1.2.1 Temporalis Muscle

The temporalis muscle is a large, flat, fan-shaped muscle that wraps around the lateral side of the skull (Figure 5). It originates from the temporal fossa of the skull and inserts at the mandibular condyle. The temporalis muscle can be divided into anterior fibres and posterior fibres (Andrade &McLoon, 2013). The anterior fibres lower and close the

mandible, while the posterior fibres contribute to the complex grinding movement by retracting the mandible backwards.
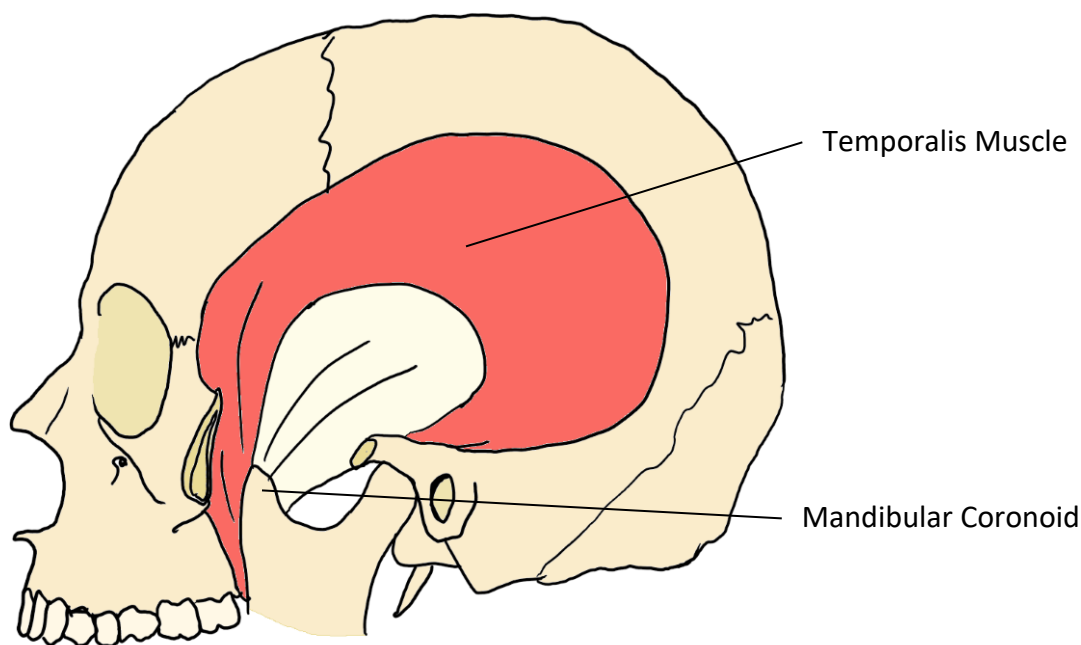
Figure 5. The temporalis muscle. The zygomatic arch was cut away to show the mandibular coronoid.

1.2.2 Masseter Muscle

The masseter muscle is a quadrilateral-shaped muscle that originates from the zygomatic arch and inserts into the ramus of the mandible (Figure 6). The masseter can be divided into the superficial and deep layers. The larger superficial layer originates from the anterior two-thirds of the zygomatic arch and inserts into the lower one-third of the ramus. The deep part of the masseter muscle has its origin spreads through the entire length of the zygomatic arch and inserts into the upper two-thirds of the ramus (vanEijden et al., 1997). Although the primary function of the masseter muscle is to elevate the mandible, it also takes a small role in laterotrusion and protrusion of the mandible.
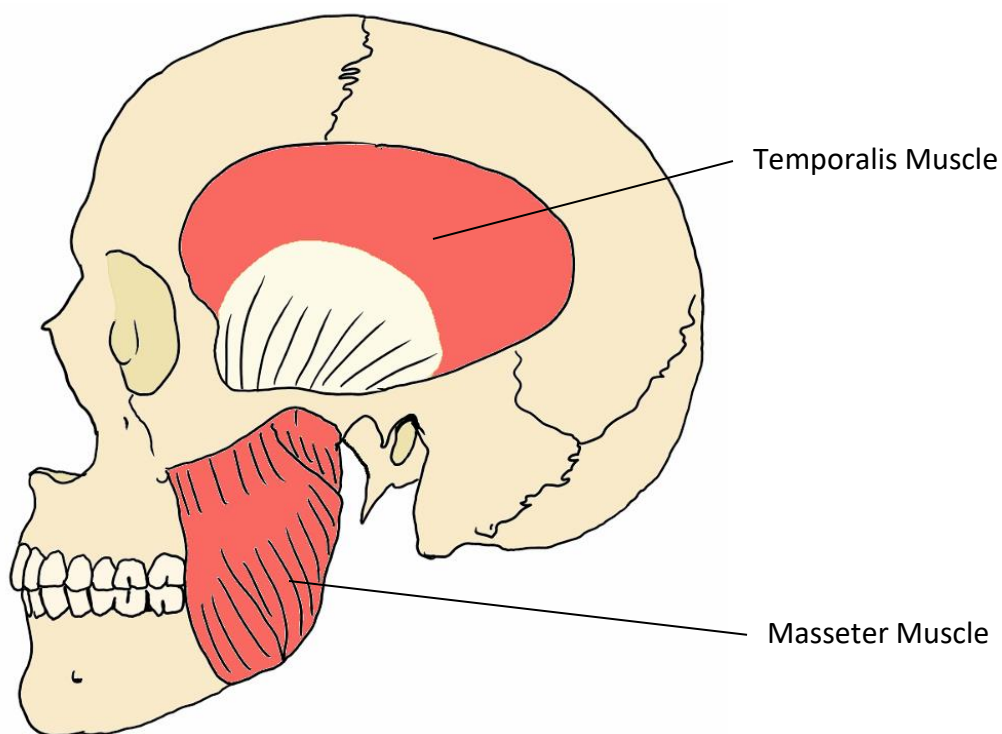
Figure 6. The masseter muscle in relation to the temporalis muscle.

1.2.3 Muscle Force

There are three kinds of muscles in the human body: cardiac, smooth, and skeletal muscle. Muscles involved in the masticatory systems are skeletal muscles. Skeletal muscles can be voluntarily controlled and have long fibres that usually spans the entire length of the muscle. For most muscle fibres, each fibre is innervated by a single nerve ending located in the mid-span of the fibre (Andrade &McLoon, 2013). Neurotransmitters released from the nerve trigger an electric signal that causes muscle fibres to axially contract, resulting in a contractile force.

The line of action of a muscle is traditionally determined by joining the centroids of the origin and insertion's attachment areas; it is based on the assumption that all the fibres in the muscle act in unison to generate a linear force (Meyer, Kahn, Boutemy, &Wilk, 1998). In reality, groups of muscle fibres can have different orientation and contract with different force (vanEijden, Klok, Weijs, &Koolstra, 1988). For example, the fan-shaped

temporalis muscle has fibres directed in the superior-inferior direction in the anterior portion, and fibres directed nearly anterior-posterior in the posterior portion of the muscle. In biomechanical analysis, wide muscles are treated to have separate lines of action for different portions of the muscle. In the case of the temporalis muscle, the anterior and posterior portions have their individual lines of action in biomechanical analysis and mathematical model of the masticatory system (Meyer et al., 1998; Nagae, Bérzin, Alves, &Bérzin, 2011; vanEijden et al., 1988). Studies have shown bite force as a function of mouth opening angle, bite contact location, and to have a large variation in in-vivo bite force between individuals (Meyer et al., 1998; Pruim, deJongh, &tenBosch, 1980). Reported maximum in-vivo bite force ranged from 400 N to 1000 N.

In-vitro muscle force can be estimated using a combination of the muscle's cross-section area and the electrical activity of the muscle tissue during activity, called electromyography. First, there is a linear relationship between a muscle's force output and its cross-sectional area, and studies have reported the same linear relationship in masticatory muscles (Sasaki, Hannam, &Wood, 1989; Weijs &Hillen, 1985). The cross-section of a muscle is commonly obtained through computed tomography (CT) or magnetic resonance imaging (MRI). Second, electrical signals in the muscle can be measured with electromyography (EMG), in which either surface-placed or implanted electrodes measure electric potential in the muscle. The intensity of the electrical signal was found to be related to the force developed by the muscle (Woods &Bigland-Ritchie, 1983). Using the information from a muscle's cross-sectional area, as well as EMG data of the muscle under contraction, the muscle contractile force of the muscle can be estimated. Biomechanical statics analysis also provides information when determining muscle force. Forces acting on the mandible are balanced to three-dimensional static equilibrium. However, due to the number of muscles involved in mastication, the force system is often simplified to avoid an indeterminate system (Meyer et al., 1998).

Physiological muscle loads are internal (or intrinsic) loads. When a muscle contracts, the force is generated between the origin and the insertion, generating two equal and opposite force vectors between the cranium and mandible. An external (or extrinsic) load, on the other hand, is defined as loads that originate from outside of the skull. For example,

compressing a skull manually by applying force between the cranium and the mandible is considered an external load on the skull. Although both of these loading methods can produce the same bite force, load distribution in the skull may differ when under external versus internal loads.

1.3 State-of-the-Art Review

1.3.1 Introduction

Physical simulators have been developed for the human skull. There are two general classifications of these simulators. The first group of simulators are dynamic simulators that aim to reproduce kinematics of the mandible. Studies using these simulators to investigate chewing motion (Daumas, Xu, &Bronlund, 2005), implant design (Celebi et al., 2011), and rehabilitation (Takanobu, Takanishi, &Kato, 1993). The second group of simulators are static simulators that aim to reproduce physiological muscle loads in the skull. Studies that utilise these simulators often investigate bone strain in the skull under simulated muscle loads. These static stimulators will be the focus of the state-of-the-art review to follow.

1.3.2 Simulators Using External Load

External loads in these simulators are often applied using a material testing machine. A typical material testing machine applies axial force or displacement with high accuracy. Alberts et al. (2003) attempted to investigate rigid plate fixation in the maxilla. In the study, the mandible was detached from the cranium. The cranium was affixed to the material testing machine using transcranial screws and force was applied through the palate. In another study (Kasrai, Hearn, Gur, &Forrest, 1999), failure pattern of fraction fixation was investigated by applying a load to the zygomatic complex in the anterior-posterior direction with a material testing machine. In an animal study looking at canine dental implants (Kan, Judge, &Palamara, 2014), canine skulls were fixed on the top of the cranium and force is applied to the inferior edge of the mandible to generate bite force. Similarly, Sutradhar et al. (2014) attempted to reproduce masticatory load in synthetic skulls by fixing the top of the cranium and compressing the maxilla with occlusal force.

1.3.3 Simulator Using Internal and Quasi-Internal Loads

There are significant challenges in generating intrinsic in-vitro muscle loads, largely due to the relatively small muscles and short muscle displacements of the masticatory system. Early attempts of applying quasi-internal loads involved applying loads to the cranium through canvas strips glued to muscle attachment sites (Endo, 1965, 1970; Endo &Suzuki, 1966). In these studies, the mandible of a cadaver head was detached from the cranium, the cranium is then fixed at the TMJ and the molar teeth. Muscle attachment areas of the temporalis and the masseter were denuded, canvas strips of equivalent size were then glued to the attachment areas. Static force along the muscle lines of action were then applied with known weights through a pulley system.

A recent iteration of this method utilised a material testing machine in lieu of static weights (Maloul, Regev, Whyne, Beek, &Fialkov, 2012). In this study, the material testing machine pulled on the temporalis muscle directly through a transected mandibular condyle and pulled on the masseter muscle through a metal plate sutured to the masseter tendon. This simulator could not apply load to the temporalis and masseter simultaneously and could only apply load to one side of the specimen.

The above simulators using quasi-internal loads transmitted simulated muscle force through physiologically accurate areas on the cranium; however, the reaction forces on the cranium came from the fixture, not the mandible. The effect of this deviation has on strain pattern in the craniofacial structure is not known.

A study attempted to use springs to generate internal load between the cranium and mandible (Ji, Wang, Song, Chen, &Wang, 2012). Stainless steel springs were attached along muscle lines of action on synthetic skull models using screws. The simulated muscle forces were controlled by elongations of the springs. Controlling the length of the springs to produce the desired force can be difficult. Furthermore, this method of generating masticatory forces is passively controlled, it therefore greatly limits flexibility in experimental design. Similar methodology had been used to determine the efficacy of fracture plating techniques in the mid-face (Wang, Chen, Fan, Tang, &Tian, 2007).

1.3.4 Strain Measurement

Strain is the deformation of a material under load. Strain gauge is the most common instrument for strain measurements. A strain gauge has a thin wire attached to a thin, flat polymer substrate. The gauge is firmly secured to the material at the location of interest. When the material experiences load, the strain gauge deforms together with the material (Cordey &Gautier, 1999a). The deformation in the strain gauge causes a change in the wire's electrical resistance and hence the electrical potential across the gauge. Uniaxial strain gauge is the most basic type of strain gauge. As suggested by its name, a uniaxial strain gauge only measure strain in one direction. Advantages of measuring strain using a strain gauge include its sensitivity and accuracy. However, a strain gauge can only measure localised strain on a relatively flat surface. More complex strain gauges, such as a Rosette strain gauge, has multiple matrices of thin wire laying in different directions within the footprint of the gauge. The direction of the strain can then be determined using these measurements. These multi-directional strain gauge are larger to a comparable uniaxial strain gauge.

There are other strain measurement methods that can capture the strain field over a wider area. Strain responsive lacquer was used for studying strain field in the craniofacial structure (DEForest &Ellis, 1940; Endo &Suzuki, 1966). The lacquer, applied to bone, creates fields of crack lines under a threshold strain. Although these strain responsive lacquers can capture a strain field, they are of one-time use and does not allow changing loading regime on the same specimen. Recent development in image processing inspired strain measurement techniques such as digital image correlation (DIC) and digital volume correlation (DVC). DIC for in-vitro bone strain measurement tracks paint speckles on bone using multiple high resolution, high-speed cameras. The displacements of paint speckles are then used for reconstructing the strain field of the specimen (Rossman et al., 2017; Soons, Lava, Debruyne, &Dirckx, 2012; Sztefek et al., 2010). Similarly, DVC reconstruct strain fields from micro-CT images of the specimen before and during load (Dall'Ara et al., 2017; Palanca et al., 2017; Tozzi, Danesi, Palanca, &Cristofolini, 2016; VonWilmowsky et al., 2015). Although both DIC and DVC can capture strain field over a wide area, DIC requires significant investment in optical investment and requires line-

of-sight to the area of interest; DVC, on the other hand, requires long data acquisition time and loading equipment used must be CT-compatible.

1.4   Rationale, Objectives, and Hypothesis

1.4.1 Rationale

Present simulators rely on external or incomplete-internal loads for in-vitro study of craniofacial bone strain distributions. There is a need for an in-vitro simulator that can reproduce clinically relevant internal muscle loads in the masticatory system. The simulator can be used for validating computer simulations and answering clinical questions such as those related to implant design and fracture fixation.

1.4.2 Objectives and Hypotheses

Objectives:

1. Develop a specimen-specific in-vitro simulator that can apply internal muscle force in the masticatory system;

2. Compare strain patterns in the craniofacial structure under internal and external loads;

3. Implement simulator in a clinically relevant investigation: Comparison of strain patterns with and without infraorbital rim plate in type 1 and type 2 zygomatic complex fractures.

Hypotheses:

1. Strain patterns in the craniofacial structure are different (with statistical significance) under internal and equivalent external loads;

2. Strain patterns in the craniofacial structure are different with and without infraorbital rim plate in type 1 zygomatic complex fracture;

3. Strain patterns in the craniofacial structure are different with and without infraorbital rim plate in type 2 zygomatic complex fracture.

1.5   Thesis Overview

Chapter 2 describes the technical development of the in-vitro simulator. This chapter also outlines the experimental protocol which involves the sequence for zygomatic complex fracture simulation and repair. Chapter 3 presents the results obtained from the zygomatic fracture and repair experiments. Finally, the significance of the results is discussed in Chapter 4.

Chapter 2

2 Methodology

The Temporomandibular (TM) Force Simulator (Figure 7) utilises subject-specific 3D-printed muscle mounts to allow the installation of muscle in-line pistons to reproduce intrinsic muscle loads. These subject-specific 3D-printed mounts (Figure 7; b and c) are affixed to the origin of the temporalis and the insertion of the masseter with a combination of adhesive and screws. The forces from the temporalis and masseter muscle groups can be applied by the simulator as a proportion to their physiological capabilities. There are six pneumatic pistons in total, two pistons (anterior and posterior) for each of the two temporalis piston mounts, and one piston for each of the two masseter piston mounts. This section will cover the development of the TM Force Simulator, including reverse engineering involved in the production of specimen-specific hardware, specimen preparation and instrumentation, and the control system of the simulator. The experimental protocol will also be discussed in this section.
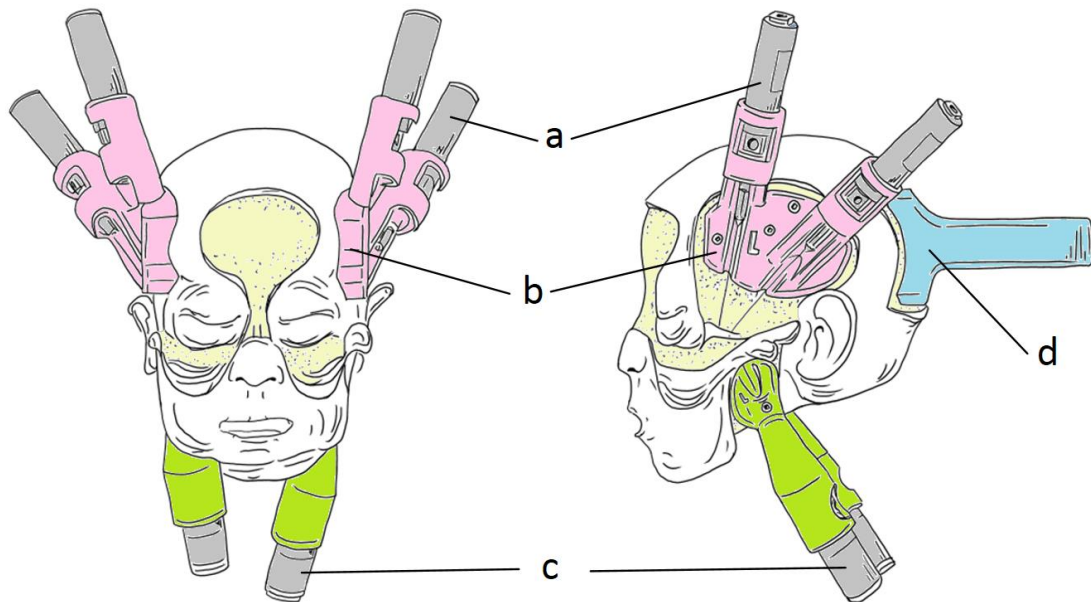
Figure 7. Temporomandibular (TM) Force Simulator
a) Pneumatic pistons; b) Temporalis piston mount; c) Masseter piston mount; and
d) mounting block for specimen fixation.

2.1 Reverse Engineering of Muscle Attachment Sites

A piston mount was required to fit over the entire surface of the native muscle attachment area. This would allow stresses from piston load to be dispersed similar to muscle load, producing physiologically relevant bone strains in the areas of interest. The piston mounts needed to conform to the organic topography of the muscle attachment sites, as well as to hold pneumatic pistons in the muscles' lines of action. It would have been impractical to produce piston mounts using traditional manufacturing technique. Rapid prototyping through additive manufacturing (3D printing) offered a cost- and time-effective mean to produce piston mounts that would satisfy the engineering requirements.

2.1.1 Computed Tomography and Image Processing

Each fresh-frozen human cadaveric head specimen was scanned, while frozen, with computed tomography (CT) (GE Discovery CT750 HD; Chicago, IL, USA) with clinical setting (120 KvP; 250 mm field of view; 0.625 mm slice increment; 0.625 mm slice thickness; resolution of 512×512; and 0.488 mm pixel size). The specimen was placed in the CT's scanner's head holder in the supine position. The raw CT image had the cranium and mandible segmented out after thresholding operation in a 3D medical imaging processing software (Mimics; Materialise NV; Leuven Belgium). The segmented skull was then processed in a 3D modelling software (3-Matic; Materialise NV; Leuven Belgium) to remove geometrical and topological defects. The computer model of the skull was finally imported into a computer-aided design (CAD) software (Solidworks 2015; Dassault Systèmes; Vélizy-Villacoublay, France) to carry out the remaining reverse engineering operations.

2.1.2 Anatomical Landmark Extraction

Since the specimens were CT scanned while frozen and most specimens had their mandibles in the maximum opening position, the mandibles were virtually realigned to the intercuspation position. Care was needed when aligning the mandible as many of the specimens were partially or completely edentulous. Tendon attachment footprints where

piston mounts would be place were outlined on the CAD model based on anatomical landmarks (Logan, Reynolds, Hutchings, &McMinn, 2010). This included the origin of the temporalis on the temporal fossa of the cranium and the insertion of the masseter on the lateral surface of the mandible's ramus. The origin of the temporalis was further divided into anterior and posterior portions (VanEijden, Koolstra, &Brugman, 1996). The line of action was then drawn between the centroid of each identified attachment outline and the insertion (Figure 8). The points on the attachment area were given offsets of 6 mm in order to compensate for muscle thickness and provide clearance for hardware. The insertion of the temporalis was the mandibular coronoid and the insertion of the masseter was the mid-point of the zygomatic arch's inferior edge.
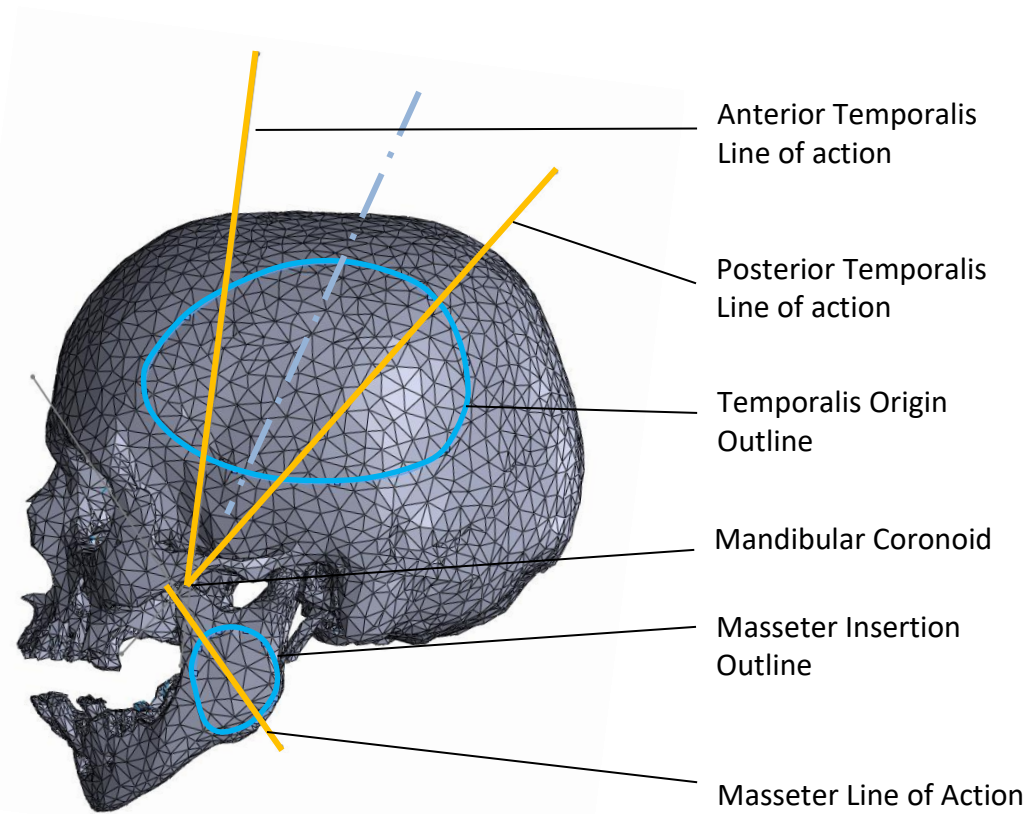
Figure 8. CAD model of the specimen. The midline of the temporalis separates the anterior and posterior halves of the temporalis. The lines of action (LOA) of the muscles and the tendon footprints for the reverse-engineered piston mounts are

labelled. The two LOA of the temporalis points towards the mandibular coronoid. The LOA of the masseter points towards the anterior third of the zygomatic arch

2.1.3 Piston Mount Design

Parametric, pre-designed piston mounts were adjusted so that a piston's rod would align with a muscle's line of action draft out in the skull CAD model. The temporalis mount had two cylinders on the mount for the anterior and posterior temporalis piston. The piston mounts had cut-outs so the piston rods could be accessed when pistons were installed. The bone-mount interface was virtually extended to the bone to produce a contact area matching the tendon attachment footprint, and a surface congruent with the osseous topography of the attachment area. This congruency would later provide a conforming surface which would be adhered to bone using adhesive. Similarly, a specimen fixation mount was virtually fitted to the back of the skull, which would fix the head in place during experimentation.

The pneumatic piston selected (Airpel Anti-Stiction Air Cylinders; AirpotCorp; Norwalk, CT, USA) used a combination of a graphite piston and a glass-lined bore to reduce stiction in the piston. The anti-stiction property provided by this model of pneumatic piston reduced friction lost in the system. The pistons had mounting threads that allowed them to be securely screwed to the piston mounts.

2.1.4 Additive Manufacturing and Post-Processing

The CAD models of the piston mounts and specimen mounting block were exported as STL, which were then imported to a 3D print preparation software (MakerBot Desktop; MakerBot; Brooklyn, NY, USA). The parts were 3D printed with polylactic acid (PLA) filament using a fused filament fabrication machine (Replicator 5th Generation; MakerBot; Brooklyn, NY, USA). After a part completed printing, the support material was removed. With piston mounts, holes were manually tapped to match the piston mounting threads.

2.2   Specimen Preparation

Since the piston mounts occupied the same attachment area as the muscle they were to replace, the muscles would need to be dissected out before the mounts could be installed. In contrast, the tendon and muscle attachment on the other end of the piston mount was preserved so the pneumatic piston could pull on the tendon attachment. Strain gauges were installed at predetermined locations and were standardised across all specimens.

2.2.1 Fresh Frozen Human Cadaveric Head

A total of 6 fresh-frozen human cadaveric head specimens were used (Table 1). The first specimen (76 F) was used as a proof of concept and did not go through the fracture protocol, only the remaining 5 specimens (average age: 78.6±14.5 (SD); 3 males, 2 females) went through the entire experimental protocol. All the specimens were previously used for dental surgery training.

Table 1. Specimen demographics

Specimen	Specimen No.	Age	Sex
0	15-12012	76	F
1	16-01039	96	M
2	16-01058	55	F
3	16-01033	81	F
4	16-01019	71	M
5	17-01032	90	M

2.2.2 Specimen Dissection

A surgical resident performed all the dissections on the specimens. The specimens were thawed in a refrigerator at 3ºC for 12 hours until superficial soft tissues were soft enough to be excised. The neck was sawed off at the C1 vertebra to provide clearance for piston mounts. The origin of the temporalis and the insertion of the masseter were excised, and their attachment areas were dissected clean of all soft tissue. A periosteal elevator was used to scrap clean remnant of fibrous tendon tissue. This soft tissue removal procedure was repeated for the area where the mounting block would attach at the back of the skull, and the areas where strain gauges would be placed. Soft tissue superficial to the

masseter's origin were dissected away to expose the attachment on the inferior edge of the zygomatic arch. A size 2 polyester braided suture (Ethibond; Johnson & Johnson Medical N.V.; Belgium) was sutured to the masseter's origin tendon to create an anchorage point for the force application. In the pilot specimen, a similar procedure was applied to the mandibular coronoid at the insertion of the temporalis. However, it was found that the insertion tendon was failing under load. For subsequent specimens, the denuded mandibular coronoid had a 1.58 mm hole drilled through in the medial-lateral direction. The hole was drilled in the centre of the mandibular coronoid with 4 mm distance from the anterior and posterior margin. The 4 mm margin provide enough bone stock to prevent fracture in the coronoid under piston load, yet preserve the anatomical relevance of the attachment point by keeping it within the tendon footprint of the temporalis insertion. A suture was tied through the hole drilled to act as the anchorage point for the temporalis pistons. The point load application on the mandibular coronoid was far removed from the midface so it is not expected to affect the load distribution.

Areas in the mid-face were also denuded down to bone for strain gauge installation. All other soft tissues were left intact.

2.2.3 Muscle Actuator Installation

The denuded tendon attachment areas were roughened with a stainless-steel wire brush and degreased with isopropyl alcohol and a bleach-based cleaner. Then the mounts were affixed using construction adhesive (PL Premium; LePage; Henkel Canada Corporation; Mississauga, ON, Canada), which was shown in pilot testing of porcine specimens to be suitable and sufficiently impervious to moisture. Two to three wood screws (US size 3.5) per mount were used to secure the mounts to bone while the adhesive cured. The specimen was returned to the freezer for 48 hours to ensure even curing of the adhesive.

On the day of the experiment, the pneumatic pistons were screwed onto the piston mounts. Braided Dacron lines tied between the piston rod and the corresponding suture anchor created during specimen dissection. The masseter piston made use of the suture anchor on the masseter origin tendon. The temporalis pistons made use of suture anchor

at the hole drilled on the mandibular coronoid. The specimen is clamped onto a post at the specimen mounting block.

2.2.4 Strain Gauge Instrumentation and Load Cell Placement

Twelve 3-lead pre-wired uniaxial strain gauges (CEA-13-062UW-350; Micro-measurements; Wendell, NC, USA) were used to measure craniofacial bone strains during simulated occlusal loading. The gauges were strategically placed along buttresses of the midface to assess strains at these locations of clinical interest (Figure 9). Installation followed established guidelines from literature (Cordey &Gautier, 1999b). Each side of the face received six strain gauges, which were mirrored across the mid-sagittal plane. Strain Gauge ZB measured strain parallel and superior to the lateral zygomatic buttress. Strain Gauge IO, measured lateral strain inferior to the infraorbital rim. Strain Gauge FH measured vertical strain in the forehead. Strain gauge SO measured lateral strain in the superior orbital rim. Strain Gauge ZA measured lateral strain across the zygomatic arch. At last, Strain Gauge LO measures vertical strain in the lateral orbital rim below the zygomaticofrontal suture.

On the day of the experiment, a six-DOF load cell (Mini45; ATI Industrial Automation; Apex, NC, USA) was placed in the specimen's oral cavity to measure bite force produced during experimentation. The load cell was attached to a mouldable sports mouth guard (strapped mouth guard; EZ GARD Industries, Inc; Minnetonka, MN, USA) to reduce movement during the experiment.
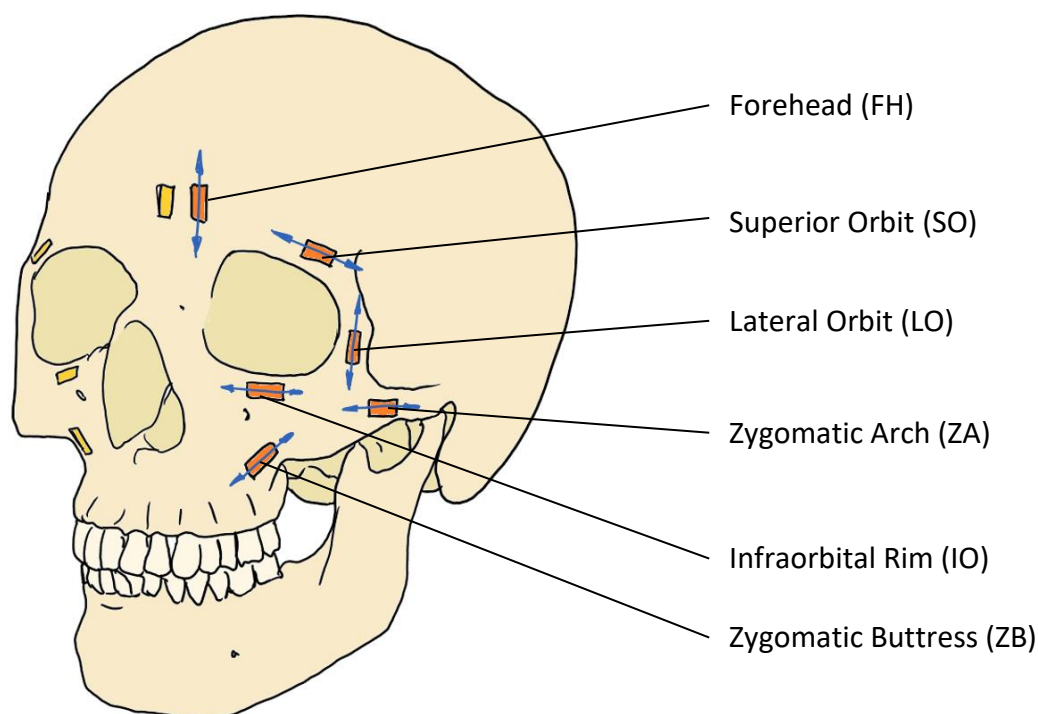
Figure 9. Locations of uniaxial strain gauges. Blue arrows show directions of strain measured.

2.3   Data Acquisition and Force Control System

The data acquisition and force control system were operated using a custom program (LabVIEW; National Instruments; Austin, TX, USA). To generate the load to mimic muscle forces, the system provided the pneumatic pistons with air pressure required based on software calculation. When the simulator was in action, the strain and bite force measurements were collected and stored by the system for analysis. The following section describes hardware and software related to the system.

2.3.1 Muscle Load Control

The air supply to the pneumatic pistons was controlled with an open-loop system. The desired actuator force output was determined based on in-vivo muscle force estimates under full bite load (Meyer et al., 1998). Each of the six pistons was individually controlled by a proportional pressure controller (PPC) (PPC5C; MAC Valves; Wixom, MI, USA). An air compressor with an air reservoir (5510SE; California Air Tools; San

Diego, CA, USA) supplied air to the PPC's. A PPC could read an analogue voltage signal between 0 to 10 V and linearly vary the output air pressure from 0 to 100 psi. For example, a 5 V signal would correspond to an output pressure to 50 psi and a 6.2 V signal would correspond to an output pressure of 62 psi.

In the force control module of the LabVIEW program, the force generated by the system was represented as a percentage of maximum physiological output. Base on the percentage, the LabVIEW program calculates the pressure required to produce the force for each individual piston and the corresponding voltage outputs to the PPC's. The voltage is generated by a voltage output module (NI 9264; National Instruments; Austin, TX, USA). The LabVIEW program could independently control each of the 12 pistons, which would allow the experimenter to apply load to individual muscle groups and asymmetric masticatory loads.

2.3.2 Data Acquisition

Two types of data were recorded by the data acquisition system: strain and bite force. Each three-lead pre-wired strain gauge was connected to a quarter-bridge completion adaptor (NI 9945; National Instruments; Austin, TX, USA). These bridge completion adaptors were connected to strain input modules (NI 9237; National Instruments; Austin, TX, USA). Each module had four input ports; thus, three modules were used in combination to gather strains from all 12 gauges. The three strain input modules and the voltage output module were connected to via a USB chassis (NI cDAQ™ 9174; National Instruments; Austin, TX, USA).

The 6 degrees-of-freedom (DOF) load cell was connected to the computer via a separate USB I/O device (NI USB-6210; National Instruments; Austin, TX, USA). An electrical wire was connected between the metallic surface of the load cell and the voltage output module to create a grounding path between the two USB devices. This ground wire reduced electromagnetic interference the load-cell had on the strain gauges. The LabVIEW program computed the net force on the load cell based on the three raw force components.

In the LabVIEW program, the strain measurements and the bite force were displayed. There was a software module that can zero the bite force measurement and another for the strain measurements. On command, the LabVIEW program could capture 50 measurements from the load cell and each of the strain gauges at 500 Hz. These measurements were automatically written to a data file and stored in the computer.

2.4   Experimental Protocol

This section will describe loading regimes for both internal and external loads. The equipment and sequence for simulating fractures and repairs will be reported.

2.4.1 Internal Load Application

Physiologically proportionate internal loads were applied through pneumatic pistons to simulate masticatory forces. The loads were scaled down to 5%, 10%, and 15% of maximum muscle force output reported in the literature (Table 2).

Table 2. Muscle loads at 5%, 10%, and 15% of maximum physiological load (Meyer et al., 1998)**.**

Muscle	Full Physiological Load (N)	5% Load (N)	10% Load (N)	15% Load (N)
Temporalis, Anterior	412	20.6	41.2	61.8
Temporalis, Posterior	169	8.5	16.9	25.4
Masseter	475	23.8	47.5	71.3

In the pilot specimen, it was found that load exceeding 15% of the physiological maximum would cause the suture-tendon interface to fail. The loads applied in subsequent specimens were therefore capped at 15% of the physiological maximum. When loads were increased, they were systematically ramped up to prevent sudden shock to the system, which could potentially damage soft tissues in the specimen.

Strain and bite force measurements were collected at each of the three load levels. The strain gauges and load cell were zeroed before loads were applied to reduce influence

from random factors. The loads were repeated five times to assess repeatability of the simulator.

2.4.2 External Load Application

External loads to the specimen were applied manually. The bite force measurements under internal loads were referenced. The specimen was then compressed between the top of the cranium and the bottom of the mandible such that the load cell measured the same bite force as generated by internal load. Manual compressions were carried out at 5%, 10%, and 15% internal load equivalents. Strain and bite force measurements were recorded once the desired bite force was reached. The external loads were repeated five times to assess repeatability.

2.4.3 Fracture and Repair Protocol

The fracture and repair protocol was conducted in four phases. The plating sequence was designed so that plates do not need to be reinstalled after removal (Figure 10). This eliminated potential issues associated with mechanical loosening of plates related to reinstallation of screws. The side of the face on which fracture was simulated was selected so that existing defects from previous dental procedures were avoided (Table 3).

Table 3. The side of the face with simulated fractures by specimen.

Specimen	Side of Fracture
0	NIL
1	Left
2	Right
3	Left
4	Right
5	Left

Osteotomies were performed to simulate traumatic zygomatic complex fractures using a rotary tool (4200 high-performance rotary tool; Dremel; Racine, WI, USA) with an abrasive cutting wheel. A bone elevator was inserted into the cut afterwards to ensure complete separation along the fracture line. Repairs were performed using 1.5 and 2.0 mm titanium plates (Craniofacial Modular Fixation System; Synthesis CMF; Mississauga, ON, Canada). All procedures were performed by an ENT surgical resident

under the supervision of a certified facial plastic surgeon. Care was taken to prevent damage to strain gauges when performing these procedures.
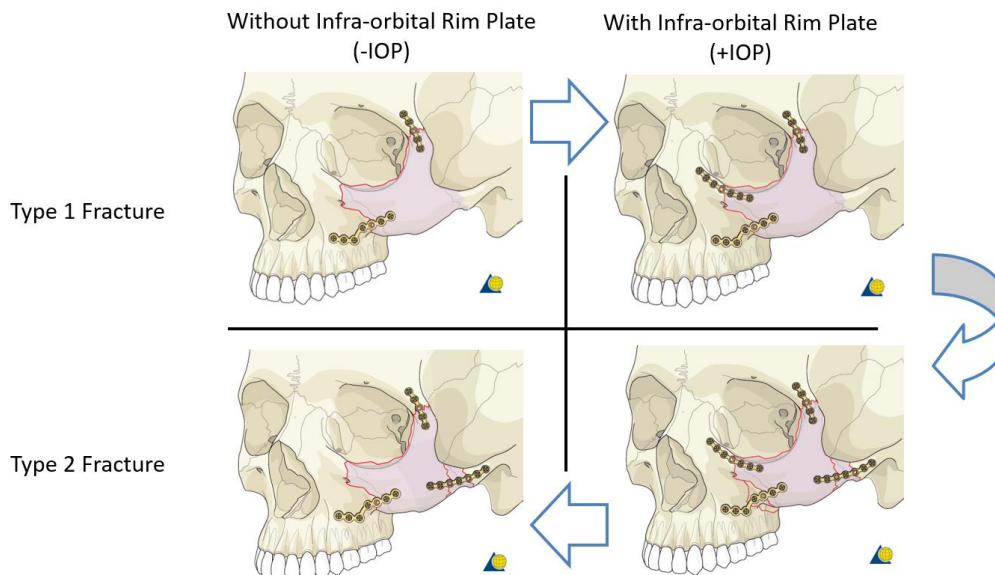
Figure 10. Fracture and repair protocol. Sequence indicated by blue arrows. (Reprinted in accordance with AO Foundation Sites General Terms and Conditions)

2.4.3.1   Phase 0: Baseline Measurements without Fracture

Internal and external loads were applied while the specimen was intact. The purpose of this phase was to collect baseline measurements.

2.4.3.2   Phase 1: Type 1 Fracture without Infraorbital Rim Plate

Recall that in a type 1 zygomatic complex fracture, the zygomaticofrontal and zygomaticomaxillary sutures are fractured. In Phase 1, osteotomies were performed at these two locations (Figure 11). The zygomaticofrontal suture was then repaired with a 2.0 mm orbital rim plate. Similarly, the zygomaticomaxillary suture was repaired with a 2.0 mm L-plate on the zygomatic buttress (Figure 12). There were right-handed and left-handed L-plates; the handiness of the L-plate used was determined by the side of the face the fracture was simulated. Masticatory loads were applied after the repair and measurements were collected.
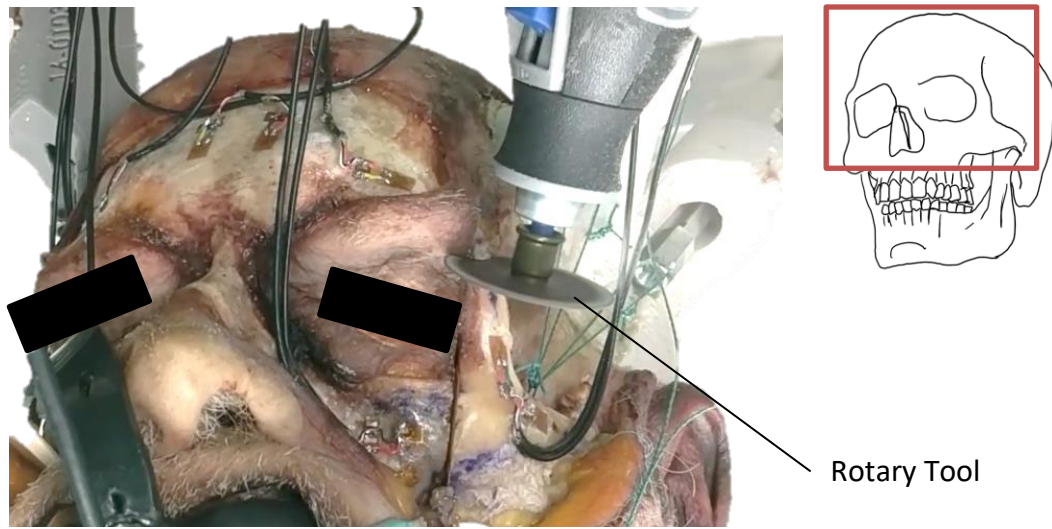
Figure 11. Osteotomy being performed at the zygomaticofrontal suture using a rotary tool.
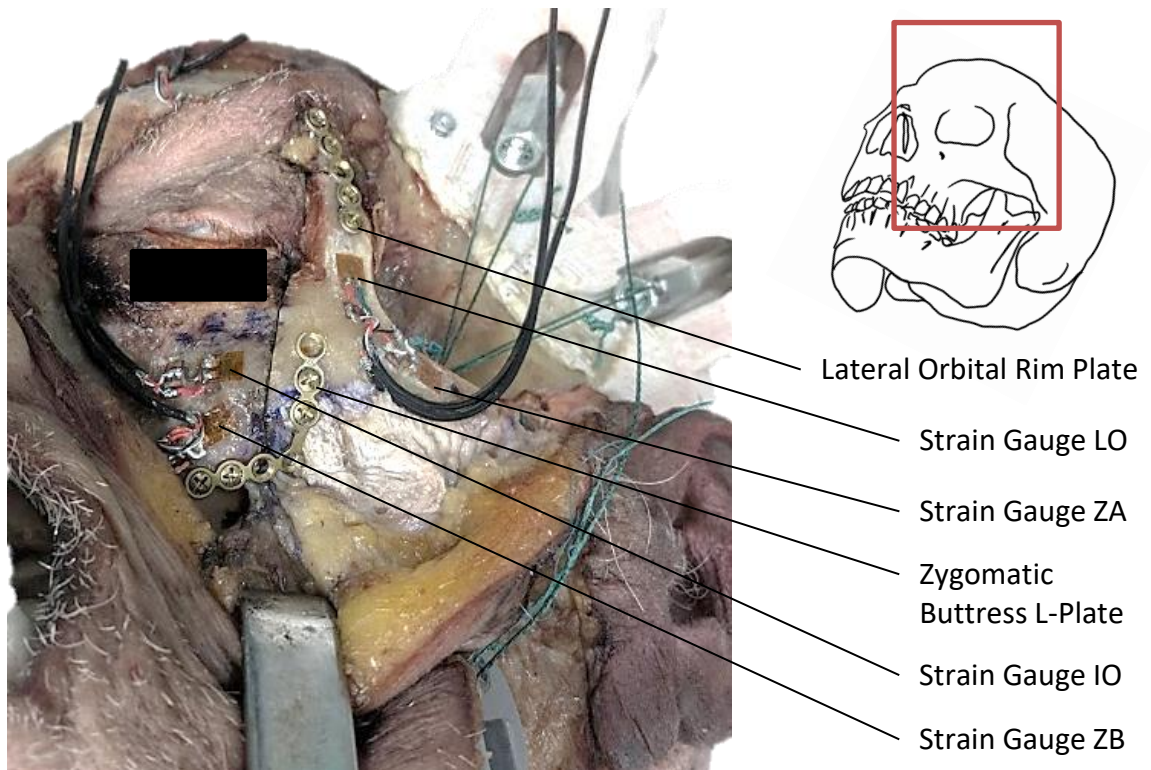
Figure 12.Repair state of a specimen at Phase 1.

2.4.3.3   Phase 2: Type 1 Fracture with Infraorbital Rim Plate

In Phase 2, a 1.5 mm orbital rim plate was added to the zygomaticomaxillary suture at the infraorbital rim. The infraorbital rim plate, in addition to the two plates installed in Phase 1, constituted a 3-point fixation to the zygomatic complex fracture (Figure 13). Masticatory loads were applied after the repair and measurements were collected.
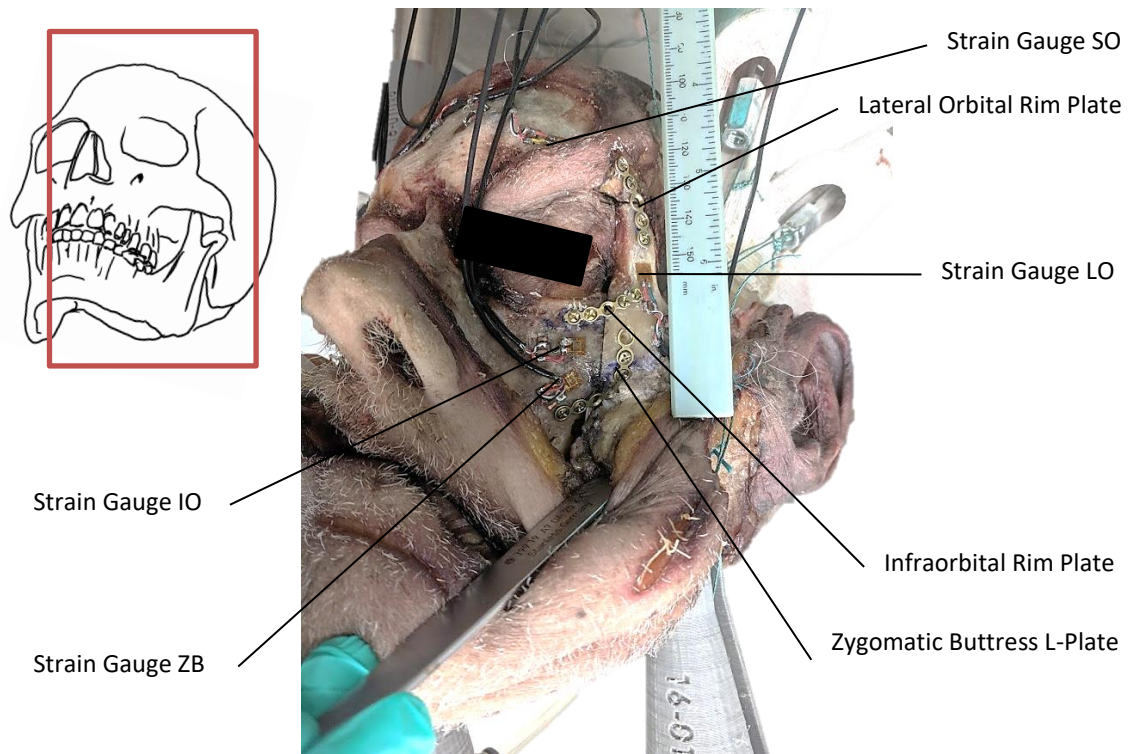
Figure 13. Repair state of a specimen at Phase 2.

2.4.3.4   Phase 3: Type 2 Fracture with Infraorbital Rim Plate

In Phase 3, osteotomy was performed on the zygomatic arch at the zygomaticotemporal suture. The fracture was repaired by a 2.0 mm straight plate. The two plates from Phase 1, the infraorbital rim plate form Phase 2, and the latest plate in the current phase constitute a 4-point fixation (Figure 14). Masticatory loads were applied after the repair and measurements were collected.

Strain Gauge SO

Lateral Orbital Rim Plate

Strain Gauge LO

Zygomatic Arch Plate

Zygomaticotemporal Suture

Strain Gauge ZA
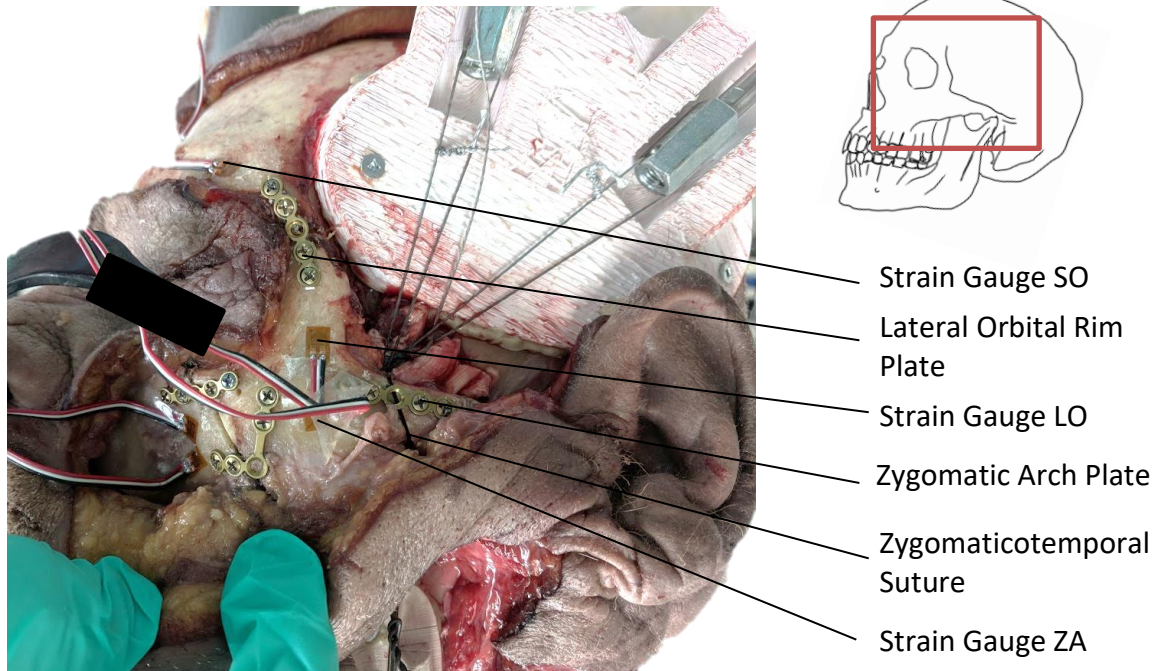
Figure 14. In Phase 3, osteotomy was performed on the zygomatic arch at the zygomaticotemporal suture. The osteotomy was then plated.

2.4.3.5   Phase 4: Type 2 Fracture without Infraorbital Rim Plate

In Phase 4, the infraorbital rim plate was removed. The two plates from Phase 1 and the plate on the zygomatic arch formed a 3-point fixation (Figure 15). Masticatory loads were applied after the removal of the infraorbital rim plate and measurements were collected.

Infraorbital Rim Plate Removed
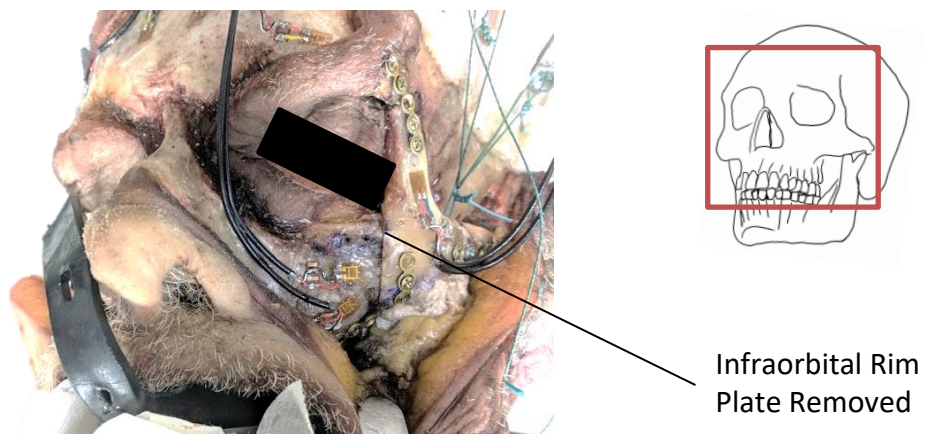
Figure 15. The infraorbital rim plate was removed for Phase 4.

2.5   Statistical Analysis

This section will describe major statistical analysis of experimental results. The setup, rational, and statistical software used will be reported.

2.5.1 Regression Analysis

Regression analysis in baseline analysis was performed with Prism (GraphPad Software; La Jolla, CA, USA). Strain measurements from all five trails at each homologous gauge location (same gauge location on both sides of the face) were plotted against load level of 5%, 10%, and 15%. The coefficient of determination (r^2) will be calculated to assess the linearity of strain measurements with load increase at each location. Similarly, the slope at each location will be calculated to assess the relative increase in strain measurements with respect to load increase.

2.5.2 Analysis of Variance

Repeated measures analysis of variance (RM-ANOVA) was performed to analysis difference between different treatments. The software used for RM-ANOVA was IBM SPSS Statistics (IBM; Armonk, NY, USA).

Only measurements from 15% load were investigated, as the absolute difference in strain was expected to be highest in the highest load level. All five trails at each load sequence were considered in the analysis.

The analysis was set up with the following within-subject factors: load method, fracture phase, and trail number. The load method factor has internal and external load as the two levels. The fracture phase factor has five levels representing Phase 0, 1, 2, 3, and 4 of the fracture protocol. The trail number factor has five levels, one for each of the five repeated trials for each load sequence. The identical setup was used for analyzing bite force. Overall alpha of 0.05 ($p < .05$) was used to determine statistical significance. The standard error of mean (SEM) was calculated to describe the uncertainty when representing the population mean with the sample mean.

2.5.3 Pearson Correlation

Pearson correlation coefficient was used for assessing agreement between strain pattern under internal and external loads, as well as agreement between different fracture repairs and baseline intact state. Statistical software Prism was used for calculating the coefficients. Only strain measurements from the last of the five trails were used. Each of the twelve strain gauges in all five specimens was used as a data point, totalling in 60 data points for each correlation.

Chapter 3

3 Results

The results section will first present measurements from intact specimens under internal and external loads, followed by measurements from the fracture protocol. In all results, the side of the face will be identified by the intact side or fracture side. Estimated means of the five specimens across all five repetitions are presented. Error bars in graphs show standard error of mean (SEM) unless otherwise specified. Similarly, mean ± SEM are presented by default.

3.1 Baseline Measurements

3.1.1 Bone Strains under Internal Loads

Strain measurements under internal load at 5%, 10%, and 15% of physiological maximum were obtained (Figure 16). Homologous strain gauges on both sides of the face were grouped together. Tensile strains (positive strains) were observed around the orbit at locations IO, SO, and LO. Compressive strains (negative strains) were observed at locations ZB and ZA. Strains on the forehead at location FH were negligible in comparison. Strain measurements at all locations increased linearly correlated ($r^2 > .99$) with increase in load. Regression slopes of strain measurements under internal loads varied by location (Table 4).

Strain measurements in individual specimens showed asymmetry across the two sides of the face as illustrated by Specimen 5 (Figure 17). Location IO measured compression on the left side but tension on the right side. In contrast, location SO measured tension on the left side but compression on the right side. Although strain measurements at location ZB and ZA had the same sign, the strain magnitudes differed greatly between the left and right side. Asymmetry between the two sides of the face was observed in all specimens.
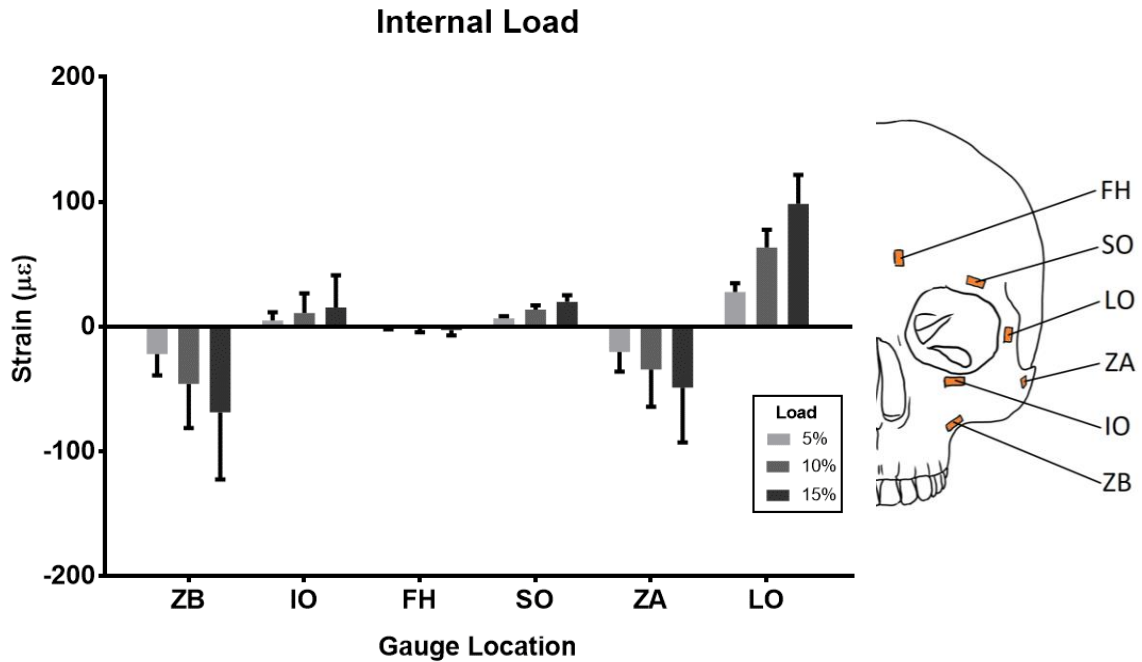
Figure 16. Average strain measurements of the five specimens under internal loads. Three bars correspond to 5%, 10%, and 15% of the physiological maximum load from left to right.

Table 4. Regression slope of strain measurements (με) from 0 to 15% internal load

Location	Slope	r^2
ZB	-466 ± 4.79	$> .99$
IO	104.9 ± 7.94	$> .99$
FH	-21.01 ± 1.47	$> .99$
SO	131.9 ± 6.22	$> .99$
ZA	-284.8 ± 1.40	$> .99$
LO	707 ± 4.09	$> .99$
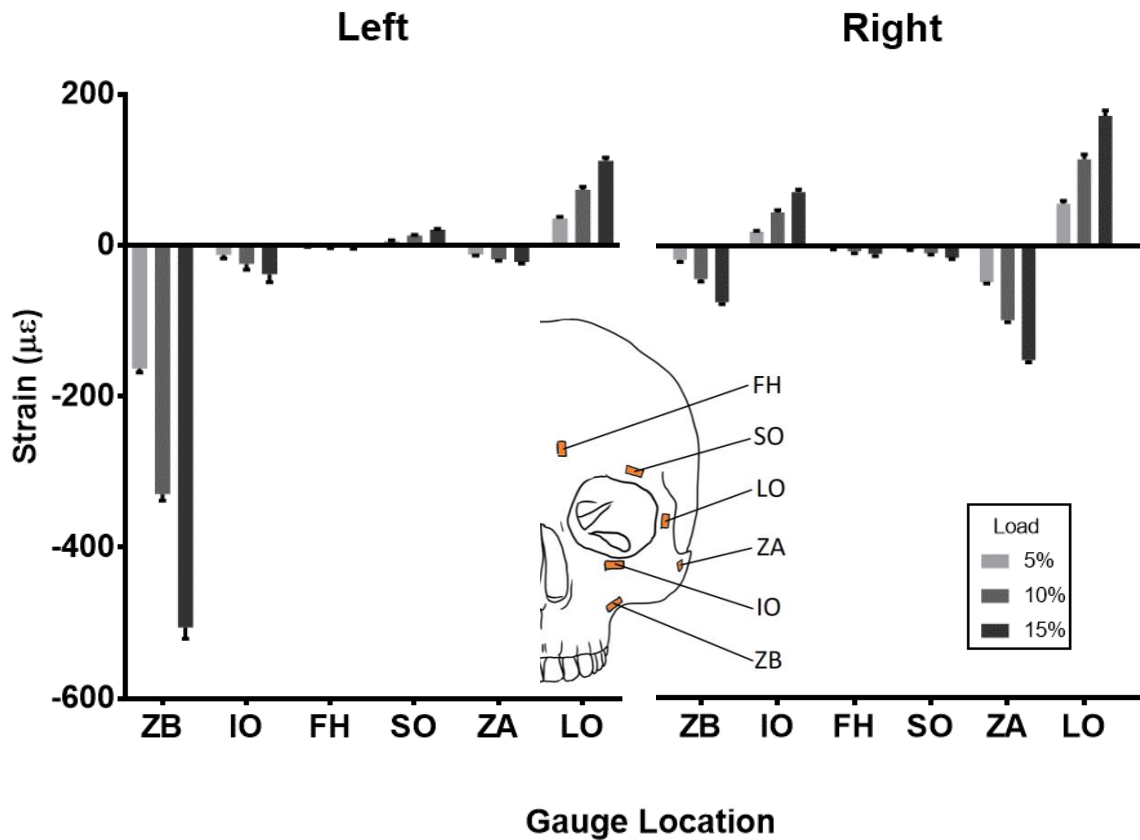
Figure 17. Strain measurements from the left and right side of Specimen 5. Three bars correspond to 5%, 10%, and 15% of the physiological maximum load from left to right.

3.1.2 Bone Strains under External Loads

Strain measurements under external load at 5%, 10%, and 15% of physiological maximum were obtained (Figure 18). There was an overall decrease in strain magnitude compared to measurements obtained under internal loads. Location IO, ZA, and LO saw similar trends compared to internal loads. Whereas, strain at location SO decreased in magnitude to a negligible level. Strain measurements went from compressive to tensile at location ZB. Strain measurements at all locations showed good linearity with increase in load. Regression slopes of strain measurements under external loads varied by location (Table 5).
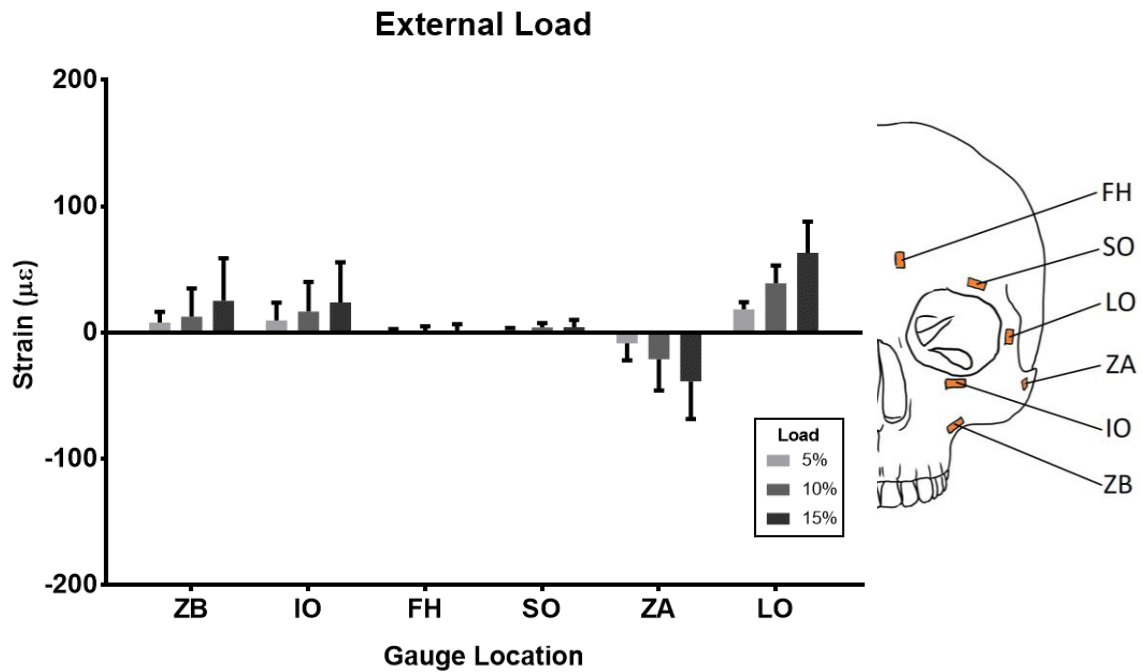
Figure 18. Average strain measurements of the five specimens under external loads. Three bars correspond to 5%, 10%, and 15% of the physiological maximum load from left to right.

Table 5. Regression slope of strain measurements from 0 to 15% external load

Location	Slope	r^2
ZB	173.4 ± 45.58	.94
IO	141.5 ± 0.90	$> .99$
FH	9.223 ± 3.75	.86
SO	23.29 ± 9.12	.87
ZA	-300.6 ± 27.28	$> .99$
LO	447 ± 18.55	$> .99$
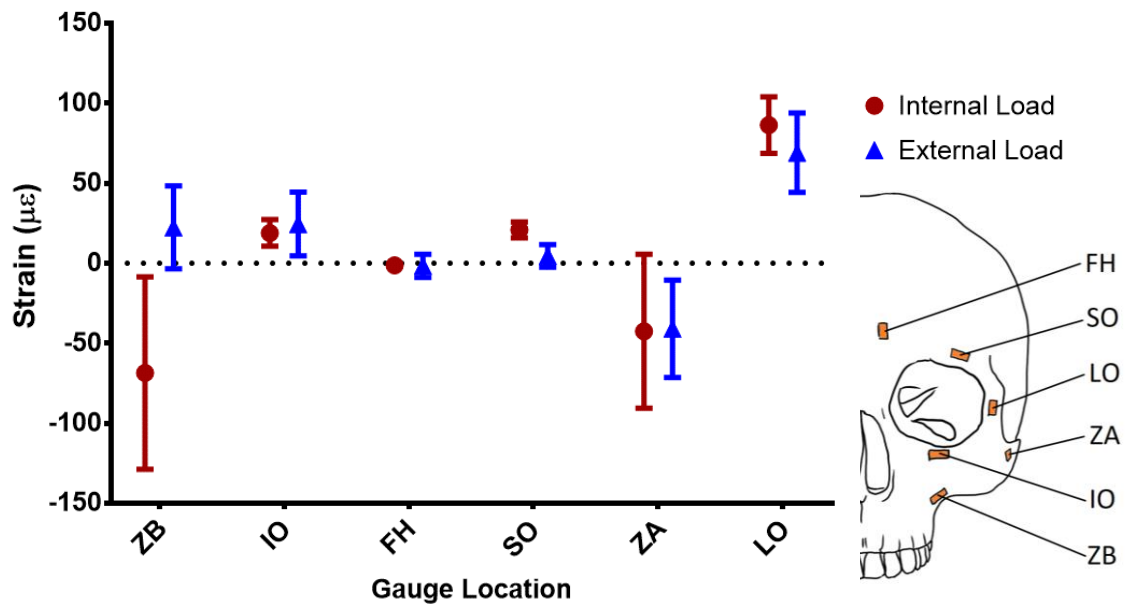
Figure 19. Strain measurements at 15% internal and external loads.

Between internal and external loads at 15% of the physiological maximum load, no significant differences were found at any location using RM-ANOVA (Figure 19).

There was a positive correlation between strain measurements at 15% internal and external loads, r = 0.715, n = 58, p < .001 (Pearson product moment). A scatterplot summarises the results (Figure 20). Overall, there was a strong positive correlation between strain measurements from 15% internal and external loads. Regression analysis calculated a slope of .529 ± .069.
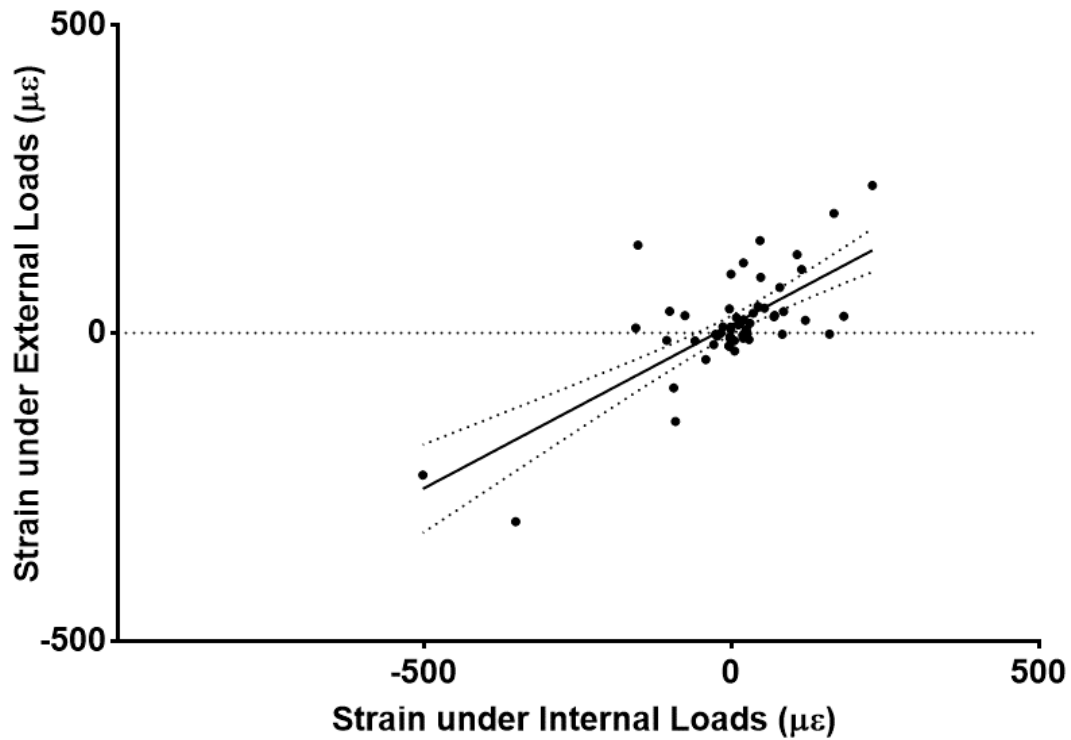
Figure 20. Scatter plot showing the correlation between strain measurements from internal and external loads. Regression line shows 95% CI.

3.1.3 Reliability

Reliability of strain measurements across the five specimens was evaluated using intraclass correlation coefficients (ICC).

Under 15% internal loads, ICC of .523 was .523 (95% CI: - .99 to .843) (Table 6), showing fair reliability within the five specimens. Under 15% external loads, ICC was .334 (95% CI: - .659 to .811) (Table 7), showing poor reliability within the five specimens.

Table 6. Intraclass correlation of consistency using 15% internal loads

	Intraclass Correlation	95% CI Lower Bound	95% CI Upper Bound	Sig
Single Measures	.180	-.018	.518	.041
Average Measures	.523	-.099	.843	.041

Table 7. Intraclass correlation of consistency using 15% external loads

	Intraclass Correlation	95% CI Lower Bound	95% CI Upper Bound	Sig
Single Measures	.091	-.086	.462	.185
Average Measures	.334	-.659	.811	.185

3.1.4 Bite Force

Bite force measurements were obtained under internal and external loads (Figure 21). Both internal and external loads produced highly linear bite force ($r^2 > .99$; $p < .01$). At 5%, 10%, and 15% internal loads, the measured bite forces were 37.6 ± 3.1 N, 79.6 ± 7.7 N, and 120.2 ± 13.7 N respectively. At 5%, 10%, and 15% external loads, the bite force measured were 36.7 ± 4.1 N, 78.0 ± 8.1 N, and 117.2 ± 11.0 N respectively. No significant differences were found between bite force measurements under internal and external loads at each load level using RM-ANOVA.
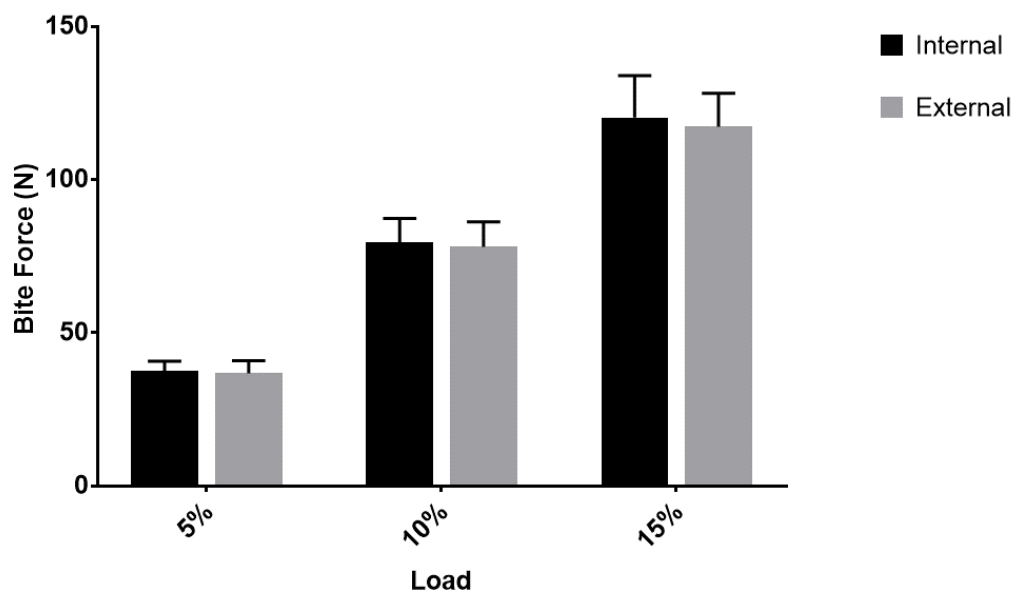
Figure 21. Bite force measurements under internal and external loads at 5%, 10%, and 15% of physiological maximum.

3.2 Results from Zygomatic Complex Fracture Repairs

3.2.1 Type 1 Fracture

Strain measurements were obtained from type 1 fractures repaired without an infraorbital rim plate (-IOP) (Phase 1) and with an infraorbital rim plate (+IOP) (Phase 2). The measurements were grouped by whether the side of the face was intact or with a fracture. Strain measurements from before the face was fractured (Phase 0) was used as the baseline. Measurements at 15% load were analysed.

On the intact side (Figure 22), strain measurements at location FH were higher in type 1 fractures (p = .034; observed power = .680). Pairwise comparison showed measurement in –IOP was 7.997 $\mu\epsilon$ higher than the baseline, the increase was small but was found to be significant (p = .046) using RM-ANOVA. No significant differences were found among the baseline, -IOP, and +IOP at any of the six strain gauge locations.
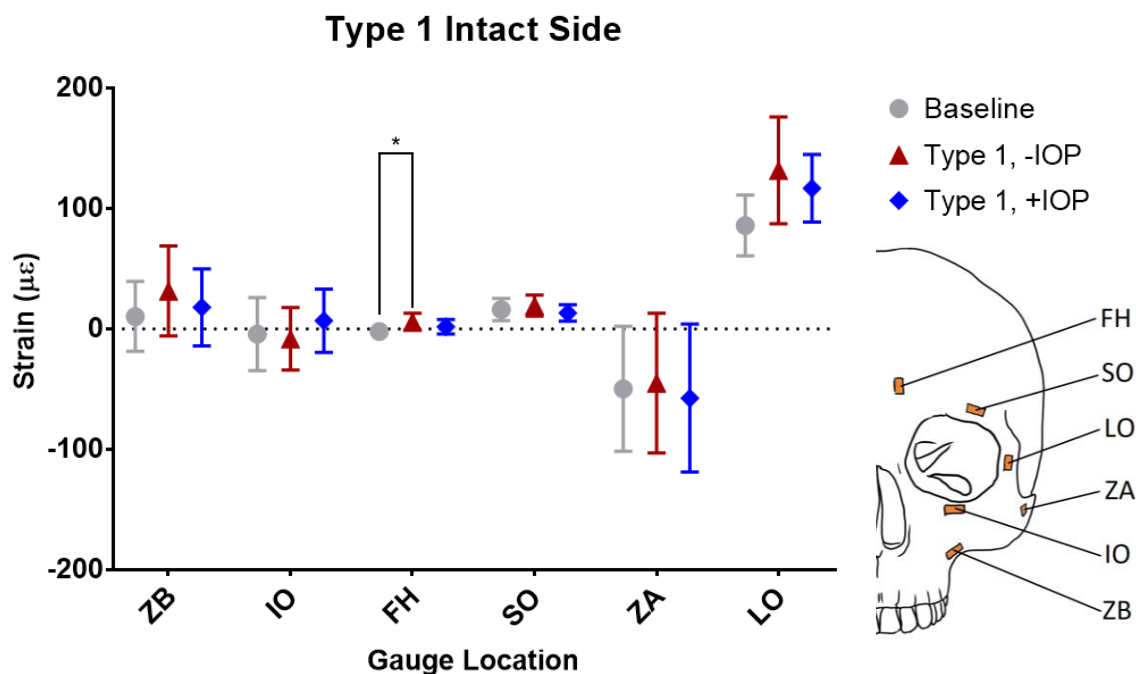
Figure 22. Strain measurements between baseline state, without infraorbital rim plate (-IOP), and with infraorbital rim plate (+IOP) on the intact side in type 1 fracture repair. * shows significant difference at p < .05.

On the fracture side, strain measurements at location FH were also higher in fracture repairs (p = .014; observed power = .828). A significant but small increase (p = .024) of 7.46 με was found at location FH in -IOP. At location SO on the fracture side, there was a significant increase in strain (p = .007; observed power = .941). The increase in -IOP was 26.96 με (p = .015). In +IOP, the increase was 25.10 με (p =.006). No significant differences were found among the baseline, -IOP, and +IOP at the other four strain gauge locations on the fracture side using RM-ANOVA (Figure 23).

The intact side was compared with the fracture side using Pearson product-moment correlation (Table 8). Strain measurements from homologous strain gauges across the face were plotted. The correlation between the intact and fracture side for baseline, -IOP, and +IOP were found to be weak. None of the three correlations was significant.
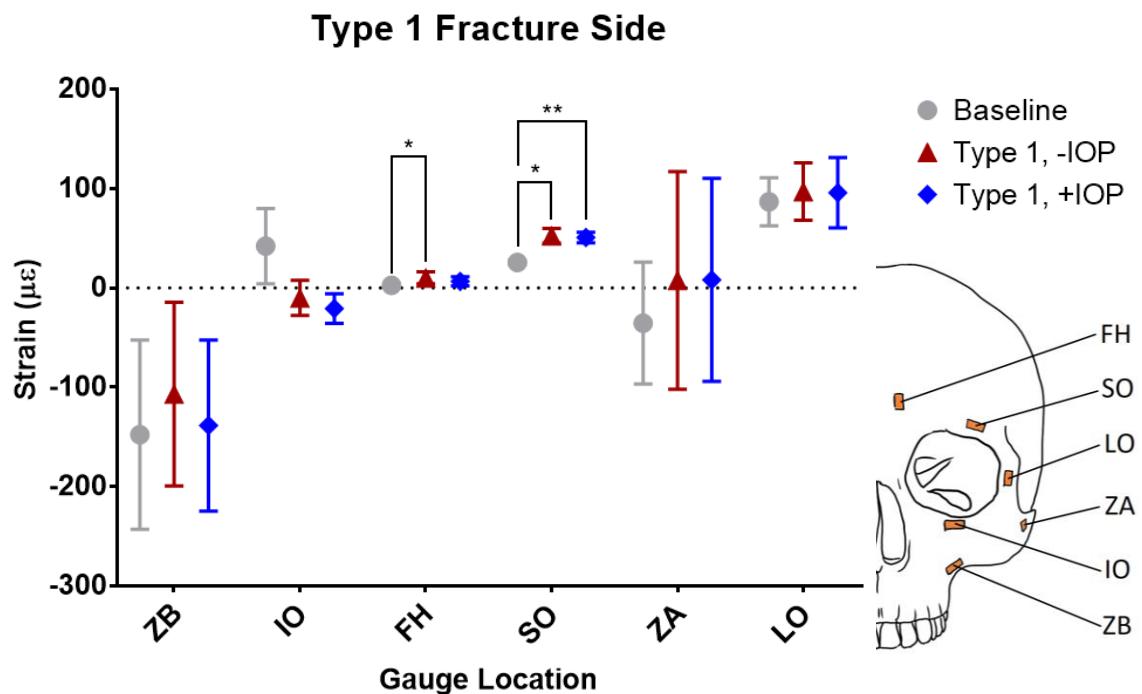
Figure 23. Strain measurements between baseline state, without infraorbital rim plate (-IOP), and with infraorbital rim plate (+IOP) on the fracture side in type 1 fracture repair. * shows significant difference at p < 0.05. ** shows significant difference at p < 0.01.

Table 8. Pearson product-moment correlation coefficients of strain measurements for type 1 fracture between intact and fracture side; baseline comparison for reference

Item	Pearson Coefficient (r)	p-Value (p)	Sample Size (n)
Baseline	.262	n.s.	30
-IOP	.258	n.s.	30
+IOP	.325	n.s.	30

The Pearson product-moment correlation coefficients between baseline and -IOP, and between baseline and +IOP were high when both sides of the face were considered (Table 9). The strain patterns of both repairs were similar to baseline. Regression slope between baseline and both -IOP and +IOP were less than, but close to 1 (Table 10). There was a 12.6% decrease in strain magnitude of –IOP compared to baseline, and a 1.5% decrease in strain magnitude of +IOP compared to baseline.

Table 9. Pearson product-moment correlation coefficients of strain measurements for type 1 fracture repairs against baseline

Item	Pearson Coefficient (r)	p-Value (p)	Sample Size (n)
Baseline vs -IOP	.803	< .001	60
Baseline vs +IOP	.810	< .001	60

Table 10. Regression slopes of strain measurements for type 1 fracture repairs against baseline

Item	Slope	Standard Error
Baseline vs -IOP	.874	.085
Baseline vs +IOP	.985	.094

On the intact side, the Pearson coefficient between baseline and +IOP was strong, but the correlation between baseline and -IOP was not as strong (Table 11). The regression slope between baseline and both -IOP and +IOP were very close or equal to 1 (Table 12). There was a 7.0% decrease in strain magnitude of –IOP compared to baseline, and no decrease in strain magnitude of +IOP compared to baseline.

Table 11. Pearson product-moment correlation coefficient of strain measurements on the intact side for type 1 fracture repairs against baseline

Item	Pearson Coefficient (r)	p-Value (p)	Sample Size (n)
Baseline vs -IOP	.722	< .001	30
Baseline vs +IOP	.829	< .001	30

Table 12. Regression slopes of strain measurements on the intact side for type 1 fracture repairs against baseline

Item	Slope	Standard Error
Baseline vs -IOP	.930	.168
Baseline vs +IOP	1.00	.128

On the fracture side, strong correlations were found between baseline and both -IOP and +IOP (Table 13). The regression slope between baseline and both -IOP and +IOP were both close to 1, with -IOP slightly lower (Table 14). There was a 14.1% decrease in strain magnitude of –IOP compared to baseline, and a 2.5% decrease in strain magnitude of +IOP compared to baseline.

Table 13. Pearson product-moment correlation coefficient of strain measurements on fracture side for type 1 fracture repairs against baseline

Item	Pearson Coefficient (r)	p Value (p)	Sample Size (n)
Baseline vs -IOP	.841	< .001	30
Baseline vs +IOP	.805	< .001	30

Table 14. Regression slopes of strain measurements on fracture side for type 1 fracture repairs against baseline

Item	Slope	Standard Error
Baseline vs -IOP	.859	.104
Baseline vs +IOP	.975	.136

3.2.1.1 Type 1 Fracture Summary

Statistical analysis showed a slight increase in tensile strains at location FH in -IOP on both sides of the face. On the fracture side, both -IOP and +IOP saw a similar moderate increase in tensile strain at location SO. Pearson product-moment correlation analysis

showed both repairs closely reproduced the baseline strain pattern. Regression analysis showed a slight decrease in overall strain magnitudes in both -IOP and +IOP repairs.

3.2.2 Type 2 Fracture

Strain measurements were obtained from type 2 fractures repaired without an infraorbital rim plate (-IOP) (Phase 4) and with an infraorbital rim plate (+IOP) (Phase 3). The measurements were grouped by whether the side of the face was intact or with a fracture. Strain measurements from before the face was fractured (Phase 0) was used as the baseline. Measurements at 15% load were analysed.

Baseline measurements showed asymmetry in strain between the two sides of the face. At location ZB, the strain was slightly tensile on the intact side (Figure 24), yet compressive on the fracture side (Figure 25). The opposite trend was seen at location IO.

On the intact side (Figure 24), a significant increase was found at location FH (p = .030; observed power = .691). However, the pairwise comparison did not find significant differences among baseline, -IOP, and +IOP at FH. No significant differences were found among the baseline, -IOP, and +IOP at the remaining five strain gauge locations using RM-ANOVA.

On the fracture side, there was an inversion of strain from tension to compression at location IO. This overall trend at location IO was significant (p = .016; observed power = .822); a significant change in strain of -94.72 $\mu\varepsilon$ and -112.2 $\mu\varepsilon$ was found between -IOP and +IOP respectively compared to the baseline. At location SO, strain increased in type 2 repairs (p = .042; observed power = .614). Pairwise comparison showed a significant increase of 18.97 $\mu\varepsilon$ from baseline in +IOP (p = .024), but the increase in -IOP was not found to be significant. No significant differences were found between the baseline, -IOP, and +IOP at the other four strain gauge locations on the fracture side using RM-ANOVA (Figure 25).
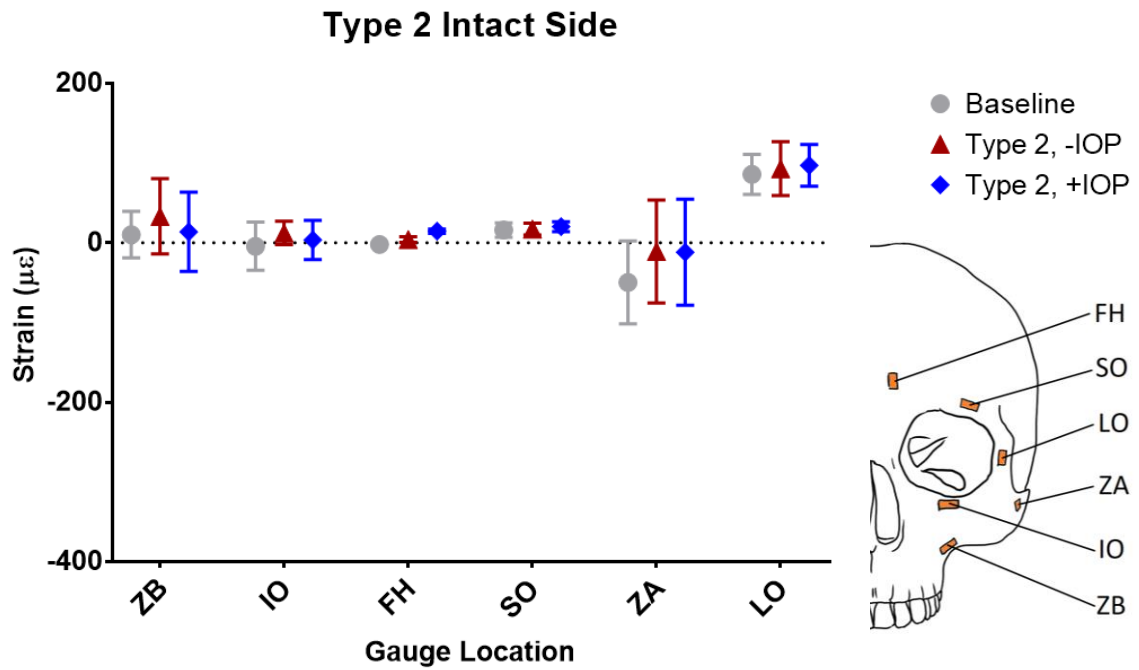
Figure 24. Strain measurements between baseline state, without infraorbital rim plate (-IOP), and with infraorbital rim plate (+IOP) on the intact side in type 2 fracture repair.
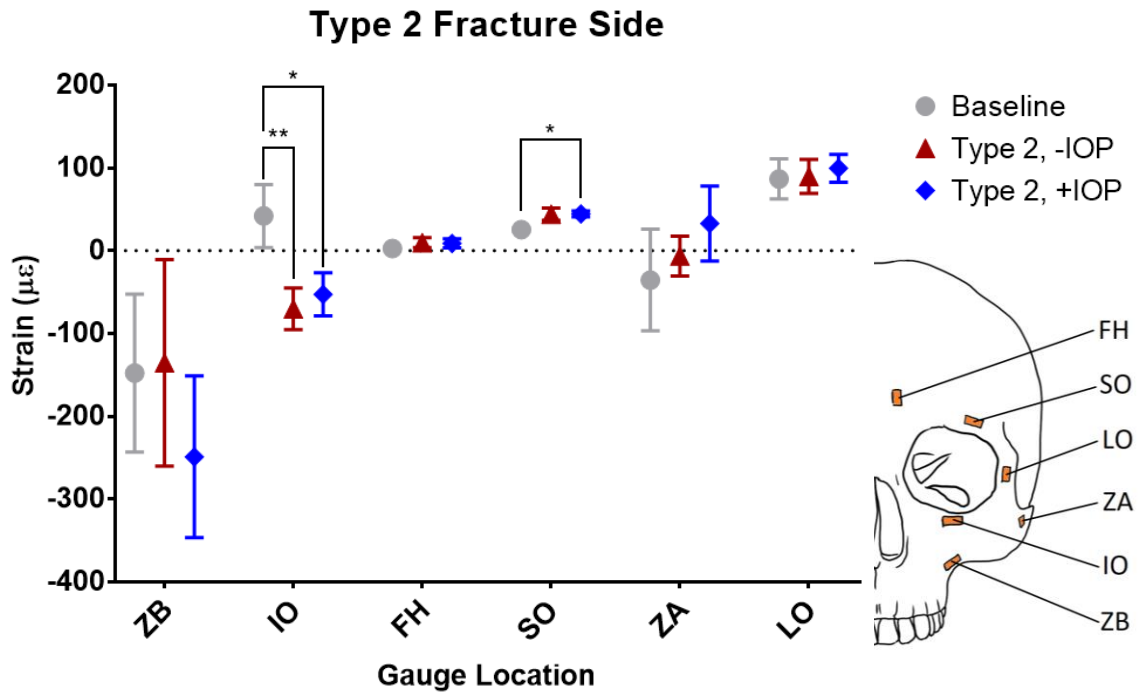
Figure 25. Strain measurements between baseline state, without infraorbital rim plate (-IOP), and with infraorbital rim plate (+IOP) on the fracture side in type 2 fracture repair. * shows significant difference at p < .05. ** shows significant difference at p < .01.

The intact side was compared with the fracture side using Pearson product-moment correlation (Table 15). Strain measurements from homologous strain gauges across the face were plotted against each other. The correlation between the intact and fracture side for baseline, -IOP, and +IOP were found to be weak. Only the correlation for -IOP was significant (p < .05).

Table 15. Pearson product-moment correlation coefficients of strain measurements for type 2 fracture between intact and fracture side; baseline comparison for reference

Item	Pearson Coefficient (r)	p-Value (p)	Sample Size (n)
Baseline	.262	n.s.	30
-IOP	.480	<.05	30
+IOP	.328	n.s.	30

Pearson coefficient of -IOP was comparable to the two type 1 fracture repairs; however, the Pearson coefficient of +IOP was lower than the rest of the repairs (Table 16). This implied that in type 2 fractures, -IOP had a strain pattern that closer reassemble baseline strain pattern. Regression slopes of both -IOP and +IOP in type 2 fractures were still high (Table 17), but considerably lower than that in type 1 fractures. There was a 19.2% decrease in strain magnitude of –IOP compared to baseline, and a 26.9% decrease in strain magnitude of +IOP compared to baseline.

Table 16. Pearson product-moment correlation coefficients of strain measurements for type 2 fracture repairs against baseline

Item	Pearson Coefficient (r)	p-Value (p)	Sample Size (n)
Baseline vs -IOP	.794	< .001	60
Baseline vs +IOP	.674	< .001	60

Table 17. Regression slopes of strain measurements for type 2 fracture repairs against baseline

Item	Slope	Standard Error
Baseline vs -IOP	.808	.081
Baseline vs +IOP	.731	.105

On the intact side, the correlation between baseline and -IOP and between baseline and +IOP were similar (Table 18). The correlations were moderately strong but were lower than those observed in type 1 fractures. Regression slopes of both -IOP and +IOP showed values close to 1 (Table 19). There was a 17.1% decrease in strain magnitude of –IOP compared to baseline, and a 14.0% decrease in strain magnitude of +IOP compared to baseline.

On the fracture side, despite -IOP showing a strong correlation with baseline, +IOP only showed moderately strong correlation (Table 20). The strain pattern in type 2 +IOP can only partially reassemble the baseline strain pattern. Regression slopes with -IOP were similar to other fracture repairs, while slope of +IOP showed decreased strain magnitudes (Table 21). There was a 20.6% decrease in strain magnitude of –IOP compared to baseline, and a 31.5% decrease in strain magnitude of +IOP compared to baseline.

Table 18. Pearson product-moment correlation coefficient of strain measurements on the intact side for type 2 fracture repairs against baseline

Item	Pearson Coefficient (r)	p-Value (p)	Sample Size (n)
Baseline vs -IOP	.776	< .001	30
Baseline vs +IOP	.766	< .001	30

Table 19. Regression slopes of strain measurements on the intact side for type 2 fracture repairs against baseline

Item	Slope	Standard Error
Baseline vs -IOP	.829	.127
Baseline vs +IOP	.860	.136

Table 20. Pearson product-moment correlation coefficient of strain measurements on fracture side for type 2 fracture repairs against baseline

Item	Pearson Coefficient (r)	p-Value (p)	Sample Size (n)
Baseline vs -IOP	.806	< .001	30
Baseline vs +IOP	.646	< .001	30

Table 21. Regression slopes of strain measurements on fracture side for type 2 fracture repairs against baseline

Item	Slope	Standard Error
Baseline vs -IOP	.794	.110
Baseline vs +IOP	.685	.153

3.2.2.1   Type 2 Fracture Summary

Strain measurements did not show a significant difference between baseline and either of the repairs on the intact side. On the fracture side, there was an inversion of strain from tension to compression at location IO. An increase of strain at location SO was also found on the fracture side. Pearson product-moment correlation analysis showed -IO strongly reproduced, while +IO only moderately reproduced the baseline strain pattern. Strain patterns in repaired type 2 fractures were not as close to the baseline as repaired type 1 fractures. Regression analysis showed a slight decrease in overall strain magnitudes in both -IOP and +IOP repairs in type 2 fractures.

3.2.3 Bite Force

Bite force measurements were obtained from all four fracture repairs (Figure 26). The measured bite force for baseline, type 1 -IOP, +IOP, type 2 -IOP, and +IOP were 120.2 ± 13.7 N, 129.1 ± 17.0 N, 126.9 ± 18.6 N, 133.4 ± 14.8 N, and 129.1 ± 17.0 N respectively. No significant differences were found among the bite forces.
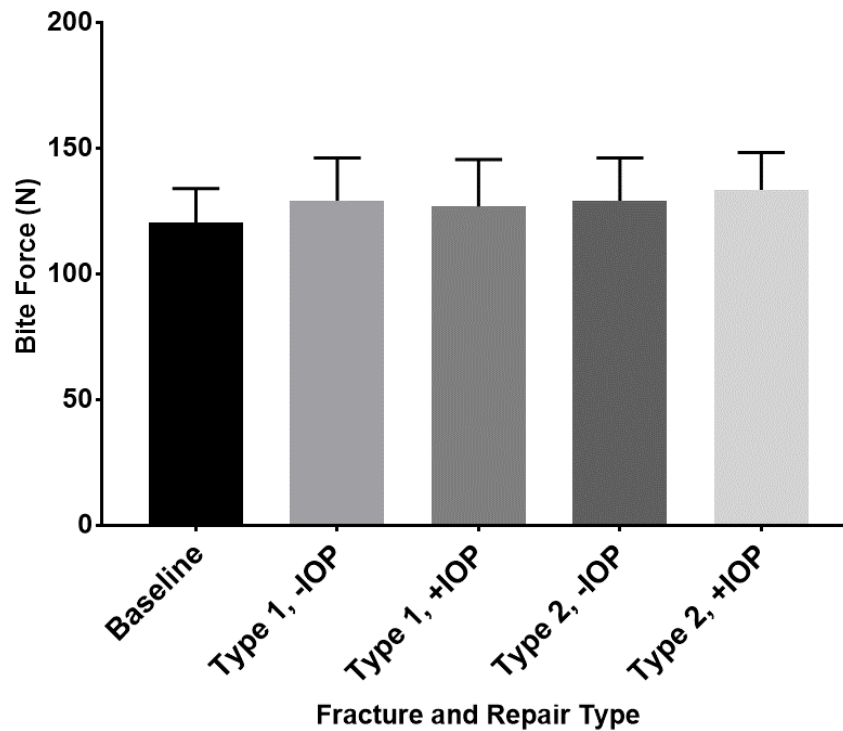
Figure 26. Bite force measurements in baseline and repaired fractures at 15% load.

3.2.4 External Loads in Fracture Repairs

Comparison between strain measurements under internal and external 15% loads in repaired fractures was made. Baseline measurements for when the specimens were without fractures are plotted in the background for reference.

On the intact side, no significant differences were found between strain measurements from internal and external loads in repaired fractures (Figure 27). At location IO, there was elevated tensile strain under external load when compared to baseline. At location

SO, there was an inversion of tensile strain to compressive strain, though the change was not found to be statistically significant.
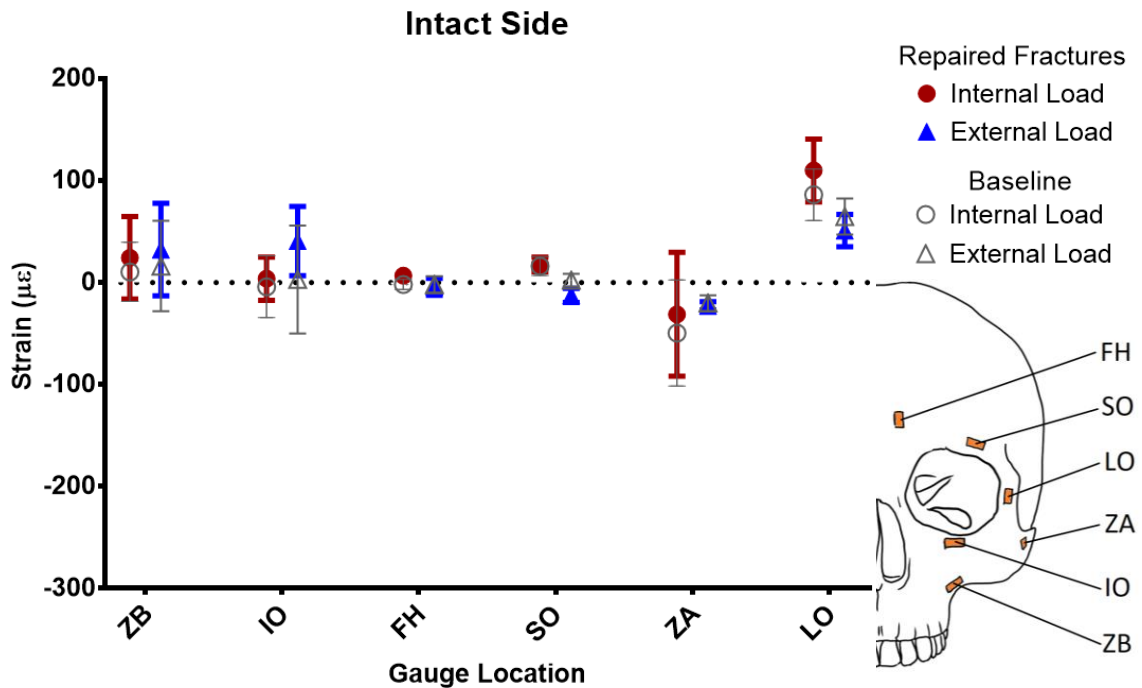
Figure 27. Strain measurements at 15% internal and external loads of all repaired fractures on the intact side. Corresponding values from the intact state (baseline) are shown for comparison.

On the fracture side, a significant difference was found at location SO ($p < .001$) between internal and external loads (Figure 28). There was a moderate tensile strain at location SO under internal load but decreased by 56.72 $\mu\varepsilon$ to a slight compression when under external load. On the other hand, location LO saw attenuation in strain under external load when compared to internal load, the change of 101.0 $\mu\varepsilon$ was found to be significant ($p = .01$).
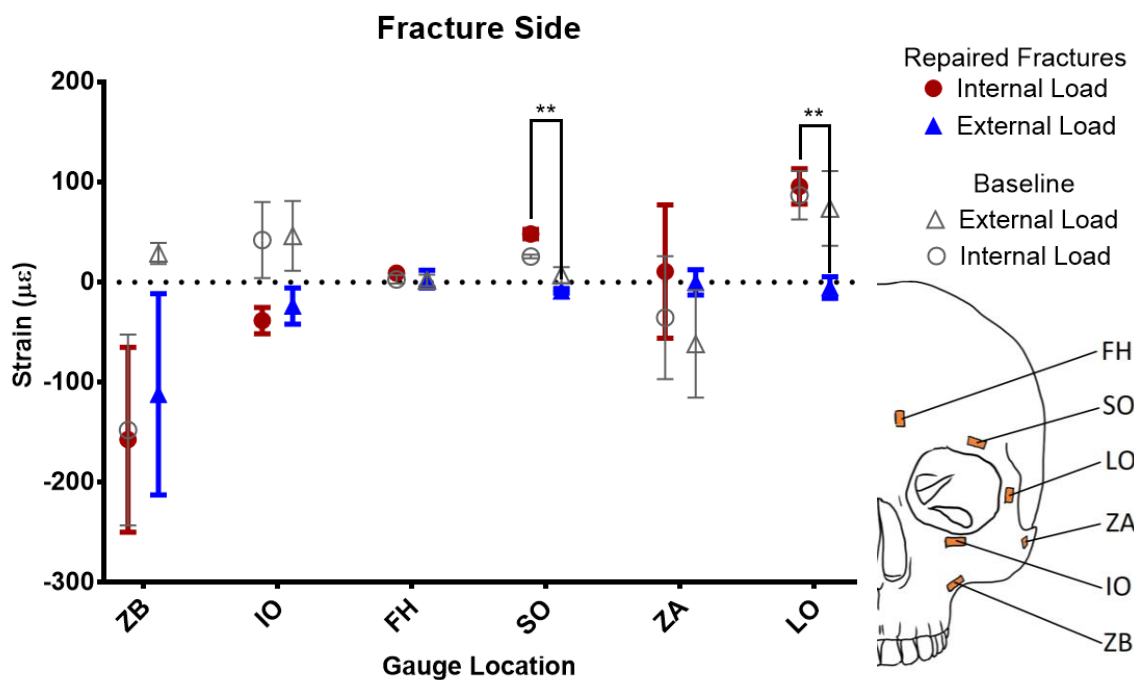
Figure 28. Strain measurements at 15% internal and external loads of all repaired fractures on the fracture side. ** shows significant difference at p < .01. Grey bars behind shows corresponding values from baseline.

A Pearson product-moment correlation coefficient was computed to assess the relationship between strain measurements from 15% internal and external loads in repaired fractures. There was a positive correlation between the two variables, $r = .494$, $n = 240$, $p < .001$. A scatterplot summarises the results (Figure 29). Overall, there was a weak, positive correlation between strain measurements from 15% internal and external loads. Regression analysis calculated a slope of $.6250 \pm .0712$. Compare to baseline (Figure 20), the correlation in strain measurements between internal and external loads was not as strong ($r_{fracture} = .494$ vs $r_{baseline} = .715$).
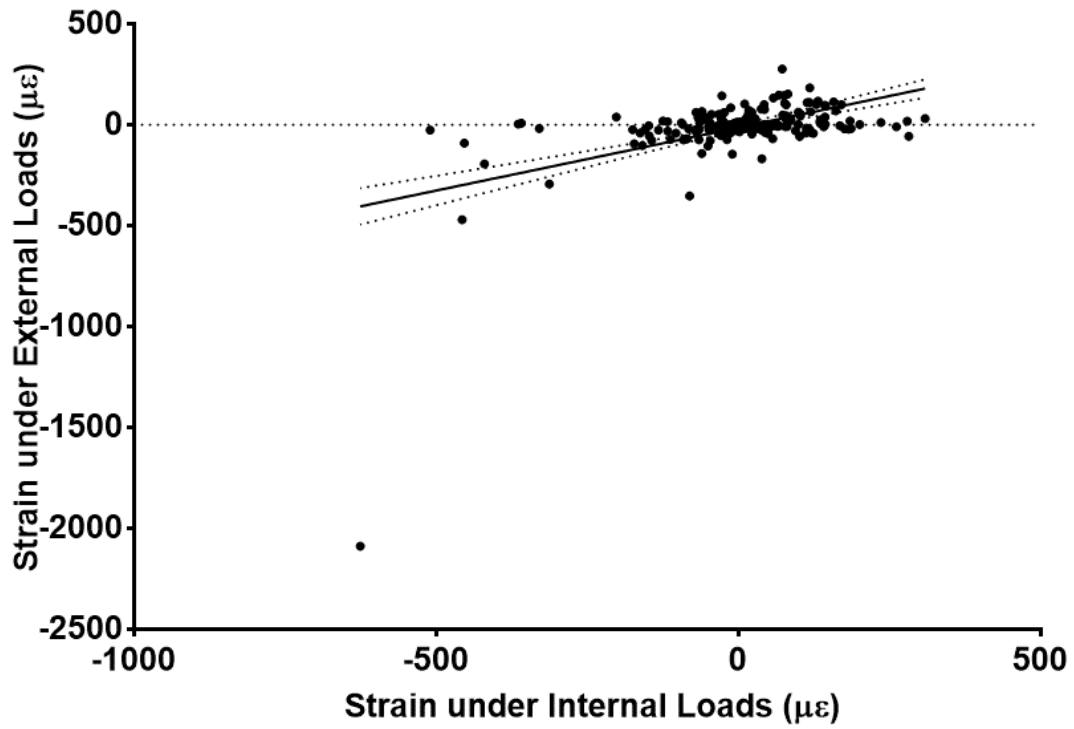
Figure 29. Scatter plot showing the correlation between strain measurements from internal and external loads of all repaired fractures. Regression line shows 95% CI.

Chapter 4

4 Discussion and Conclusion

4.1 Discussion

Craniofacial strains under masticatory loads are not well understood. Current simulators seldom use internal manipulation to apply force to the skull. The new TM force simulator, which reproduces masticatory forces internally rather than externally, provides a more physiologically accurate way to study craniofacial strains.

4.1.1 Baseline Measurements

4.1.1.1 Internal Load

Due to limitation in tendon strength, simulated muscle loads applied through pneumatic pistons were limited to 15% of the physiological maximum. Strain measurements under internal muscle loads were shown to be highly linear from 5% to 15% (Table 4). Assuming no failure occurs, the craniofacial structure is expected to stay within the linear region even at maximum muscle effort. This supports findings from a study where strain measurements in the maxilla were linear with load applied to the hard palate (Alberts et al., 2003). The bite force, used as an indicator for the overall output of the system, was also highly linear (Table 13). The simulator was shown to be a reliable system for measuring strain patterns in the craniofacial system given the linear relationships it produced in intact specimens. Strain and bite force measurements can thus likely be extrapolated to maximum physiological levels if needed.

Baseline strain measurements in individual specimens showed asymmetry across the two sides of the face (Figure 17). Experimental strain asymmetry at certain locations in the pilot specimen was confirmed with a computer model based on the same specimen; the computer model demonstrated that strain asymmetry can occur even with symmetrical piston force output (Appendix A). Such asymmetry in strain measurements was also observed in other in-vitro studies (Alberts et al., 2003; Endo, 1965, 1970). A computer simulation using a CT finite element model had also reported bilateral asymmetry in the craniofacial strains under masticatory load (Pakdel, Whyne, &Fialkov, 2017). While this

result may seem counterintuitive, the craniofacial skeleton, together with muscles of mastication, create an extremely complex loading system. Any deviation from symmetrical loading in-vivo may cause craniofacial bone morphology to change. The observed biased load transmission (left versus right) may have been caused by potential alterations in craniofacial structure. This has been previously discussed by Jian et al. (2015), where clinical results showed that asymmetry in physiological muscle output due to chewing-side preference led to asymmetry in TMJ structure. Similar morphological change in the rest of the craniofacial structure may ultimately result in uneven load sharing when a symmetrical load was applied.

The facial buttress theory suggests that the protruded lateral orbital rim acts as a column in the midface, resisting compressive force (Figure 1). In-vivo experiments in primates have shown tensile strains in the lateral orbital rim, which contradicted the theory (Hylander &Johnson, 1992; Oyen, Melugin, &Indresano, 1996; Oyen &Tsay, 1991). A validated finite element model of the human skull suggested that the lateral orbital rim was in bending, and experienced tensile strains under masticatory loads (Pakdel et al., 2017). In our experiment, baseline measurements showed tensile strains at the lateral orbit (location LO) under internal loads (Figure 16). This result was consistent with findings from the studies above. Clinical observation also supported these results, with fractured lateral orbital rims elongated through distraction osteogenesis caused by the tensile load (Barry et al., 2007). The tensile load transmission path continued to the lateral aspect of the superior orbital rim to a certain degree, as shown by the strain measured at the superior orbit (location SO). It is likely that the tensile strain on the lateral orbital rim resulted from the force from the masseter muscle pulling on the zygomatic complex. However, tensile strain was also observed in the lateral orbital rim when the craniofacial structure was under external load, where there was no muscle force acting on the zygoma (Figure 18). The presence of tensile strain under external loads suggests that the pattern was not only a result of muscle load, but also related to how the craniofacial structure naturally functions to transmit and distribute loads.

Both in-vitro experiments (Endo, 1965; Maloul et al., 2012) and finite element models (Janovic et al., 2015; Pakdel et al., 2017) have shown high compressive strains at the

zygomatic buttress of the maxilla. In the present study, average measurements from location ZB on the zygomatic buttress also showed high compressive strains under internal loads (Figure 16). However, strain measurements showed variations in both direction and magnitude: the strain gauge at location ZB experienced a range of small tensile strain to large compressive strain. The discrepancy in strain measurements at location ZB could potentially be explained by the complex strain pattern experienced by the area around the zygomatic buttress. Previous in-vitro experiments had demonstrated the direction and magnitude of principle strain varied greatly with a shift in the location of occlusal reaction load (Endo, 1965). Furthermore, the strain field in the area under internal load from a finite element model did not point in the same direction of the gauge (Pakdel et al., 2017). The finite element model suggested that the zygomaticomaxillary suture experienced a mix of compressive and shear loads rather than pure compressive loads. The combination of gauge alignment and sensitivity of strain to occlusal load in the area, make it possible to see such variation in strain measurements obtained from location ZB.

In our experiment, the measured strains in the infraorbital region (location IO) were predominantly tensile. Compared to location ZB, the measured strains at IO were lower in magnitude. The zygoma had been shown to have a tendency to rotate inferiorly on the axis of the zygomatic arch (Deveci et al., 2004). The rotation would have produced a distracting force on the superior portion of the zygomaticomaxillary buttress, where location IO was located. Although the rotation tendency of the zygoma might have produced some tensile strain, the mix of shear and compressive loads on the zygomaticomaxillary suture would also have superimposed at location IO. Similar to location ZB, it would not be surprising to see variation in strain measurements obtained from location IO due to the complex loads that went through the area.

4.1.1.2 External Load

The overall strain pattern was similar to baseline when the specimens were under external load compared to internal load, but the overall magnitude of strain under external load was less (Figure 20). Although the changes at individual locations between internal and external load were not found to be statically significant, these changes may still provide

insight on load distribution in the craniofacial structure under external load (Figure 19). The compressive strain at location ZB on the zygomatic buttress observed with internal loading was not observed with external loading, but rather a smaller tensile strain similar to that observed at location IO. The lack of muscle force removed a powerful contributor to the inferior rotation of the zygoma. The strain field around the zygomaticomaxillary buttress became solely driven by the occlusal load, leaving only measurable tensile strains in the directions of the gauges at location ZB and IO. On the other hand, the tensile strain observed at location LO decreased in magnitude under external load. Although the occlusal loads generated were the same, the results suggest that the load transfer in the midface have differences between internal and external load.

4.1.2 Fracture Repairs

4.1.2.1   Type 1 Fracture

The strain patterns from both repairs with and without the infraorbital rim plate (IOP) strongly reassembled that of the baseline state.

On the intact side, strains at individual locations were similar between baseline, -IOP, and +IOP. The tensile strain increased on the lateral orbital rim in both fracture repairs. The increase was not statistically significant but the reason for this increase was unknown. Although there was a significant increase in strain measurements at location FH in type 1 repairs, strain magnitude at location FH remained relatively low. A similar trend was observed at FH on the fracture side.

On the fracture side, compressive strain was observed at location ZB throughout. At location IO, the tension inverted to compression and decreased in magnitude after fractures were simulated. Based on the discussion of load transfer around the zygomatic buttress, the fracture would have taken away the ability for the zygomaticomaxillary suture to transfer shear loads. Only compressive load was allowed to go through the infraorbital region with or without the infraorbital rim plate. The change in loading mode in the infraorbital region of the zygomaticomaxillary suture may improve fracture healing, as studies had shown compressive load across a fracture gap to have less

negative effect on healing compare to a shear load (Steiner, Claes, Ignatius, Simon, &Wehner, 2014).

The tensile strain at location SO on the fracture side increased in both -IOP and +IOP repairs. Although the changes were not found to be statistically significant, it appeared that the tensile strain from the infraorbital rim was shifted to the superior orbit. The shift was possibly due to the reduced ability of the zygomaticomaxillary suture to resist shear load in a fracture repair, causing increase tensile load in the superior orbit to balance the forces acting on the zygomatic complex.

4.1.2.2   Type 2 Fracture

In type 2 fractures, strain patterns in -IOP repairs still strongly reassembled the baseline, while -IOP repairs only moderately reassemble the baseline. On the intact side, the strain pattern remained similar between baseline, -IOP, and +IOP. The increase in compressive strain at location FH in -IOP repairs had already been discussed under type 1 fractures. A similar increase in tensile strain on the lateral orbital rim in type 1 fracture repairs was also observed in type 2 fracture repairs.

On the fracture side, strain patterns similar to in type 1 repairs were observed in type 2 repairs. The strain reversal at location IO was even more drastic. There was also an increase in compressive strain at location ZB, though the increase was not deemed statistically significant. It is possible that the decrease in torsional stiffness in the zygomatic arch required more reaction force to counteract the rotational tendency of the zygoma under load, causing the increase in compressive strain in the infraorbital region.

4.1.2.3   External Loads in Fracture Repairs

The strain pattern in intact specimens under external loads was similar to the strain pattern under internal loads. However, this was not the case when specimens had repaired fractures; the strain pattern only showed a weak correlation between internal and external loads. On the intact side, there was a decrease in tensile strain in the lateral orbital rim. An inversion of tensile to compressive strain observed at location SO. Both locations adjacent to the zygomaticomaxillary suture, ZB and IO, measured tensile strains.

On the fracture side, compressive strains along the zygomaticomaxillary suture remained similar under external loads. There was a statistically significant decrease ($p< .05$) in tensile strain at location LO. The strains along the lateral orbital rim, at locations LO and SO, greatly decreased in magnitude under external load. An inversion of strain at SO was also observed, the difference in strain measurement between internal and external loads was statically significant on the fracture side. It appeared that in craniofacial structures with fractures, load transfer shifted medially and relied even more on the anterior medial naso-maxillary buttress. The greater shift caused compressive strains to be observed in the superior orbit.

It was surprising to see such departure in strain pattern under external load in repaired fractures, especially given the relatively high resemblance in intact specimens. An intact craniofacial structure could handle external load somewhat similar to the way it handles internal load. However, this ability was compromised in damaged craniofacial structure.

4.1.2.4 Clinical Significance

Based on the discussion on type 1 and type 2 fractures, the infraorbital rim plate (IOP) had no significant effect on local strain magnitudes, nor on the overall strain pattern. In all repairs, compressive strains were observed perpendicular to the zygomaticomaxillary suture. Such shift from shear to compressive strain may allow the fracture to heal better (Steiner et al., 2014). Repairs made with and without an IOP in both type 1 and type 2 fractures could reasonably reproduce the strain pattern of the intact state under masticatory loads.

It might be true that the IOP provides extra stability to a fractured zygomatic complex as suggested by some studies (Jank et al., 2003; Ramesh Candamourty &, M. F. Baig , M. R. Muthusekar, Manoj Kumar Jain, 2015; Rana et al., 2012). However, whether such stability is warranted to produce a satisfactory clinical result is still an active research area. Once the healing process takes over, new bone can start transferring load and the advantage in stability provided by the plate may potentially diminish. Moreover, the metallic fixation plate with high stiffness may provide good initial fixation to the fracture, but the plate also increases clinical risks such as bone atrophy from stress shielding, and

other well-documented issues associated with metallic fixation plates (Imola, Hamlar, Shao, Chowdhury, &Tatum, 2001). Nonetheless, the extra plate may be helpful in preventing catastrophic failure of the repair when met with traumatic external loads (Kasrai et al., 1999). Although only an external load mimicking occlusal load was simulated in the current study, results showed that the ability for a damaged craniofacial structure to dissipate external load was greatly compromised. There are also clinical scenarios where the infraorbital rim plates are necessary, such as in comminuted fractures where multiple bone fragments need to be bounded; a decision maker must carefully balance the potential benefit and risk related to the use of an infraorbital rim plate.

4.2 Hypotheses Revisited

Hypothesis 1: Strain patterns in the craniofacial structure are different under internal and equivalent external load.

Yes. Although the overall strain pattern in an intact craniofacial structure under external loads was similar to the strain pattern produced under internal loads, there were local differences found. The results suggested that load transfer shifted medially under external load and the effect was even more exaggerated in repaired craniofacial structure.

Hypothesis 2: Strain patterns in the craniofacial structure are different with and without infraorbital rim plate in type 1 zygomatic complex fracture.

No. Strain patterns from both repairs in type 1 fracture were able to strongly reassemble the baseline strain pattern from intact specimens. The two repairs are not expected to perform differently in a clinical setting. This may imply the infraorbital rim plate may not be needed in for a type 1 fracture repair.

Hypothesis 3: Strain patterns in the craniofacial structure are different with and without infraorbital rim plate in type 2 zygomatic complex fracture.

Yes. Strain patterns in type 2 repairs without the infraorbital rim plate was able to strongly reassemble the baseline strain pattern from intact specimens; whereas, repairs with the infraorbital rim plate only moderately reassemble the baseline strain pattern.

This may imply the infraorbital rim plate may not be needed in for a type 2 fracture repair.

4.3   Strengths and Limitations

In order to simulate masticatory forces internally, a reliable method was developed to attach actuators to a fresh-frozen cadaveric head. This set up ensured that the simulated loads were spread across the entire area of muscle attachment, similar to the loading scenario expected in-vivo. Nonetheless, there were limitations that arose from assumptions and simplifications made on the system.

Muscle force and bite force was shown to vary greatly between individuals, as previously shown (Pruim et al., 1980). The simulator preserved muscle attachments and lines of action through the use of 3D-printed specimen-specific pneumatic piston mounts reverse engineered from CT data. The simulated muscle forces applied to all the specimens were same in magnitude because it would have been impossible to determine specimen specific muscle force. Although estimated muscle force output differed from study to study, the relative force between the temporalis and masseter remained similar (Meyer et al., 1998). It could be inferred that the relative magnitude of measured strains at a location would remain similar regardless of the exact force used. It had been reported that masseter force output decreased in patients with zygomatic complex fractures, but the decrease was not well documented (Dal Santo, Ellis Iii, And, &Throckmorton, 1992). In the current fracture protocol, the same symmetrical, physiologically proportionate force continued to be applied as in the baseline protocol. This was done to present the "worst case" scenario with no decrease in muscle output, and to reduce the number of variables in the experiment.

Out of the four main muscles of mastication, only the temporalis and masseter muscles were simulated. The simplification was necessary because of the lack of space for hardware installation. With the omission of the other two muscles, the bite force, and hence the overall strain magnitude was expected to be lower. Superficial strain pattern was not expected to deviate much because the attachment of the pterygoid muscle was deep in the craniofacial structure.

The mounts and adhesive interface showed no sign of failure in a post-experiment inspection. There were concerns regarding stress concentrations in the bone at the screw holes. However, the screw holes are small relative to the mounts and the adhesive provided ample stress shielding to dissipate the stress concentration.

The Dacron line used for connecting the piston rod to the suture anchorage was wrapping around some piston mounts due to insufficient clearance (Figure 14). The wrapping introduced friction lost to the piston's force output, which may alter the simulated muscle load in unpredictable ways. The clearance issue was likely due to the failure to account for factors such as surface finish in the 3D printed mounts and thickness of adhesive during installation. In the future, more clearance should be provided for the Dacron lines during the design phase to compensate for potential deviation. The deviation in installed mounts in past specimens should be quantified to provide information for future mount design using techniques such as laser surface scanning.

Post-mortem soft tissue degradation caused a weakening in muscle tendons. Sutures attachment to the tendon created localised stress concentration at the tendon-suture interface. Experience with the pilot specimen showed force exceeding 15% of maximum physiological output would cause failure in the tendon-suture interface. Even at 15% load, failure occasionally occurred and required mid-experiment repair. In later specimens, a hole was drilled into the mandibular condyle for attaching the lines from the anterior and posterior temporalis pistons. The change mitigated the reliability issue with the temporalis insertion tendon, but the issue with the masseter origin where the other piston attached persisted. Another method for reproducing tendon attachment of the masseter may be required.

In the simulator, the anterior temporalis, posterior temporalis, and masseter pistons can individually be controlled by the computer program. It allows for high freedom when designing experiment. The simulator can apply asymmetrical load, tease out the effect of individual muscle pairs, and even reproduce force output in neurological pathologies that affect masticatory muscles. To the knowledge of the author, this simulator is first of its kind to provide such flexibility in a physiologically consistent way.

In the fracture protocol, osteotomies were performed using an abrasive cutting wheel. The cutting wheel inevitable removed bone material that was roughly equal to the width of the wheel. The gap, about 1 mm in width, was considered a small gap for a fracture fixation in a clinical setting (Claes, Augat, Suger, &Wilke, 1997). Although the gap was well within clinical range, the gap introduced variability in results. In the future, the size of the gap should be quantified and recorded to ensure consistency across specimens. On the other hand, a thinner steel blade can be used to further reduce the width of the gap, reducing potential variability from the gap.

Through the discussion, it came to show the complexity of load transfer within the craniofacial structure. The uniaxial strain gauge used for instrumentation could only measure strain in one direction. At locations where a simple tensile or compressive strain with no direction change expected, such as on the lateral orbital rim, a uniaxial strain gauge would perform well measuring the signal. At locations with complex loads, such as around the zygomaticomaxillary buttress, a uniaxial strain gauge would not be able to definitively describe the nature of the change in strain. Although rosette strain gauge could measure two-dimensional change in strain, it would occupy too large of a footprint where space was also needed for fixation plate.

The combination of inter- and intra-specimen variability was a great challenge in this study, as strain measurements not only varied greatly between the same location between specimens, but also varied between the two sides of the face within a specimen. Some differences were even in the compression-tension direction of the strain. The variation was likely caused by both anatomical differences and human error in strain gauge placement. Instead of comparing the change in average strain, the overall strain pattern was used as the main output measurement for comparing different conditions. Each strain gauge would serve as its own baseline, the overall correlation between two conditions among the 60 strain gauges in the five specimens acted a measure of similarity in strain pattern. It was assumed that the goal of a fracture repair was to restore the strain pattern to the intact craniofacial structure. A similar strain pattern would indicate similar load transfer, and also reduce the chance for bone resorption due to stress shielding (Queiroz, Sarmento, DeAzevedo, DeOliveira, &Bastos, 2014; Strömberg &Dalén, 1978). However,

the measurements only represented the strain pattern after initial fixation. The continuous change in craniofacial strain pattern due to bone healing and remodelling was not, and could not be accounted for. Similarly, the strain pattern measured was based on physiological masticatory loads. Although the scope of the study did not include unexpected, external traumatic loads on the craniofacial structure, these loads can cause catastrophic failure if they are not adequately managed by the fracture repair. Again, in-vitro study of failure seldom take bone healing and remodelling into account (Kasrai et al., 1999). There are other factors affecting the clinical outcome of a fracture repair, many of them are not biomechanical in nature. A decision maker should take a holistic view of factors involved when deciding on the method of repair.

4.4 Future Directions

The flexibility of the simulator provides freedom for researchers when designing experiments. Load response from individual muscles and asymmetric loads can be explored using the simulator. Results from these studies may yield insights on the biomechanics of neurological muscle pathologies. Other types of fractures in the midface can be investigated using a similar method. Efficacy of patient-specific craniofacial implant and dental hardware can also be tested using the simulator.

The reliability of the simulator can continuously be improved. During the experiment, the suture-tendon interface was prone to failing; mid-experiment repairs took heavy time cost. Using a surrogate, such as a strip of fabric (Endo, 1965), for the masseter origin tendon may improve reliability. Validation will be needed to ensure the surrogate is able to spread the load across the attachment area a tendon would.

The current study used strain and bite force as outcome measurements. In future studies, the location and orientation of strain gauges can be refined based on findings from the current study. Other instrumentation hardware and techniques discussed in 1.3.4, such as strain sensitive lacquer and DIC, can be considered for future studies.

Strain measurements collected from the study provides valuable in-vitro data for validating finite element models. The pneumatic piston mounts reverse engineered from

specimen CT scans allow for precise replication of boundary conditions in a finite element study. A validated finite element model will open up opportunities for in silico craniofacial biomechanics studies. Studies may include an examination of three-dimensional stress and strain field in a damaged craniofacial structure, which is not possible with the in-vitro model.

4.5   Conclusion

The temporomandibular force simulator is the first known simulator that internally replicates masticatory loads. The initial study validated the methodology for affixing pneumatic actuators to a fresh frozen cadaveric specimen. With 5 specimens, the simulator demonstrated the ability to reliability reproduce internal masticatory forces. It was found that strain pattern in the craniofacial structure was different under internal and external loads, the difference was more pronounced in a craniofacial structure with repaired fractures. For type 1 zygomatic complex fracture, there was no observable difference in the strain pattern between repairs done with and without an infraorbital rim plate. For type 2 zygomatic complex fracture, strain pattern in repair done without an infraorbital rim closer reassemble that from an intact craniofacial structure.

4.6   Conflict of Interest

DePuy Synthes Companies supplied the craniofacial modular fixation system used in the experiment, but was not involved in the experiment's inception, design, or data analysis.

References

Alberts, L. R., Phillips, K. O., Tu, H. K., Stinson, W. W., &Friedman, A. (2003). A biologic model for assessment of osseous strain patterns and plating systems in the human maxilla. *Journal of Oral and Maxillofacial Surgery*, *61*(1), 79–88. https://doi.org/10.1053/joms.2003.50013

Andrade, F. H., &McLoon, L. K. (2013). Masticatory Muscles. In *Craniofacial Muscles: A New Framework for Understanding the Effector Side of Craniofacial Muscle Control* (pp. 91–140). New York, NY: Springer.

Barry, C. P., Ryan, W. J., &Stassen, L. F. A. (2007). Anatomical Study of Factors Contributing to Zygomatic Complex Fracture Instability in Human Cadavers. *Plastic and Reconstructive Surgery*, *119*(2), 637–640. https://doi.org/10.1097/01.prs.0000239565.82612.56

Belinha, J., Jorge, R. M. N., &Dinis, L. M. J. S. (2013). A meshless microscale bone tissue trabecular remodelling analysis considering a new anisotropic bone tissue material law. *Computer Methods in Biomechanics and Biomedical Engineering*, *16*(11), 1170–1184. https://doi.org/10.1080/10255842.2012.654783

Bogusiak, K., &Arkuszewski, P. (2010). Characteristics and epidemiology of zygomaticomaxillary complex fractures. *Journal of Craniofacial Surgery*, *21*(4), 1018–1023. https://doi.org/10.1097/SCS.0b013e3181e62e47

Celebi, N., Rohner, E. C., Gateno, J., Noble, P. C., Ismaily, S. K., Teichgraeber, J. F., &Xia, J. J. (2011). Development of a mandibular motion simulator for total joint replacement. *Journal of Oral and Maxillofacial Surgery*, *69*(1), 66–79. https://doi.org/10.1016/j.joms.2010.05.085

Chakranarayan, A., Thapliyal, G. K., Sinha, R., &Suresh, M. P. (2009). Efficacy of two point rigid internal fixation in the management of zygomatic complex fracture. *Journal of Maxillofacial and Oral Surgery*, *8*(3), 265–9. https://doi.org/10.1007/s12663-009-0065-0

Choi, C. H., Kulinsky, L., Jun, J. S., &Kim, J. H. (2014). A numerical study of the spring-back phenomenon in bending with a rebar bending machine. *Advances in Mechanical Engineering*, *2014*. https://doi.org/10.1155/2014/959207

Claes, L., Augat, P., Suger, G., &Wilke, H. J. (1997). Influence of size and stability of the osteotomy gap on the success of fracture healing. *Journal of Orthopaedic Research*, *15*(4), 577–584. https://doi.org/10.1002/jor.1100150414

Cordey, J., &Gautier, E. (1999a). Strain gauges used in the mechanical testing of bones Part I: Theoretical and technical aspects. *Injury*, *30*(99), SA7-SA13. https://doi.org/10.1016/S0020-1383(99)00120-5

Cordey, J., &Gautier, E. (1999b). Strain gauges used in the mechanical testing of bones Part II: "In vitro" and "in vivo" technique. *Injury*, *30*, SA14-SA20. https://doi.org/10.1016/S0020-1383(99)00121-7

Dal Santo, F., Ellis Iii, E., And, T., &Throckmorton, G. S. (1992). The Effects of Zygomatic Complex Fracture on Masseteric Muscle Force. *J Oral Maxillofac Surg*, *50*, 791–799. Retrieved from https://ac-els-cdn-com.proxy1.lib.uwo.ca/0278239192902674/1-s2.0-0278239192902674-main.pdf?_tid=e9ef172d-ffa4-4894-80c1-66e84b19d0f2&acdnat=1527624863_c209da030f06d1fbc0512e5ce21dfa04

Dall'Ara, E., Peña-Fernández, M., Palanca, M., Giorgi, M., Cristofolini, L., &Tozzi, G. (2017). Precision of Digital Volume Correlation Approaches for Strain Analysis in Bone Imaged with Micro-Computed Tomography at Different Dimensional Levels. *Frontiers in Materials*, *4*. https://doi.org/10.3389/fmats.2017.00031

Daumas, B., Xu, W. L., &Bronlund, J. (2005). Jaw mechanism modeling and simulation. *Mechanism and Machine Theory*, *40*(7), 821–833. https://doi.org/10.1016/j.mechmachtheory.2004.12.011

DEForest, A.V, &Ellis, G. (1940). Brittle Lacquers as an Aid to Stress Analysis. *Journal of the Aeronautical Science*, *7*(5), 205–208.

Deveci, M., Eski, M., Gurses, S., Yucesoy, C. A., Selmanpakoglu, N., &Akkas, N. (2004). Biomechanical Analysis of the Rigid Fixation of Zygoma Fractures: An Experimental Study. *Journal of Craniofacial Surgery*, *15*(4), 595–602. https://doi.org/10.1097/00001665-200407000-00013

Endo, B. (1965). Distribution of stress and strain produced by the masticatory force. *The Journal of the Anthropological Society of Tokyo*, *73*, 123–136. Retrieved from https://www.jstage.jst.go.jp/article/ase1911/73/4/73_4_123/_pdf/-char/en

Endo, B. (1970). Analysis of Stresses around the Orbit Due to Masseter and Temporalis Muscles Respectively. *The Journal of Anthropological Society of Nippon*, *78*, 251–266. https://doi.org/10.1537/ase1911.78.251

Endo, B., &Suzuki, H. (1966). A Biomechanical Study of the Human Facial Skeleton by Means of Strain-Sensitive Lacquer. *Okajimas Fol. Anat. Jap*, *42*, 205–217.

Erdine, E., &Kallegias, A. (2017). Interwoven reinforced concrete structures: Integration of design and fabrication drivers through parametric design processes. *Design Studies*, *52*, 198–220. https://doi.org/10.1016/j.destud.2017.06.002

Erdmann, D., Follmar, K. E., DeBruijn, M., Bruno, A. D., Jung, S. H., Edelman, D., …Marcus, J. R. (2008). A retrospective analysis of facial fracture etiologies. *Annals of Plastic Surgery*, *60*(4), 398–403. https://doi.org/10.1097/SAP.0b013e318133a87b

Eski, M., Sahin, I., Deveci, M., Turegun, M., Isik, S., &Sengezer, M. (2006). A retrospective analysis of 101 zygomatico-orbital fractures. *Journal of Craniofacial Surgery*, *17*(6), 1059–1064. https://doi.org/10.1097/01.scs.0000235111.92988.b2

Hak, D. J., Toker, S., Yi, C., &Toreson, J. (2010). The Influence of Fracture Fixation Biomechanics on Fracture Healing. *Orthopedics*, *33*(10), 752–755. https://doi.org/10.3928/01477447-20100826-20

Hardt, N., &Kuttenberger, J. (2010). *Craniofacial trauma: Diagnosis and management. Craniofacial Trauma: Diagnosis and Management* (Vol. 5). https://doi.org/10.1007/978-3-540-33041-7

Holmes, K. D., &Matthews, B. L. (1989). Three-Point Alignment of Zygoma Fractures With Miniplate Fixation. *Archives of Otolaryngology--Head and Neck Surgery*, *115*(8), 961–963. https://doi.org/10.1001/archotol.1989.01860320071021

Hwang, K., &Kim, D. H. (2011). Analysis of zygomatic fractures. *Journal of Craniofacial Surgery*, *22*(4), 1416–1421. https://doi.org/10.1097/SCS.0b013e31821cc28d

Hylander, W. L., &Johnson, K. R. (1992). Strain gradients in the craniofacial region of primates. *The Biological Mechanisms of Tooth Movement and Craniofacial Adaptation.*, (January 1992), 559–569.

Imola, M. J., Hamlar, D. D., Shao, W., Chowdhury, K., &Tatum, S. (2001). Resorbable plate fixation in pediatric craniofacial surgery: long-term outcome. *Archives of Facial Plastic Surgery : Official Publication for the American Academy of Facial Plastic and Reconstructive Surgery, Inc. and the International Federation of Facial Plastic Surgery Societies*, *3*(2), 79–90. Retrieved from http://www.embase.com/search/results?subaction=viewrecord&from=export&id=L3 3482816%5Cnhttp://sfx.library.uu.nl/utrecht?sid=EMBASE&issn=15212491&id=d oi:&atitle=Resorbable+plate+fixation+in+pediatric+craniofacial+surgery%3A+long -term+outcome.&stitle=Arch+Fa

Islamoglu, K., Coskunfirat, O. K., Tetik, G., &Ozgentas, H. E. (2002). Complications and removal rates of miniplates and screws used for maxillofacial fractures. *Annals of Plastic Surgery*, *48*(3), 265–268. https://doi.org/10.1097/00000637-200203000-00006

Jank, S., Schuchter, B., Emshoff, R., Strobl, H., Koehler, J., Nicasi, A., …Baldissera, I. (2003). Clinical signs of orbital wall fractures as a function of anatomic location. *Oral Surgery, Oral Medicine, Oral Pathology, Oral Radiology, and Endodontics*, *96*(2), 149–153. https://doi.org/10.1016/S1079-2104(03)00317-2

Janovic, A., Saveljic, I., Vukicevic, A., Nikolic, D., Rakocevic, Z., Jovicic, G., …Djuric, M. (2015). Occlusal load distribution through the cortical and trabecular bone of the

human mid-facial skeleton in natural dentition: A three-dimensional finite element study. *Annals of Anatomy*, *197*, 16–23. https://doi.org/10.1016/j.aanat.2014.09.002

Ji, B., Wang, C., Song, F., Chen, M., &Wang, H. (2012). A new biomechanical model for evaluation of fixation systems of maxillofacial fractures. *Journal of Cranio-Maxillofacial Surgery*, *40*(5), 405–408. https://doi.org/10.1016/j.jcms.2011.07.011

Jiang, H., Li, C., Wang, Z., Cao, J., Shi, X., Ma, J., &Liu, H. (2015). Assessment of osseous morphology of temporomandibular joint in asymptomatic participants with chewing-side preference. *Journal of Oral Rehabilitation*, *42*(2), 105–112. https://doi.org/10.1111/joor.12240

Kan, J. P. M., Judge, R. B., &Palamara, J. E. A. (2014). In vitro bone strain analysis of implant following occlusal overload. *Clinical Oral Implants Research*, *25*(2). https://doi.org/10.1111/clr.12059

Kasrai, L., Hearn, T., Gur, E., &Forrest, C. R. (1999). A biomechanical analysis of the orbitozygomatic complex in human cadavers: examination of load sharing and failure patterns following fixation with titanium and bioresorbable plating systems. *The Journal of Craniofacial Surgery*, *10*(3), 237–43. https://doi.org/10.1097/00001665-199905000-00012

Knight, B. J. S., Ph, D., North, J. F., &Chir, B. (1961). The classification of malar fractures: an analysis of displacement as a guide to treatment. *British Journal of Plastic Surgery*, *13*, 325–339. https://doi.org/10.1016/S0007-1226(60)80063-X

Kovács, A. F., &Ghahremani, M. (2001). Minimization of zygomatic complex fracture treatment. *International Journal of Oral and Maxillofacial Surgery*, *30*(5), 380–383. https://doi.org/10.1054/ijom.2001.0131

Kristensen, S., &Tveterås, K. (1986). Zygomatic fractures: classification and complications. *Clinical Otolaryngology & Allied Sciences*, *11*(3), 123–129. https://doi.org/10.1111/j.1365-2273.1986.tb02003.x

Kubota, Y., Kuroki, T., Akita, S., Koizumi, T., Hasegawa, M., Rikihisa, N., …Satoh, K.

(2012). Association between plate location and plate removal following facial fracture repair. *British Journal of Plastic Surgery*, *65*, 372–378. https://doi.org/10.1016/j.bjps.2011.09.040

Lee, J. D., Chen, Y., Zeng, X., Eskandarian, A., &Oskard, M. (2007). Modeling and simulation of osteoporosis and fracture of trabecular bone by meshless method. *International Journal of Engineering Science*, *45*(2–8), 329–338. https://doi.org/10.1016/j.ijengsci.2007.03.007

Llandro, H., &Langford, R. (2015). Reasons for plate removal after treatment of orbitozygomatic complex fractures. *Journal of Cranio-Maxillofacial Surgery*, *43*(1), 17–20. https://doi.org/10.1016/j.jcms.2014.10.003

Logan, B. M., Reynolds, P. A., Hutchings, R. T., &McMinn, R. M. H. (2010). Skull and skull bone articulations. In *McMinn's color atlas of head and neck anatomy* (4th ed., pp. 10–18). Philadelphia, PA: Mosby/Elsevier.

Maloul, A., Regev, E., Whyne, C. M., Beek, M., &Fialkov, J. A. (2012). In Vitro Quantification of Strain Patterns in the Craniofacial Skeleton Due to Masseter and Temporalis Activities. *Journal of Craniofacial Surgery*, *23*(5), 1529–1534. https://doi.org/10.1097/SCS.0b013e31825e3ccd

Marques, M., Belinha, J., Dinis, L. M. J., &Natal Jorge, R. (2018). A brain impact stress analysis using advanced discretization meshless techniques. *Proceedings of the Institution of Mechanical Engineers, Part H: Journal of Engineering in Medicine*, *232*(3), 257–270. https://doi.org/10.1177/0954411917751559

Maturo, S., &Lopez, M. A. (2008). Zygomatico-orbito-maxillary complex fractures. *Operative Techniques in Otolaryngology - Head and Neck Surgery*, *19*(2), 86–89. https://doi.org/10.1016/j.otot.2008.04.004

Meyer, C., Kahn, J. L., Boutemy, P., &Wilk, A. (1998). Determination of the external forces applied to the mandible during various static chewing tasks. *Journal of Cranio-Maxillo-Facial Surgery*, *26*(5), 331–341. https://doi.org/10.1016/S1010-

5182(98)80064-4

Miloro, M., Ghali, G. E., Larsen, P. E., &Waite, P. D. (2011). Peterson's Principles of Oral And Maxillofacial Surgery. *People's Medical Publishing House-USA*, 1502. https://doi.org/8005687281

Nagae, M., Bérzin, F., Alves, M. C., &Bérzin, M. da G. R. (2011). How the anterior, middle and posterior portions of the temporalis muscle work during mastication. *Brazilian Journal of Oral Sciences*, *10*(3), 213–216.

Oyen, O. J., Melugin, M. B., &Indresano, A. T. (1996). Strain gauge analysis of the frontozygomatic region of the zygomatic complex. *Journal of Oral and Maxillofacial Surgery*, *54*(9), 1092–1096. https://doi.org/10.1016/S0278-2391(96)90167-6

Oyen, O. J., &Tsay, T. P. (1991). A biomechanical analysis of craniofacial form and bite force. *American Journal of Orthodontics and Dentofacial Orthopedics*, *99*(4), 298–309. https://doi.org/10.1016/0889-5406(91)70012-L

Ozkaya, O., Turgut, G., Kayali, M. U., Ugurlu, K., Kuran, I., &Bas, L. (2009). A retrospective study on the epidemiology and treatment of maxillofacial fractures. *Ulusal Travma ve Acil Cerrahi Dergisi = Turkish Journal of Trauma & Emergency Surgery : TJTES*, *15*(3), 262–266. Retrieved from http://www.ncbi.nlm.nih.gov/pubmed/19562549

Pakdel, A. R., Whyne, C. M., &Fialkov, J. A. (2017). Structural biomechanics of the craniomaxillofacial skeleton under maximal masticatory loading: Inferences and critical analysis based on a validated computational model. *Journal of Plastic, Reconstructive & Aesthetic Surgery*, *70*(6), 842–850. https://doi.org/10.1016/j.bjps.2017.01.021

Palanca, M., Bodey, A. J., Giorgi, M., Viceconti, M., Lacroix, D., Cristofolini, L., &Dall'Ara, E. (2017). Local displacement and strain uncertainties in different bone types by digital volume correlation of synchrotron microtomograms. *Journal of*

Biomechanics, *58*, 27–36. https://doi.org/10.1016/j.jbiomech.2017.04.007

Perren, S. M. (2002). Evolution of the internal fixation of long bone fractures: The scientific basis of biological internal fixation: choosing a new balance between stability and biology. *The Journal of Bone and Joint Surgery*, *84*(8), 1093–1110. https://doi.org/10.1302/0301-620X.84B8.13752

Pruim, G. J., deJongh, H. J., &tenBosch, J. J. (1980). Forces acting on the mandible during bilateral static bite at different bite force levels. *Journal of Biomechanics*, *13*(9), 755–763. https://doi.org/10.1016/0021-9290(80)90237-7

Queiroz, C. S., Sarmento, V. A., DeAzevedo, R. A., DeOliveira, T. F. L., &Bastos, L. C. (2014). A comparative study of internal fixation and intermaxillary fixation on bone repair of mandibular fractures through radiographic subtraction. *Journal of Cranio-Maxillofacial Surgery*, *42*(5), e152–e156. https://doi.org/10.1016/j.jcms.2013.07.013

Ramesh Candamourty, V. N., &, M. F. Baig , M. R. Muthusekar, Manoj Kumar Jain, R. M. R. B. (2015). Treatment modalities in zygomatic complex fractures: A prospective short clinical study. *Dentistry and Medical Research*, *12*(1), 73–78. Retrieved from http://www.dmrjournal.org/temp/DentMedRes1113-5537531_152255.pdf

Rana, M., Warraich, R., Tahir, S., Iqbal, A., vonSee, C., Eckardt, A. M., &Gellrich, N. C. (2012). Surgical treatment of zygomatic bone fracture using two points fixation versus three point fixation-a randomised prospective clinical trial. *Trials*, *13*(36). https://doi.org/10.1186/1745-6215-13-36

Rossman, T., Uthamaraj, S., Rezaei, A., Mceligot, S., Giambini, H., Jasiuk, I., …Dragomir-Daescu, D. (2017). A Method to Estimate Cadaveric Femur Cortical Strains During Fracture Testing Using Digital Image Correlation Video Link. *J. Vis. Exp*, *54942*(10). https://doi.org/10.3791/54942

Sasaki, K., Hannam, A. G., &Wood, W. W. (1989). Relationships Between the Size, Position, and Angulation of Human Jaw Muscles and Unilateral First Molar Bite

Force. *Journal of Dental Research*, *68*(3), 499–503. https://doi.org/10.1177/00220345890680031401

Soons, J., Lava, P., Debruyne, D., &Dirckx, J. (2012). Full-field optical deformation measurement in biomechanics: Digital speckle pattern interferometry and 3D digital image correlation applied to bird beaks. *Journal of the Mechanical Behavior of Biomedical Materials*, *14*, 186–191. https://doi.org/10.1016/j.jmbbm.2012.05.004

Steiner, M., Claes, L., Ignatius, A., Simon, U., &Wehner, T. (2014). Disadvantages of interfragmentary shear on fracture healing - Mechanical insights through numerical simulation. *Journal of Orthopaedic Research*, *32*(7), 865–872. https://doi.org/10.1002/jor.22617

Strömberg, L., &Dalén, N. (1978). Atrophy of cortical bone caused by rigid internal fixation plates: An experimental study in the dog. *Acta Orthopaedica*, *49*(5), 448–456. https://doi.org/10.3109/17453677808993261

Sutradhar, A., Park, J., Carrau, D., &Miller, M. J. (2014). Experimental validation of 3D printed patient-specific implants using digital image correlation and finite element analysis. *Computers in Biology and Medicine*, *52*, 8–17. https://doi.org/10.1016/j.compbiomed.2014.06.002

Sztefek, P., Vanleene, M., Olsson, R., Collinson, R., Pitsillides, A. A., &Shefelbine, S. (2010). Using digital image correlation to determine bone surface strains during loading and after adaptation of the mouse tibia. *Journal of Biomechanics*, *43*(4), 599–605. https://doi.org/10.1016/j.jbiomech.2009.10.042

Taicher, S., Ardekian, L., Samet, N., Shoshani, Y., &Kaffe, I. (1993). Recovery of the infraorbital nerve after zygomatic complex fractures: a preliminary study of different treatment methods. *Int J Oral Maxillofac Surg*, *22*(6), 339–341. Retrieved from http://www.ijoms.com/article/S0901-5027(05)80662-9/abstract

Takanobu, H., Takanishi, a., &Kato, I. (1993). Design of a mastication robot mechanism using a human skull model. *Proceedings of 1993 IEEE/RSJ International*

Conference on Intelligent Robots and Systems (IROS '93), *1*(C), 203–208.
https://doi.org/10.1109/IROS.1993.583099

Tavares, J., &Jorge, N. (2012). *Meshless Method in Biomechanics*.
https://doi.org/10.1007/978-94-007-4174-4

Tozzi, G., Danesi, V., Palanca, M., &Cristofolini, L. (2016). Elastic Full-Field Strain
Analysis and Microdamage Progression in the Vertebral Body from Digital Volume
Correlation. *Strain*, *52*(5), 446–455. https://doi.org/10.1111/str.12202

vanEijden, T. M. G. J., Klok, E. M., Weijs, W. A., &Koolstra, J. H. (1988). Mechanical
capabilities of the human jaw muscles studied with a mathematical model. *Archives
of Oral Biology*, *33*(11), 819–826. https://doi.org/10.1016/0003-9969(88)90106-9

VanEijden, T. M. G. J., Koolstra, J. H., &Brugman, P. (1996). Three-dimensional
structure of the human temporalis muscle. *Anatomical Record*, *246*(4), 565–572.
https://doi.org/10.1002/(SICI)1097-0185(199612)246:4<565::AID-AR17>3.0.CO;2-
M

vanEijden, T. M. G. J., Korfage, J. A. M., &Brugman, P. (1997). Architecture of the
human jaw-closing and jaw-opening muscles. *Anatomical Record*, *248*(3), 464–474.
https://doi.org/10.1002/(SICI)1097-0185(199707)248:3<464::AID-AR20>3.0.CO;2-
M

VonWilmowsky, C., Bergauer, B., Nkenke, E., Neukam, F. W., Neuhuber, W., Lell, M.,
…Matta, R. E. (2015). A new, highly precise measurement technology for the in
vitro evaluation of the accuracy of digital imaging data. *Journal of Cranio-
Maxillofacial Surgery*, *43*(8), 1335–1339.
https://doi.org/10.1016/j.jcms.2015.06.021

Wang, H., Chen, M. S., Fan, Y. B., Tang, W., &Tian, W. D. (2007). Biomechanical
Evaluation of Le Fort I Maxillary Fracture Plating Techniques. *Journal of Oral and
Maxillofacial Surgery*, *65*(6), 1109–1116.
https://doi.org/10.1016/j.joms.2006.10.020

Weijs, W., &Hillen, B. (1985). Cross-sectional areas and estimated intrinsic strength of the human jaw muscles. *Acta Morphologica Neerlando-Scandinavica*, *23*(3), 267–74. Retrieved from http://www.ncbi.nlm.nih.gov/pubmed/4096273

Wood, D. (1980). Fractures of the zygoma. A geometric, biomechanical and surgical analysis. *Plastic and Reconstructive Surgery*, *65*(5), 702. https://doi.org/10.1097/00006534-198005000-00058

Woods, J. J., &Bigland-Ritchie, B. (1983). Linear and non-linear surface EMG/force relationships in human muscles. An anatomical/functional argument for the existence of both. *American Journal of Physical Medicine*, *62*(6), 287–99. Retrieved from http://www.ncbi.nlm.nih.gov/pubmed/6650674

Zingg, M., Chowdhury, K., Lädrach, K., Vuillemin, T., Sutter, F., &Raveh, J. (1991). Treatment of 813 Zygoma-Lateral Orbital Complex Fractures: New Aspects. *Archives of Otolaryngology--Head and Neck Surgery*, *117*(6), 611–620. https://doi.org/10.1001/archotol.1991.01870180047010

Zingg, M., Laedrach, K., Chen, J., Chowdhury, K., Vuillemin, T., Sutter, F., &Raveh, J. (1992). Classification and Treatment of Zygomatic Fractures: *Journal of Oral and Maxillofacial Surgery*, *50*, 779–790.

Appendices

Appendix A: Finite Element Model

Introduction

There are many studies that examined stress and strain fields in the human skull. Finite element (FE) models of the skull are often generated from clinical-resolution CT images. In older models, the number of elements and nodes in a model is limited due to restrictions in computational resources. The result is finite element models that are unable to represent complex geometries in the skull (Prado et al. 2014). Details in thin bony structures, such as those in the facial sinus, are often lost. In these models, either homogenous material property was applied to the entire model (Gross, Arbel, and Hershkovitz 2001), or two different material properties were applied to cortical and trabecular bone (Chalk et al. 2011). Furthermore, many of these FE models were not experimentally validated.

A recent model used computer algorithms to preserve contrast between thin bone structures and surrounding tissues (Pakdel, Fialkov, and Whyne 2016). In the same model, heterogenous material properties were mapped to elements based on CT intensity. The study also validated the FE model with in-vitro experimental results (Maloul et al. 2012). This model, however, requires custom image processing software for element and material property mapping. The study also reported long solution computing time of 8 hours for each load case. The complicated model generation process and long solution time, prohibits the model to be used for an application that requires frequent modifications, such as in the iterative design process of a patient-specific implant.

In traditional finite element models, systematic elements and nodes are mapped to the geometries to generate a meshed model. In meshless methods, there is no "mesh" because nodes are arbitrary distributed across the model using the theory of external approximation (Belytschko et al. 1996; Gu 2005; Tavares and Jorge 2012). Because there is no mesh involved, the time required to generate the model is significantly reduced.

Meshless analysis in biomechanics relied on custom computer software (Belinha, Jorge, &Dinis, 2013; Lee, Chen, Zeng, Eskandarian, &Oskard, 2007; Marques, Belinha, Dinis, &Natal Jorge, 2018; Tavares &Jorge, 2012). Commercial meshless analysis programs have been used in structural engineering applications, but was not applied for biomechanics analysis (Choi, Kulinsky, Jun, &Kim, 2014; Erdine &Kallegias, 2017).

Rationale

Finite element (FE) models are often used for biomechanical computer simulation, to allow for parametric and repeatable analysis. When the method is applied to a complex structure such as the craniofacial structure, defeaturing, meshing, and solving the model require considerable computing resources. Our craniofacial computational model uses a structural analysis method that utilises the theory of external approximations (meshless method). This method allows complex models to be directly imported for simulation, potentially reducing time and computational resources.

Methods

The pilot specimen, a fresh frozen human cadaveric head (76 F), was CT scanned (isotropic voxel: 0.625 mm). The Temporal Mandibular Force Simulator was fitted to the specimen. Ten uniaxial strain gauges were cemented to craniofacial bones at locations of clinical interest (Figure A. 1). In-vitro strain measurements were obtained under 5%, 10%, and 15% of maximum physiological muscle loads. A 6 degrees of freedom load cell placed intra-orally measured in-vitro bite force.
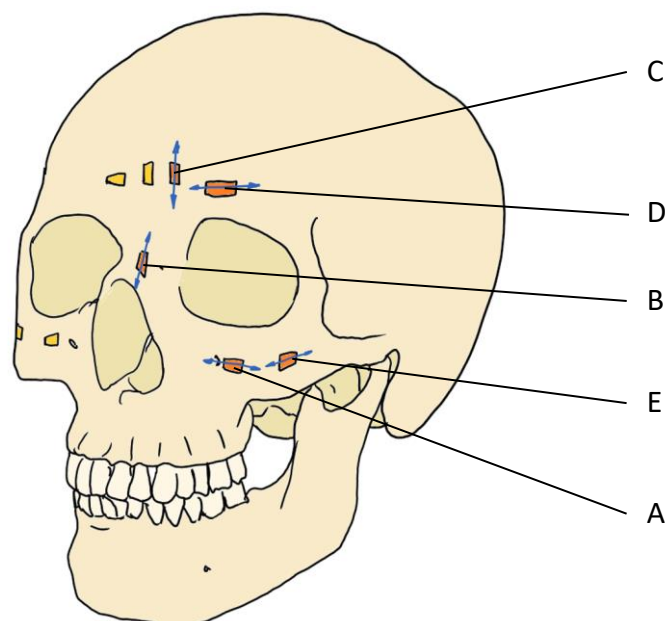
Figure A. 1. Locations of the uniaxial strain gauges on the pilot specimen. Blue arrows show directions of strain measured.

After experimental testing, the head was scanned using micro-CT (isotropic voxel: 0.108 mm). The micro-CT scan was combined with the clinical-resolution CT scan to create a stereolithography (STL) model of the skull with micro-resolution in the face and clinical resolution in the cranium and mandible (Figure A. 2). The strain gauges were located on the solid model using micro-CT data. The complete experiment, including bone and piston mounts, was directly imported into a commercial structural analysis software (Simsolid, Simsolid Corporation; Newport Beach, California USA) as STL models. The program automatically generated a meshless model from the STL, thin bone and trabecular structures were preserved. Material properties of the bones were set to 12 GPa with $\nu = 0.3$. "Sliding connections" were applied at the temporomandibular joints, which allowed a hinge-like motion at the joints. The piston mount models were connected to the skull model at muscle attachment sites with "bonded connections". The same loads as in the in-vitro experiment were applied to the piston mounts. Reversed engineered patches were created at muscle attachment areas. The coupled force of the corresponding piston mount, equal in magnitude but opposite in direction, was applied to the patch. In the case of the temporalis, the vector sum of the anterior and posterior temporalis piston output

was applied to the patch at the mandibular coronoid. A patch would spread the load across the entire attachment area as in the in-vitro experiment. The model of the specimen fixation mount was connected to the back of the skull, a fixed boundary condition was applied to this mount to hold the specimen in place. The virtual load cell was placed intraorally to measure simulated occlusal loads. Simulated strain measurements were obtained at corresponding gauge locations.
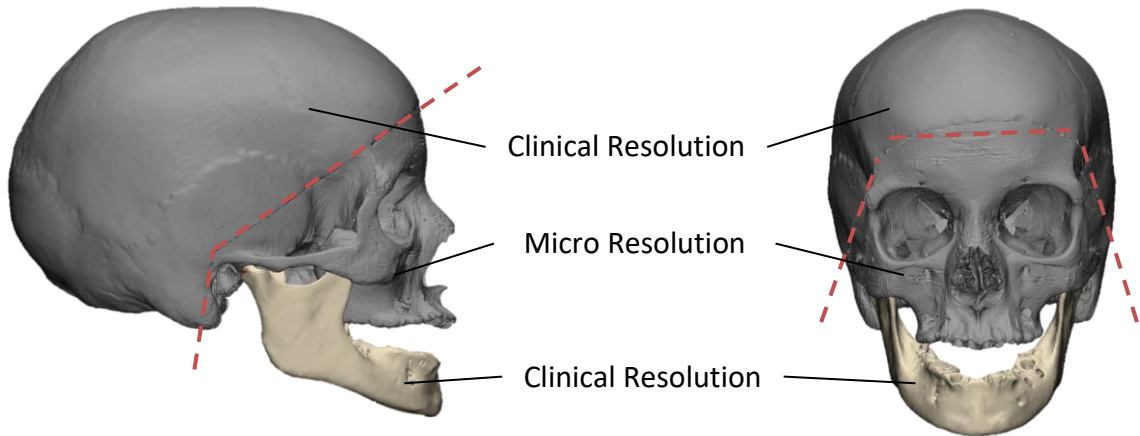
Figure A. 2. The model combined clinical-resolution CT model of the cranium and mandible, with micro-resolution CT model of the face.
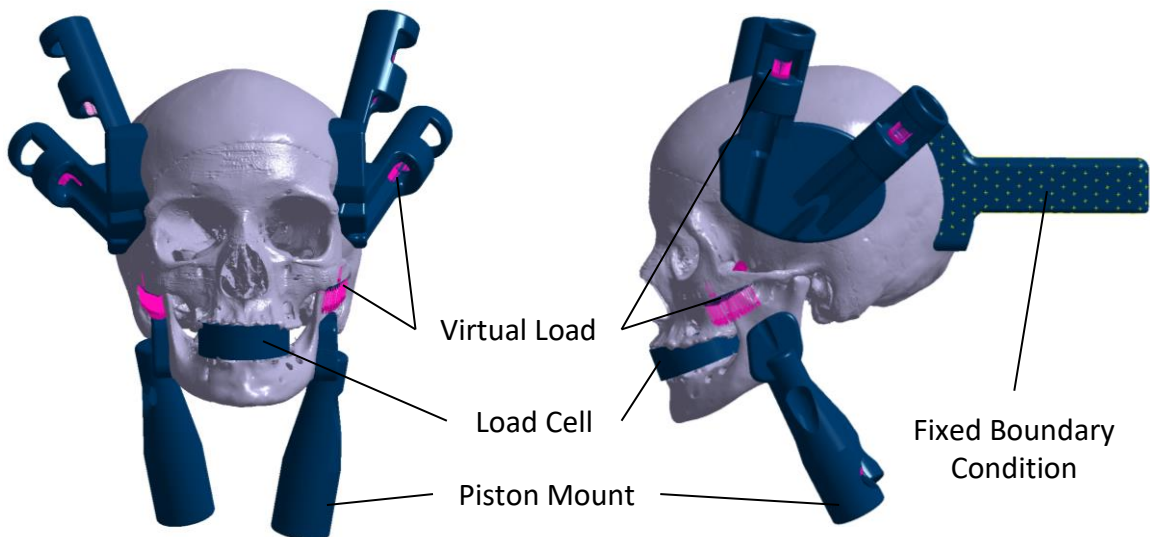
Figure A. 3. The computer model of the experimental setup. Virtual loads are shown in pink. A fixed boundary condition was applied to the specimen fixation mount.

A sensitivity analysis was performed to investigate the effect of shifting the load of the masseter muscle within the physiological range. The patch for the masseter's origin on the zygomatic arch was shortened to shift the load centroid posteriorly (Figure A. 4). The strains around location E will be reviewed.

a) Baseline (29.54 mm) b) Posterior 1 (21.89 mm) c) Posterior 2 (16.65 mm)
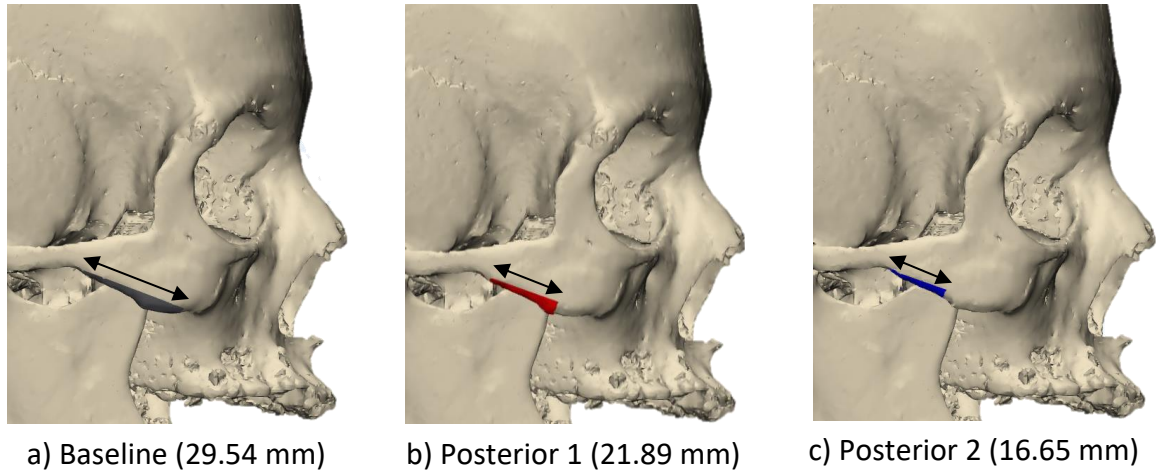
Figure A. 4. Three different configurations of masseter attachment origin patch. a) shows the baseline configuration. a) Posterior 1 and b) 2 configurations were progressively shortened from the baseline configuration at the anterior end. Arrows and dimensions in brackets show lengths of the patch at the three configurations.

Results

Strain measurements under internal load at 5%, 10%, and 15% of physiological maximum were obtained from the in-vitro experiment. Strain measurements from the meshless model are resented alongside the in-vitro results (Figure A. 6). The same symmetry at location A was present in both in-vitro and meshless model, with tension on the right side and compression on the left side.

Computer simulations at each load level took on average 15 minutes to complete. Result showed asymmetry in strain field (Figure A. 5). Strain measurements from the computer simulation at 15% load were plotted against that from the experiment (Figure A. 7). Strain measurements at the 10 strain gauges were probed, and the measurements were transformed so that they aligned with the axis of the uniaxial strain gauges. When all 10

strain gauges were considered, there was a positive correlation between strain measurements from the meshless model and the experiment, $r = 0.649$, $n = 10$, $p = .042$ (Pearson product moment). Regression analysis calculated a slope of $.3758 \pm .1558$. When only the 8 strain gauges away from load application (i.e. location A-D), the correlation increased, $r = 0.886$, $n = 8$, $p = .003$ (Pearson product moment). Regression analysis calculated a slope of $.4589 \pm .0979$ with the 8 gauges.
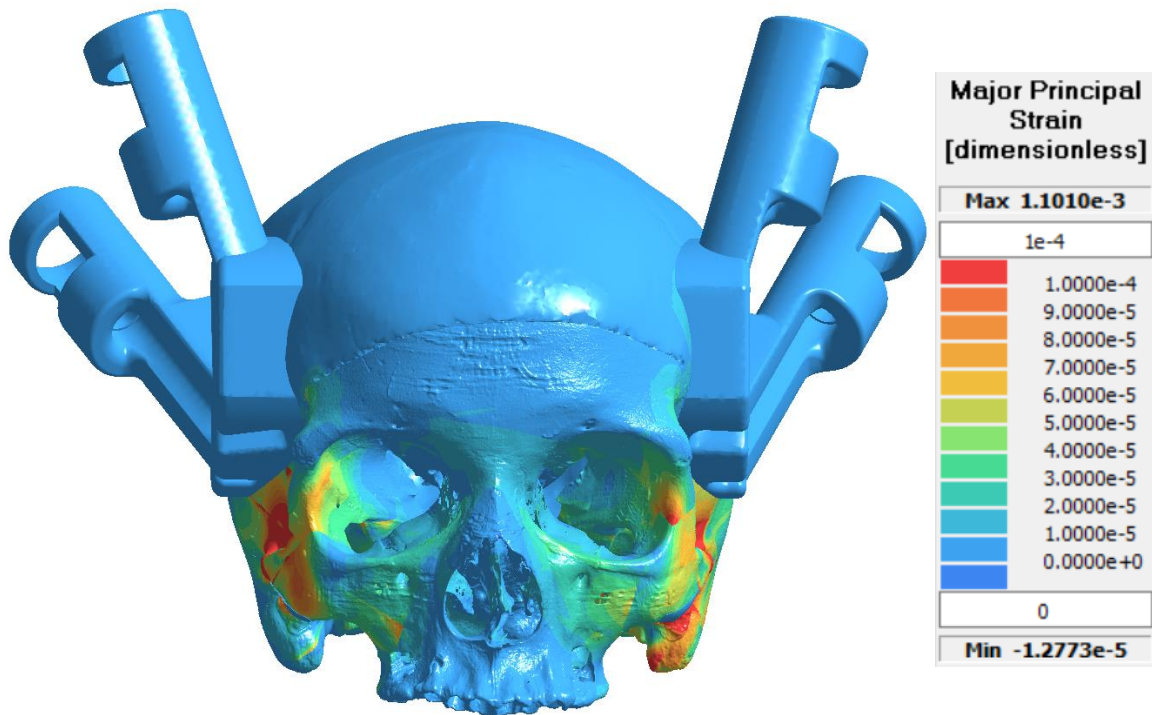
Figure A. 5. Major principal strain in the meshless model under 15% load. Asymmetry in strain pattern is observed around the orbit. Only the skull and the temporalis mounts are shown.
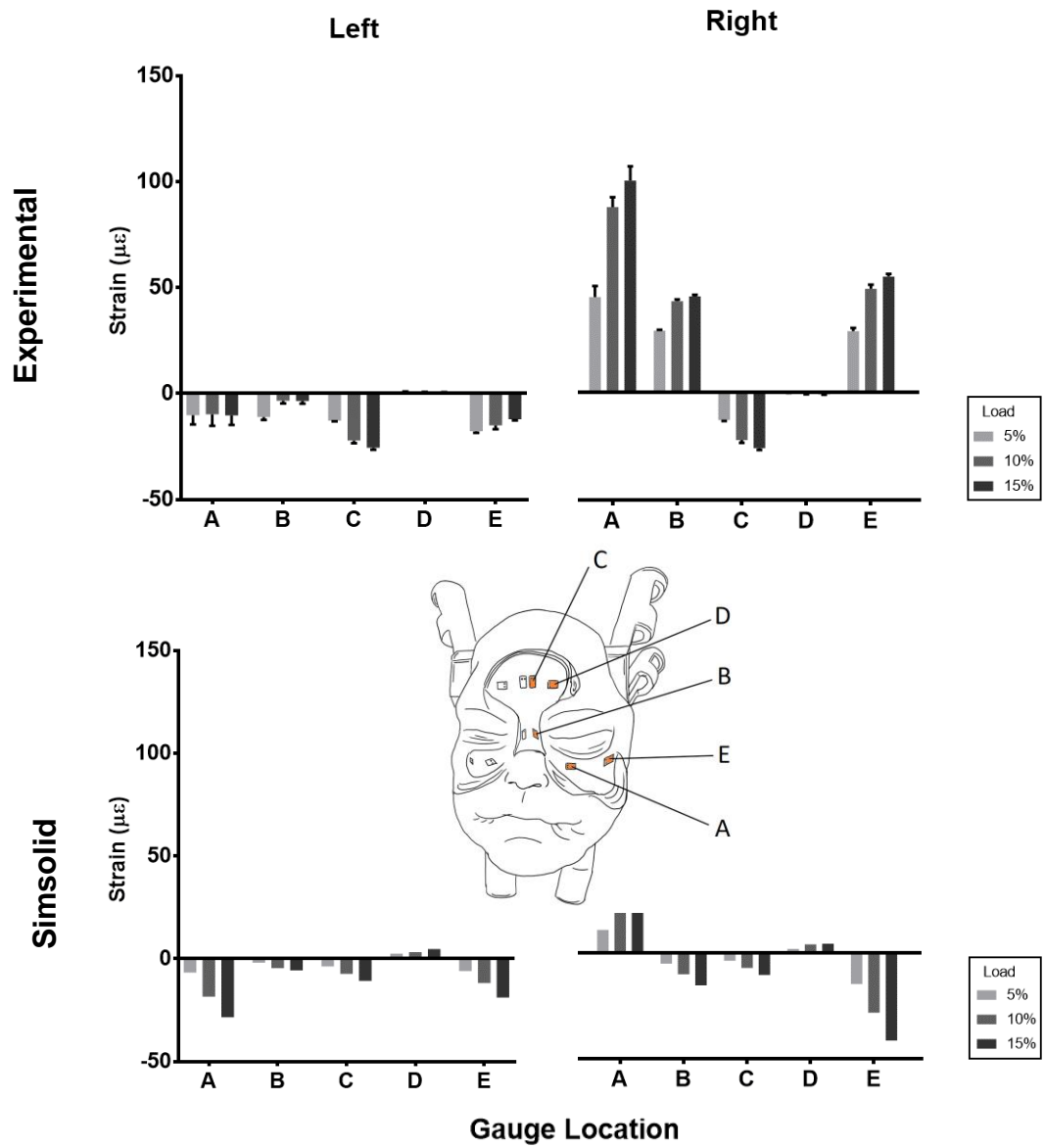
Figure A. 6. (Top) Strain measurements from the experiment. (Bottom) Strain measurements from the computer simulation.
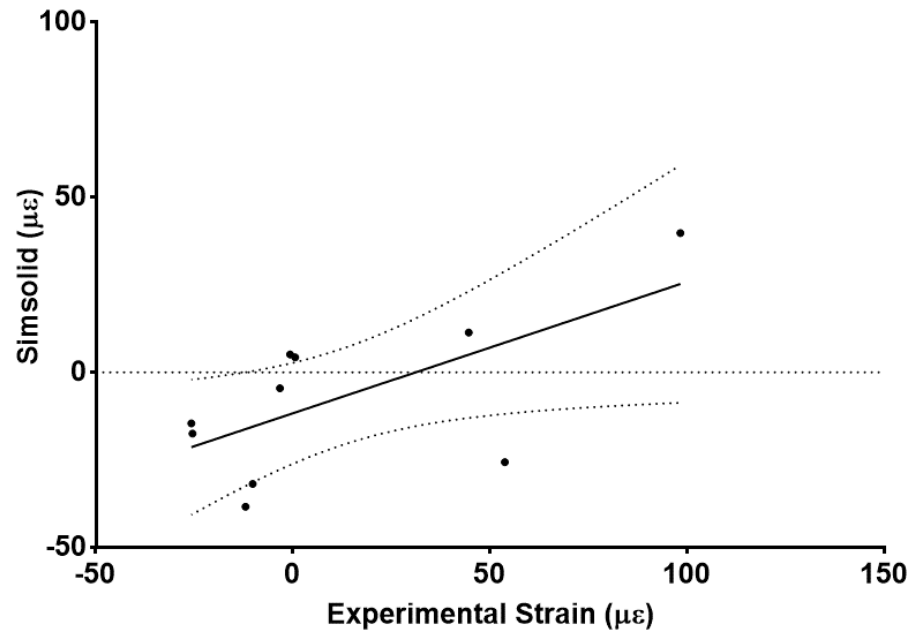
Figure A. 7. Scatter plot showing the correlation between strain measurements from the in-vitro experiment and the strain measurements from the meshless computer model (Simsolid). Regression line shows 95% CI.

Table A. 1. Pearson product-moment correlation coefficients of strain measurements from the meshless model against the experiment

Item	Pearson Coefficient (r)	p Value (p)	Sample Size (n)
Locations A-E	.649	.042	10
Locations A-D	.810	.003	8

Sensitivity analysis showed the line of inflection, where tensile strain transitioned to compressive strain, shifted posteriorly with load (Figure A. 8). The strain field shown was in line with the uniaxial strain gauge at location E. In the baseline configuration, the inflection line was on the strain gauge at location E (Figure A. 8a). In posterior 1 and 2 configurations where the patch was shortened from the anterior end (i.e. posterior shift of load centre), the inflection line progressively shifted in the posterior direction (Figure A. 8d).

a) Baseline   b) Posterior 1   c) Posterior 2

d) Overlay
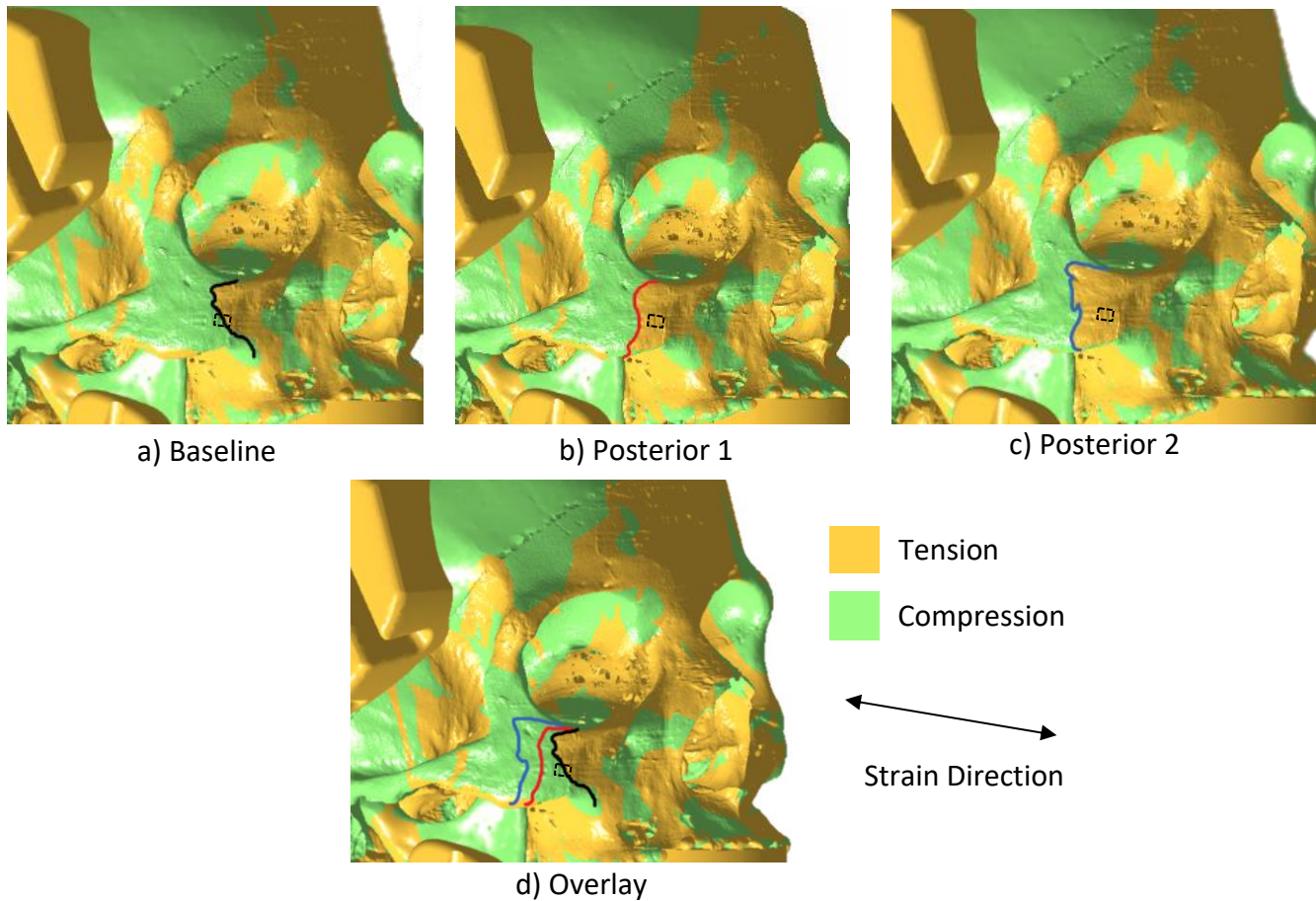
Figure A. 8. Strain field in the direction of the strain gauge at location E (dotted box) on the right side. Orange shows tensile strain and green shows compressive strain. The line of inflection around location E are shown for a) baseline in black, b) posterior 1 in red, and c) posterior 2 in blue. d) is the overlay of the three inflection lines.

Discussion

There were initial concerns over the possibility of load imbalance causing the asymmetry in experimental strains. In the meshless model, the boundary conditions could be tightly controlled. The consistent piston force outputs in the meshless model ensured there was no load imbalance across the two sides of the specimen. Strain measurements from the meshless model again showed asymmetry, specifically at location A on the maxilla

(Figure A. 6). The asymmetry in the meshless model demonstrated that asymmetry in load measurement can result from factors other than load imbalance.

There was a moderate agreement between strain measurements from the experiment and the meshless model. However, when only the strains away from the load were considered (i.e. Location A-D), the agreement between the experiment and meshless model was much stronger. In the experiment, strain gauge at location E on the zygoma showed compression on the left side and tension on the right side. In the meshless model, although compressive strains were measured on both sides of the face, the magnitude of compressive strain was higher on the right side. The meshless model revealed a line of inflection close to location E, compressive strain in the direction of the gauge's axis was found on the posterior side of the line. The sensitivity analysis showed the inflection line move posteriorly with the load centroid of the masseter's origin posteriorly. This finding suggests that strain measurements from a uniaxial strain gauge in the area around a load can be sensitive to the load's placement.

Conclusion

There was a strong agreement between the strain pattern obtained from the computer simulation and in-vitro measurements. The meshless model demonstrated asymmetry in strain measurements could arise from factors other than load imbalance.

Appendix B: Baseline Measurements under Internal Load
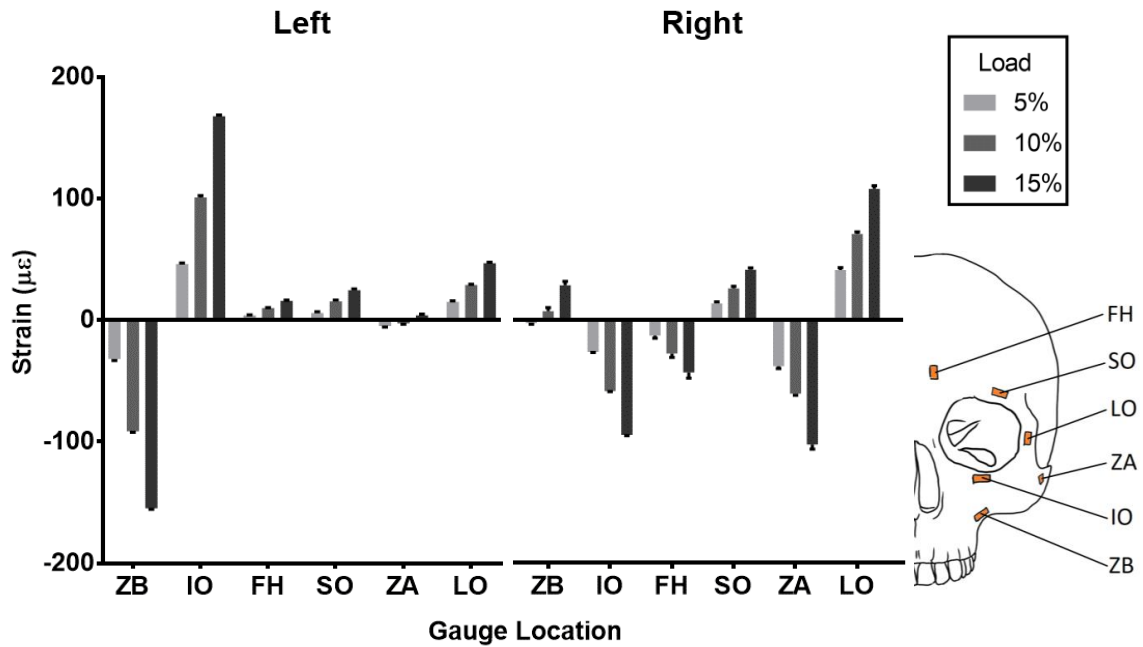
**Figure B. 1. Baseline measurements from Specimen 1 under internal load. Error bars shows standard errors across the five trials.**
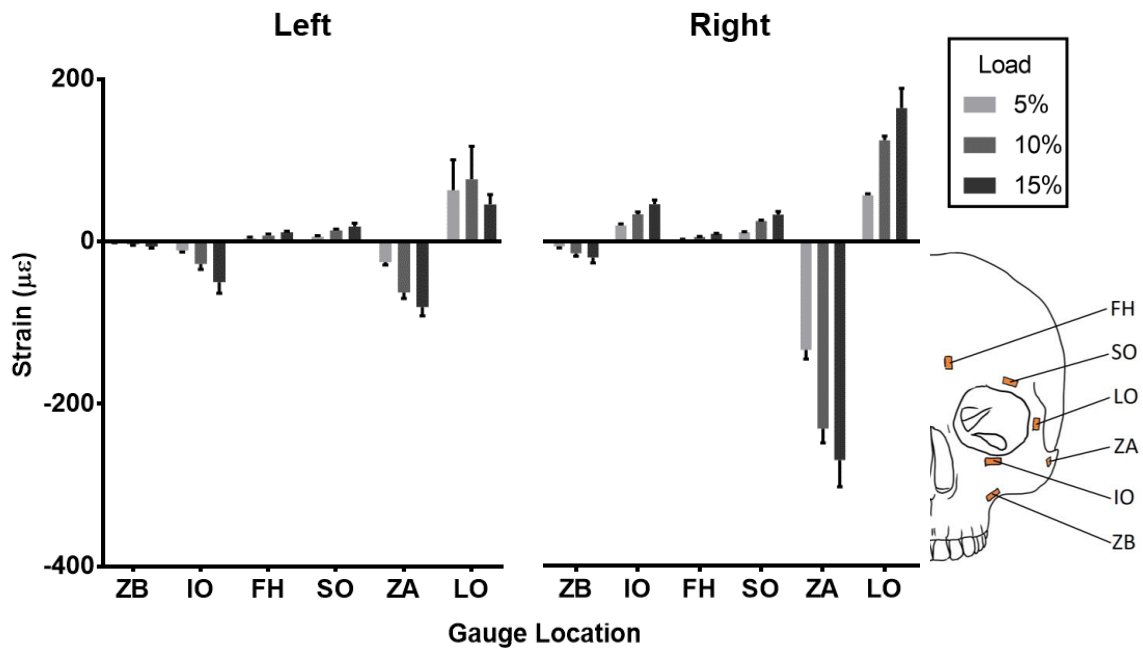
Figure B. 2. Baseline measurements from Specimen 2 under internal load. Error bars shows standard errors across the five trials.
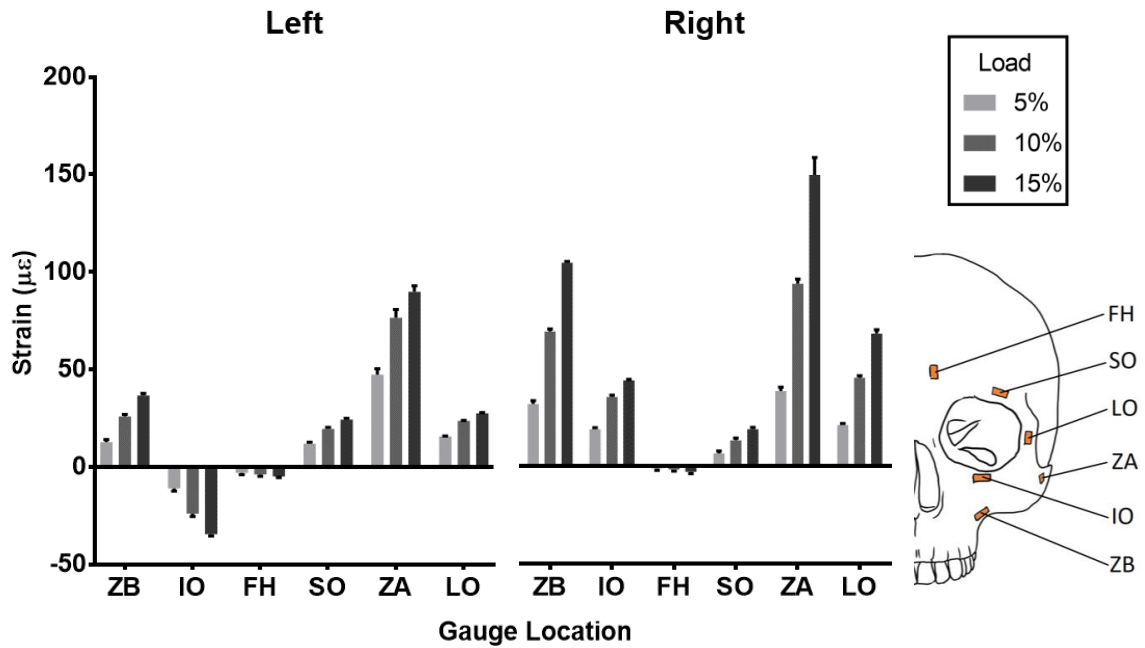
Figure B. 3. Baseline measurements from Specimen 3 under internal load. Error bars shows standard errors across the five trials.
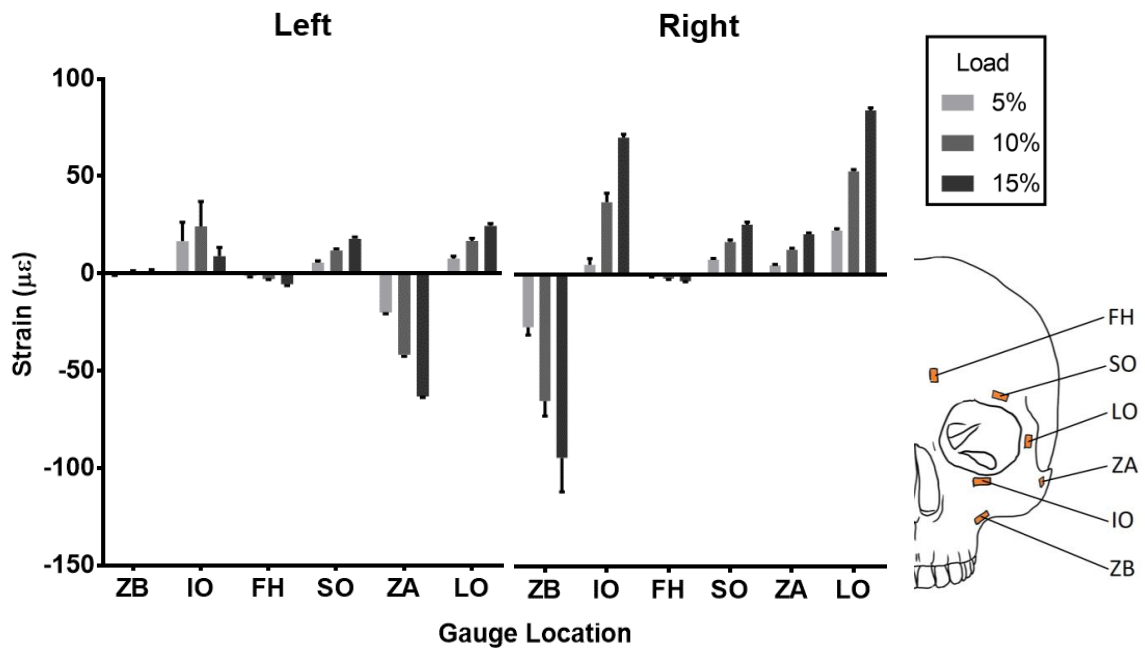
Figure B. 4. Baseline measurements from Specimen 4 under internal load. Error bars shows standard errors across the five trials.
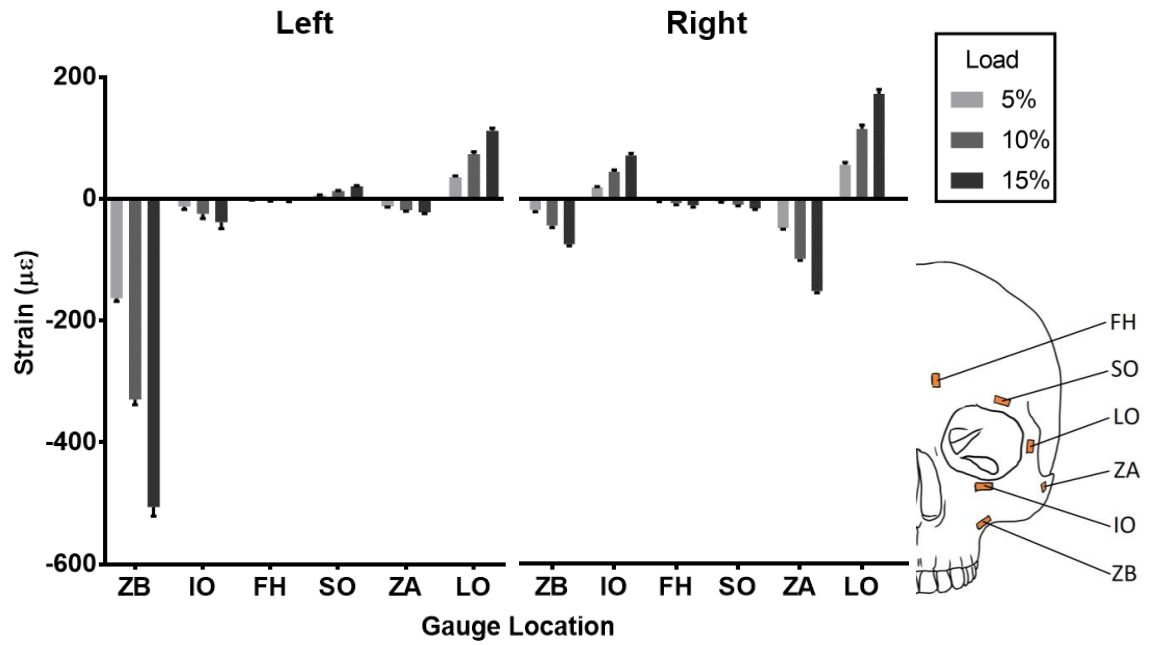
Figure B. 5. Baseline measurements from Specimen 5 under internal load. Error bars shows standard errors across the five trials.

Appendix C: Baseline Measurements under External Load
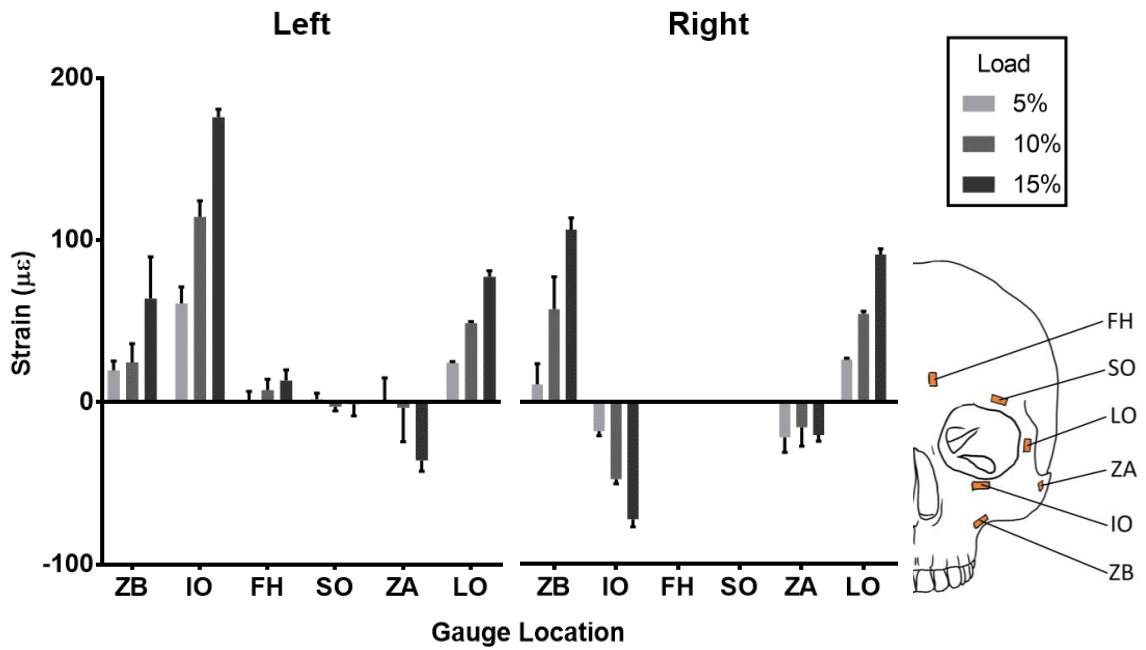
Figure C. 1. Baseline measurements from Specimen 1 under external load. Error bars shows standard errors across the five trials. Bad gauge at FH and SO (right).
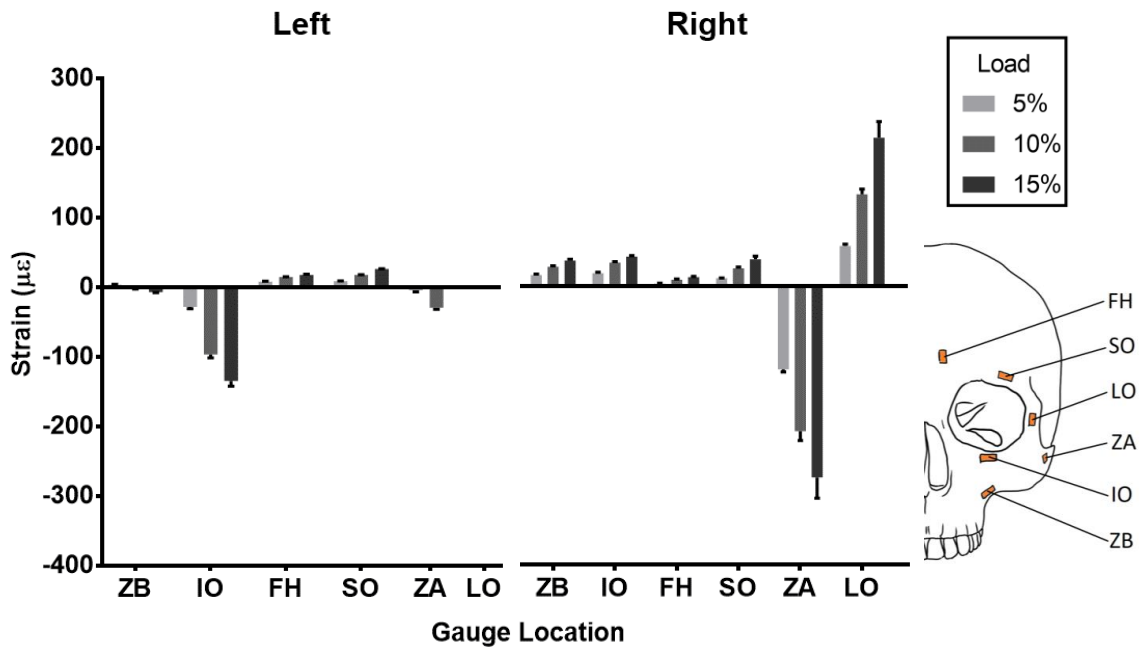
Figure C. 2. Baseline measurements from Specimen 2 under external load. Error bars shows standard errors across the five trials. Bad gauge at LO (left).
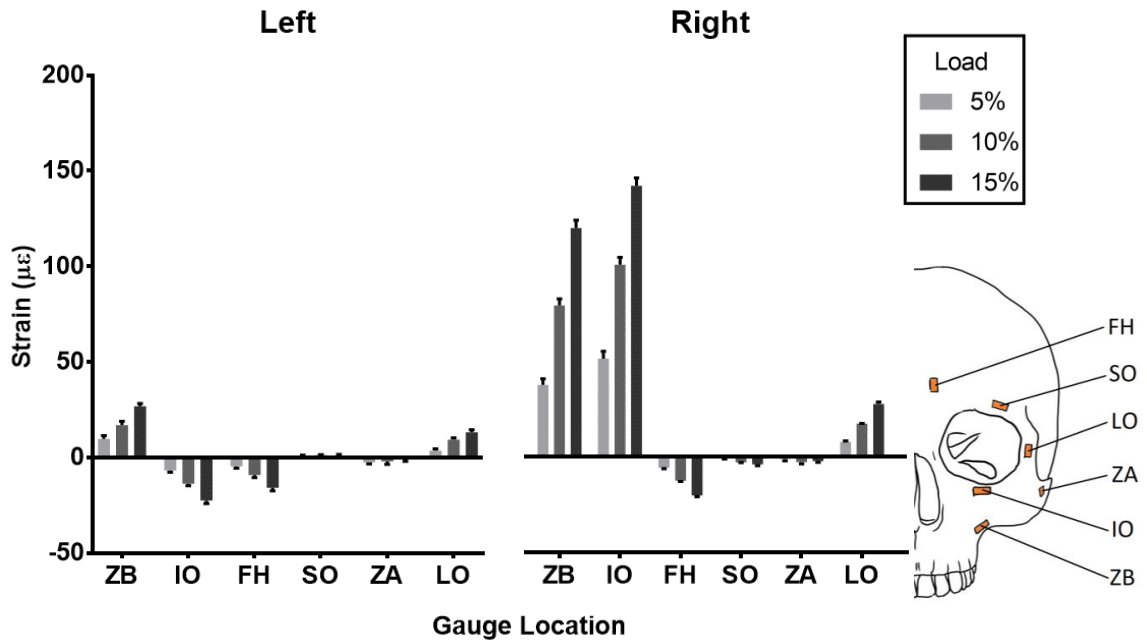
Figure C. 3. Baseline measurements from Specimen 3 under external load. Error bars shows standard errors across the five trials.
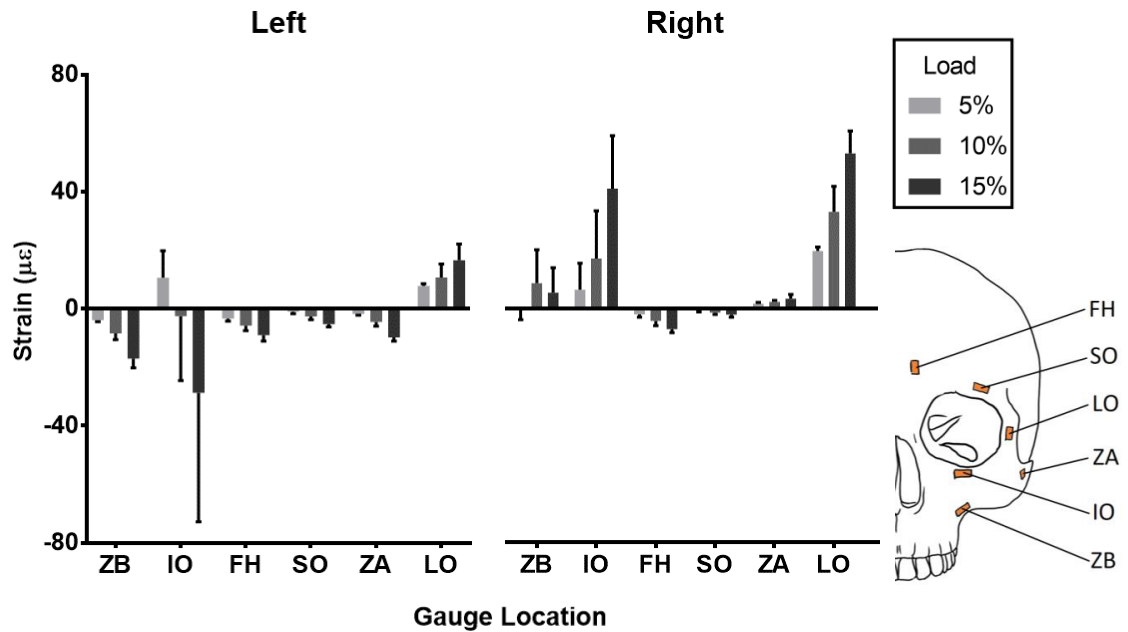
Figure C. 4. Baseline measurements from Specimen 4 under external load. Error bars shows standard errors across the five trials.
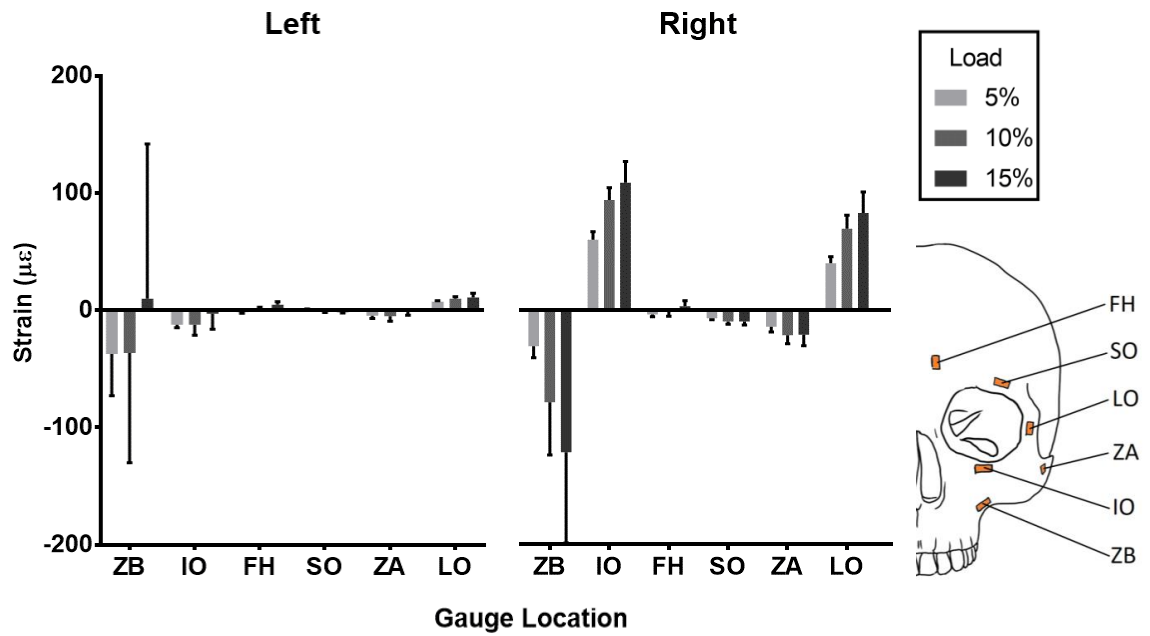
Figure C. 5. Baseline measurements from Specimen 5 under external load. Error bars shows standard errors across the five trials.

Appendix D: Strain Measurements in Fracture Repairs under Internal Load
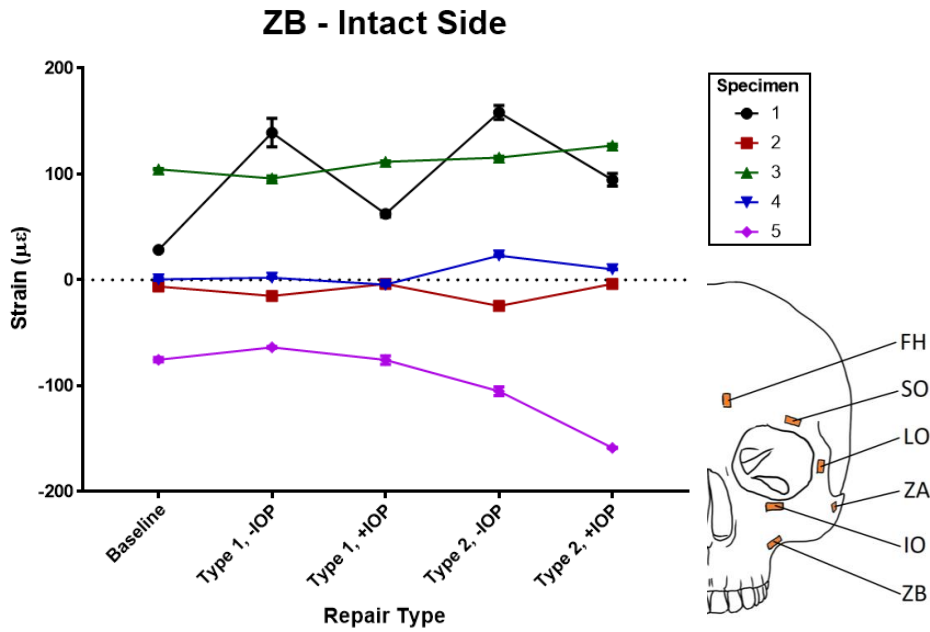
Figure D. 1. Strain measurements at location ZB on the intact side by specimen and fracture repair type under internal load.
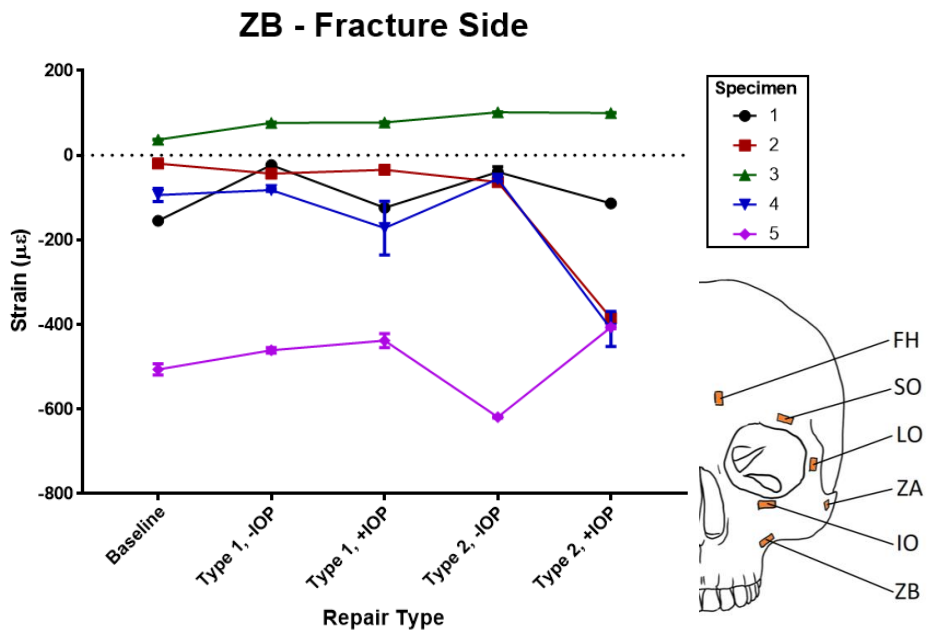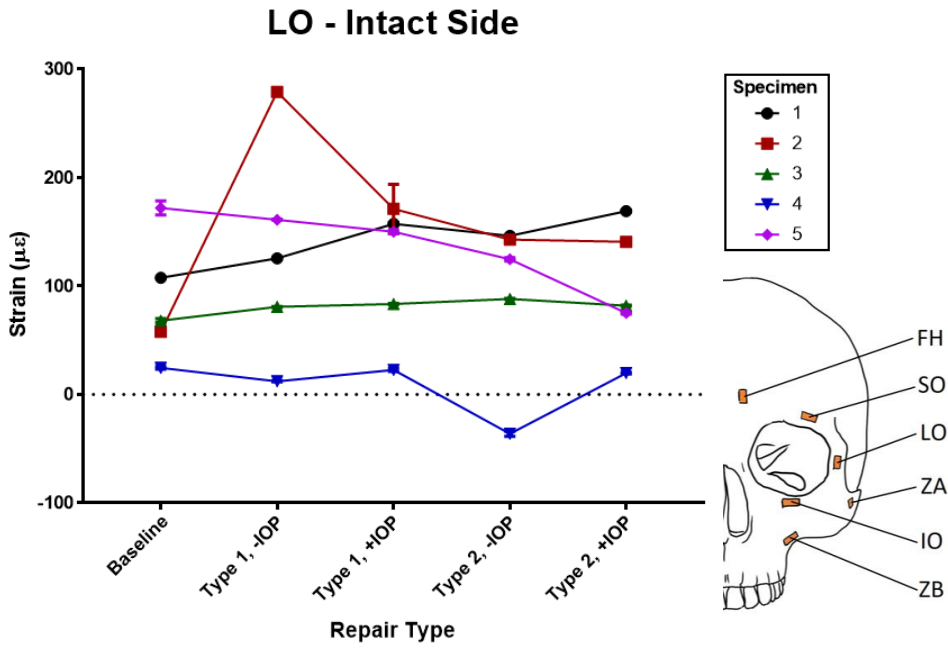

Figure D. 2. Strain measurements at location ZB on the fracture side by specimen and fracture repair type under internal load.
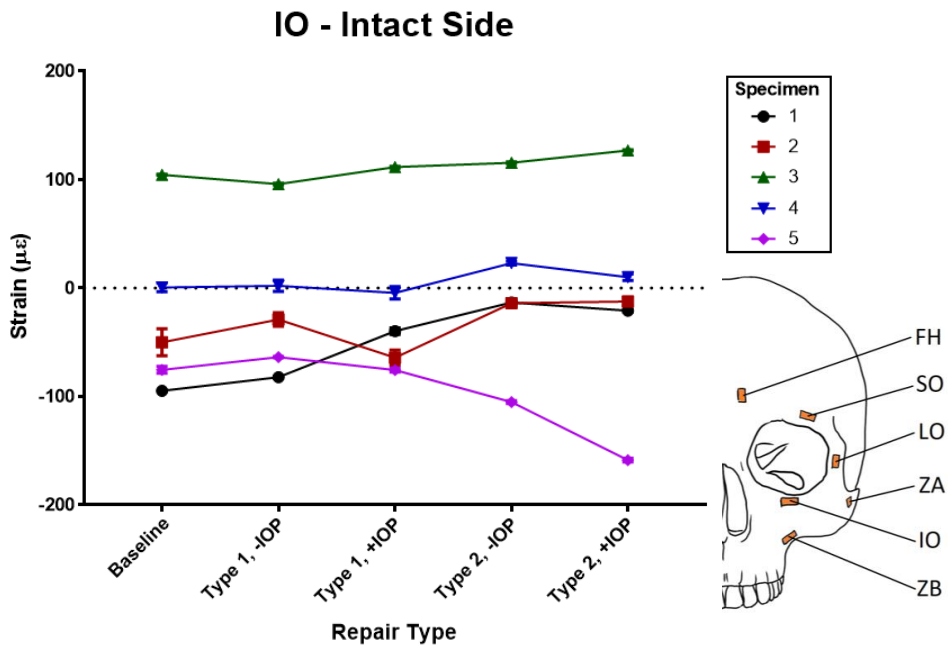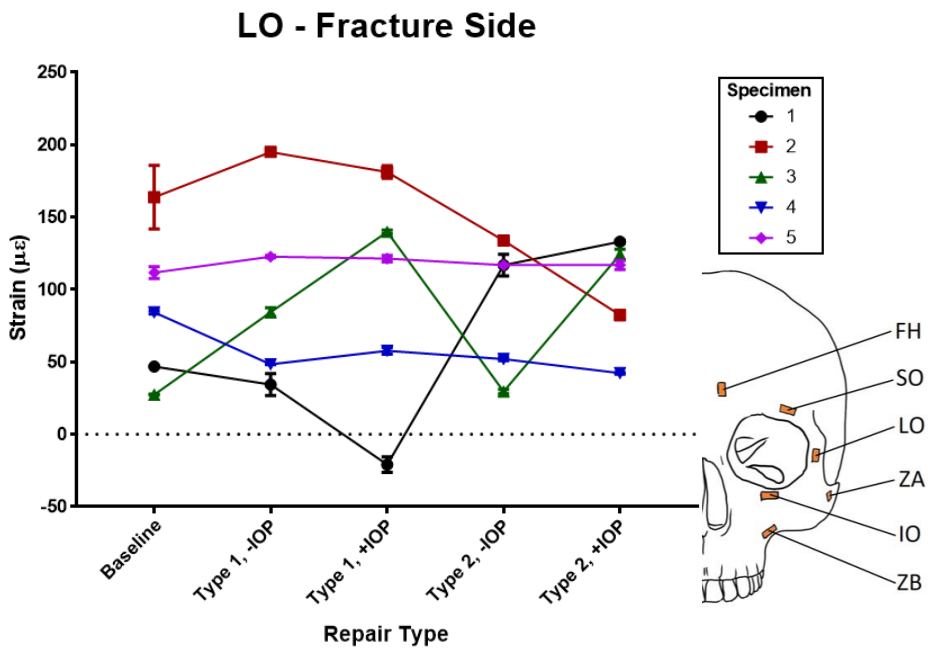
Figure D. 3. Strain measurements at location IO on the intact side by specimen and fracture repair type under internal load.
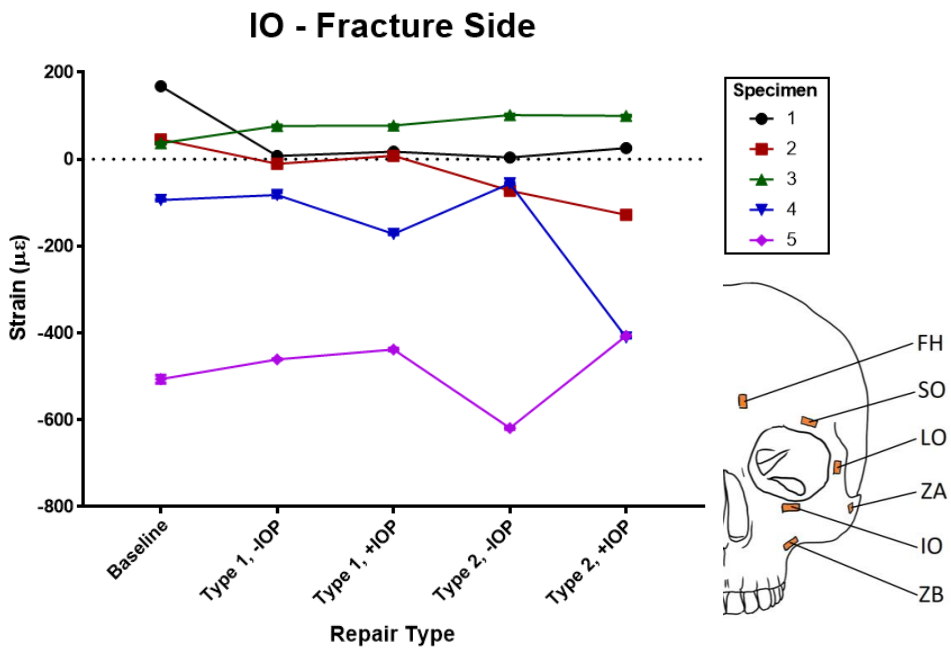
Figure D. 4. Strain measurements at location IO on the fracture side by specimen and fracture repair type under internal load.
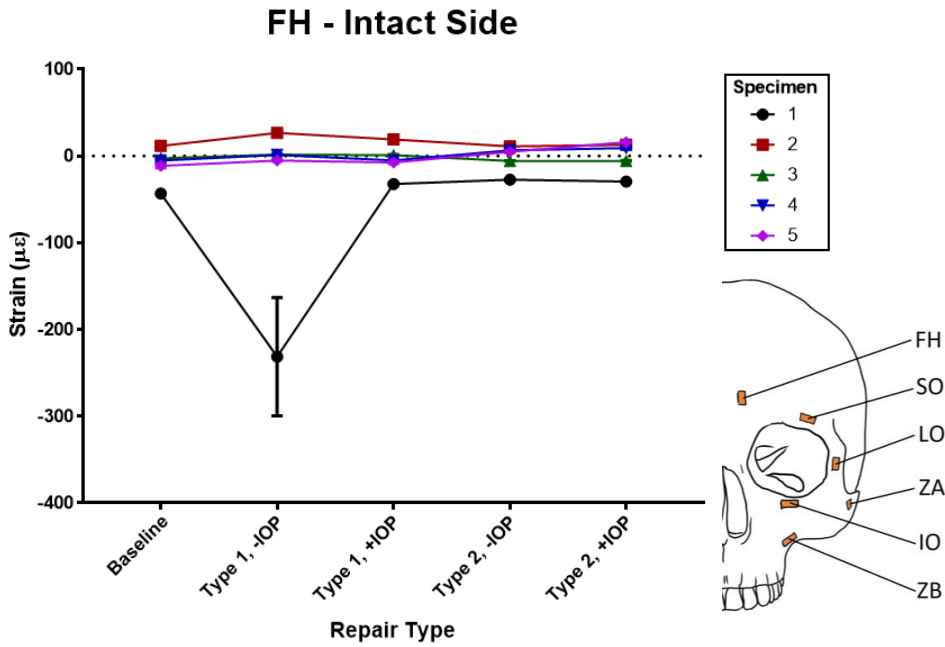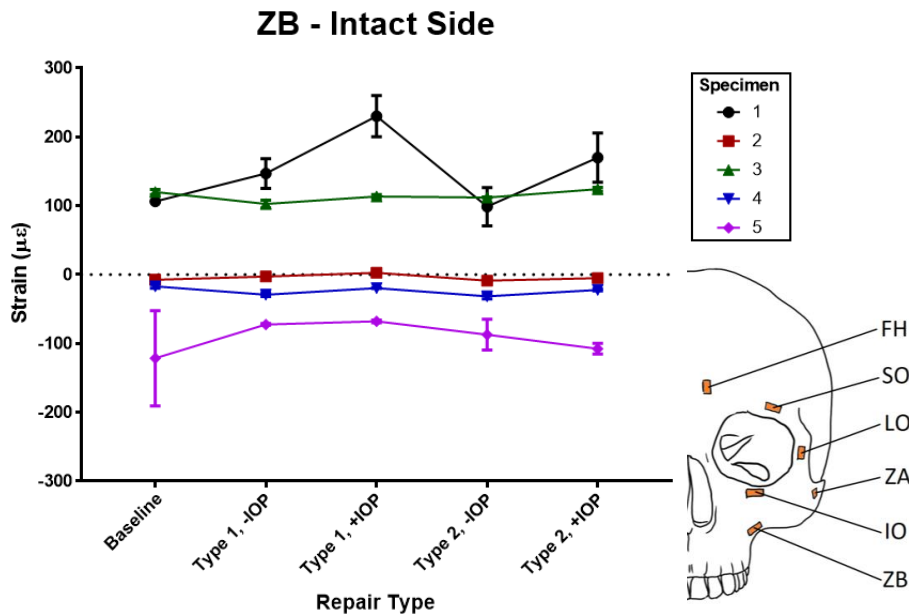
Figure D. 5. Strain measurements at location FH on the intact side by specimen and fracture repair type under internal load.
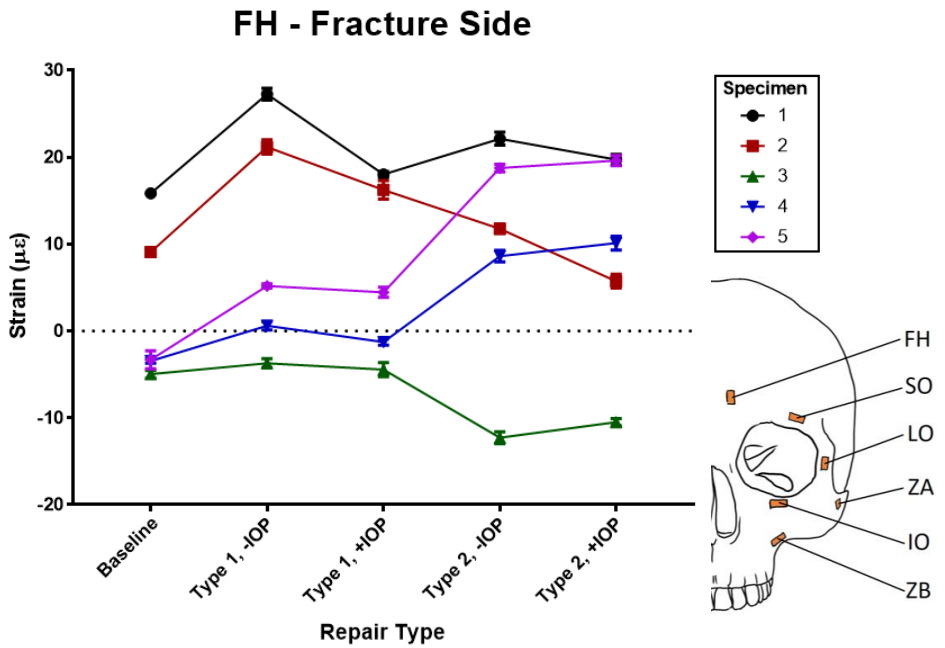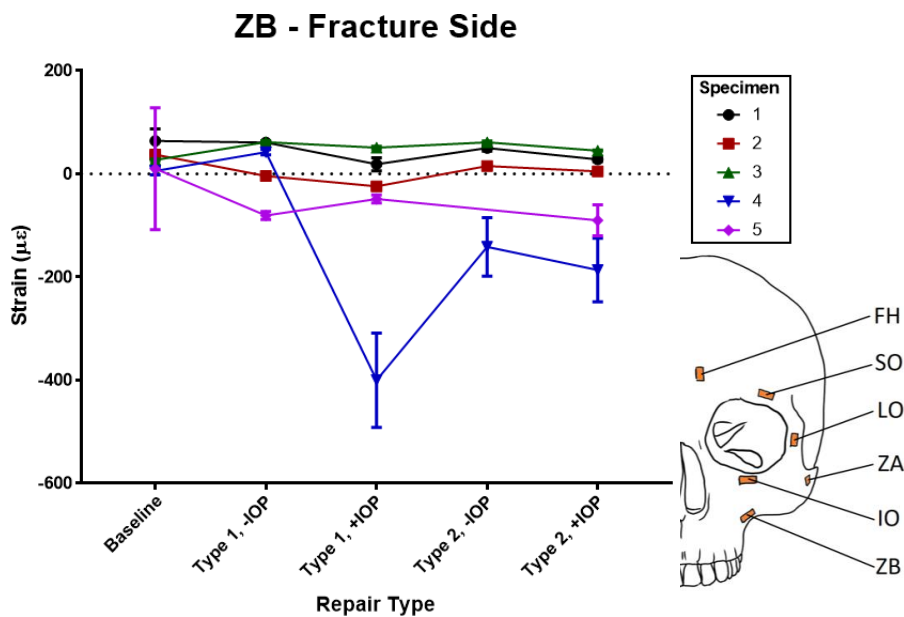

Figure D. 6. Strain measurements at location FH on the fracture side by specimen and fracture repair type under internal load.
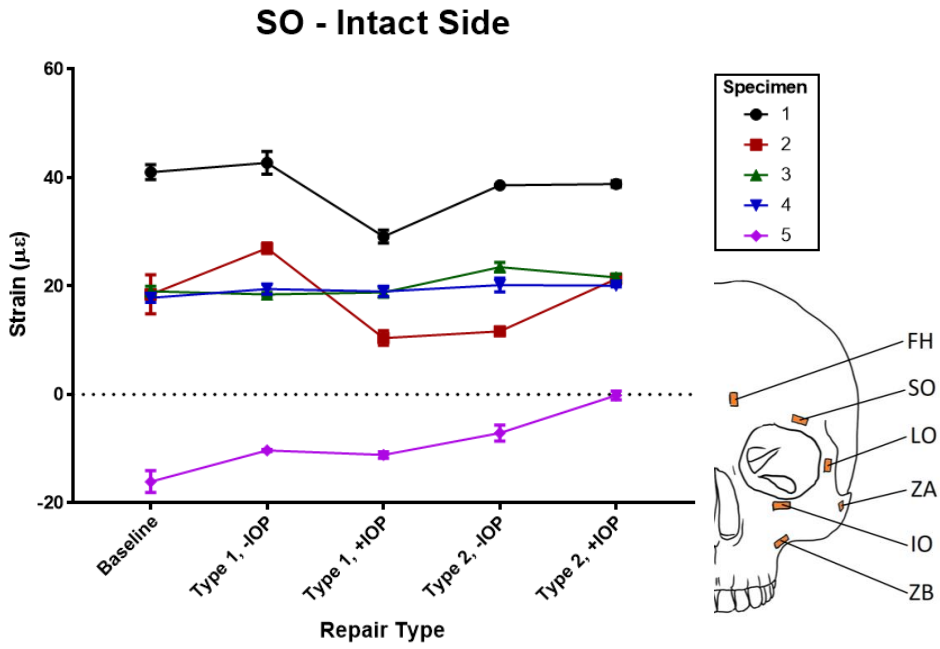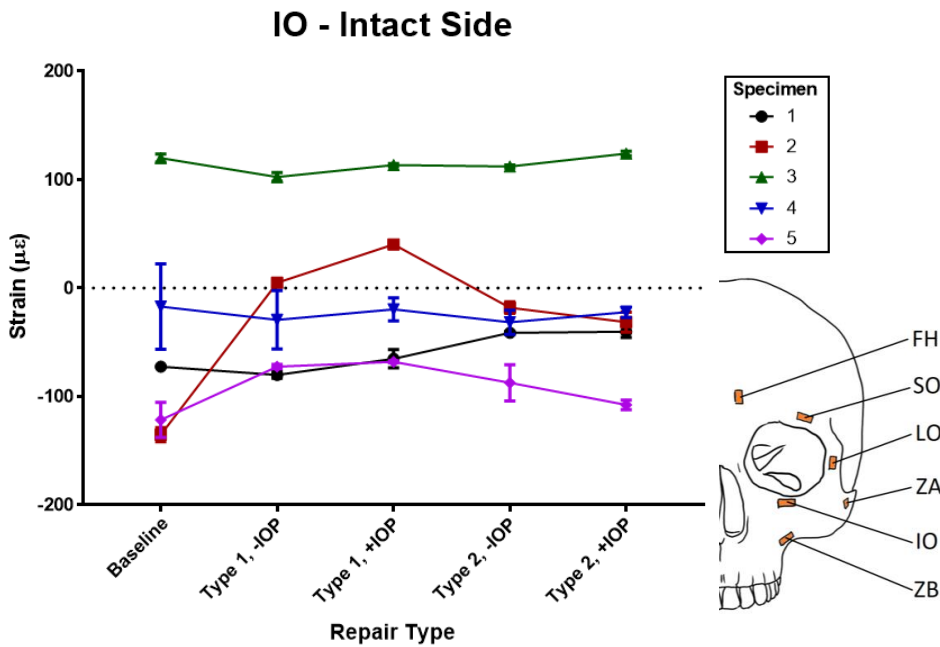
Figure D. 7. Strain measurements at location SO on the intact side by specimen and fracture repair type under internal load.
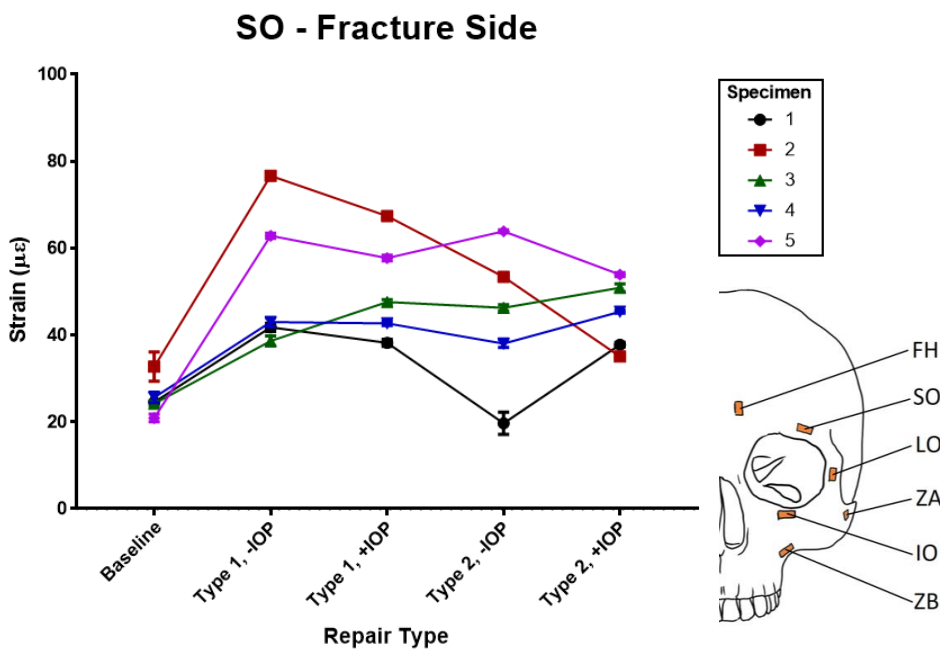
Figure D. 8. Strain measurements at location SO on the fracture side by specimen and fracture repair type under internal load.
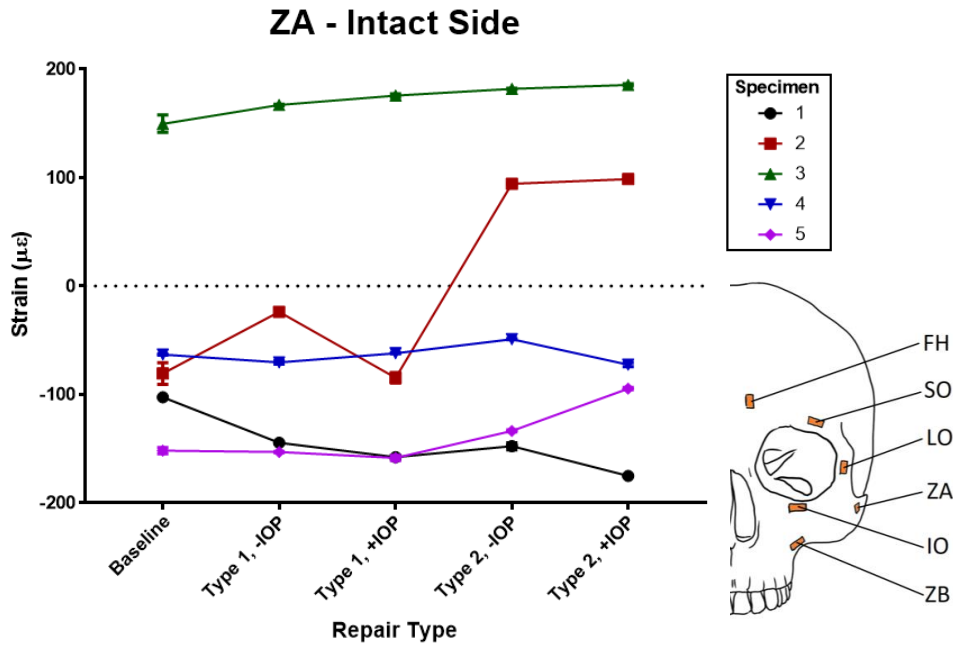
Figure D. 9. Strain measurements at location ZA on the intact side by specimen and fracture repair type under internal load.
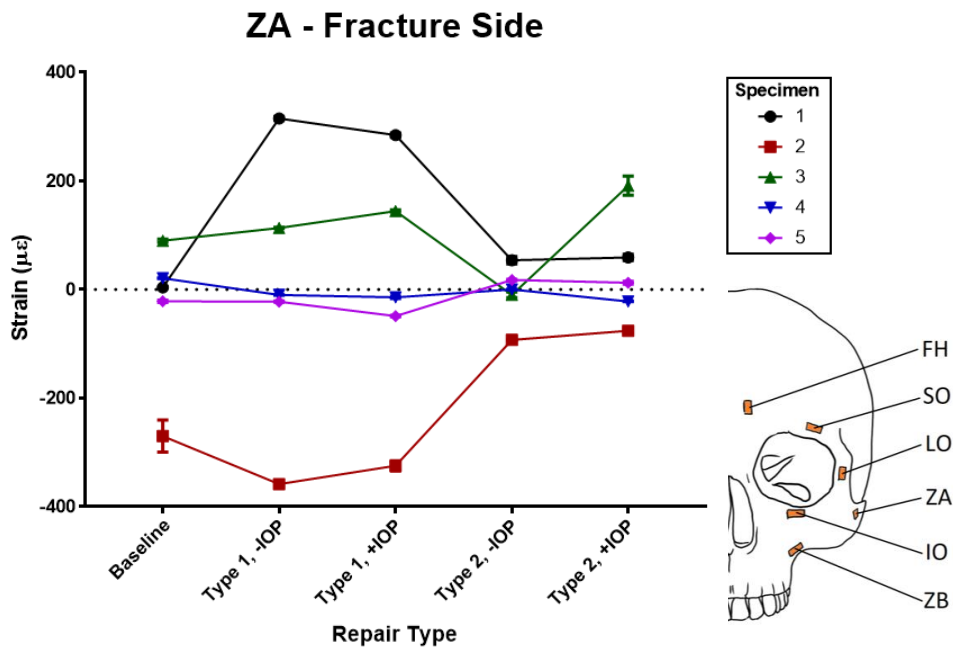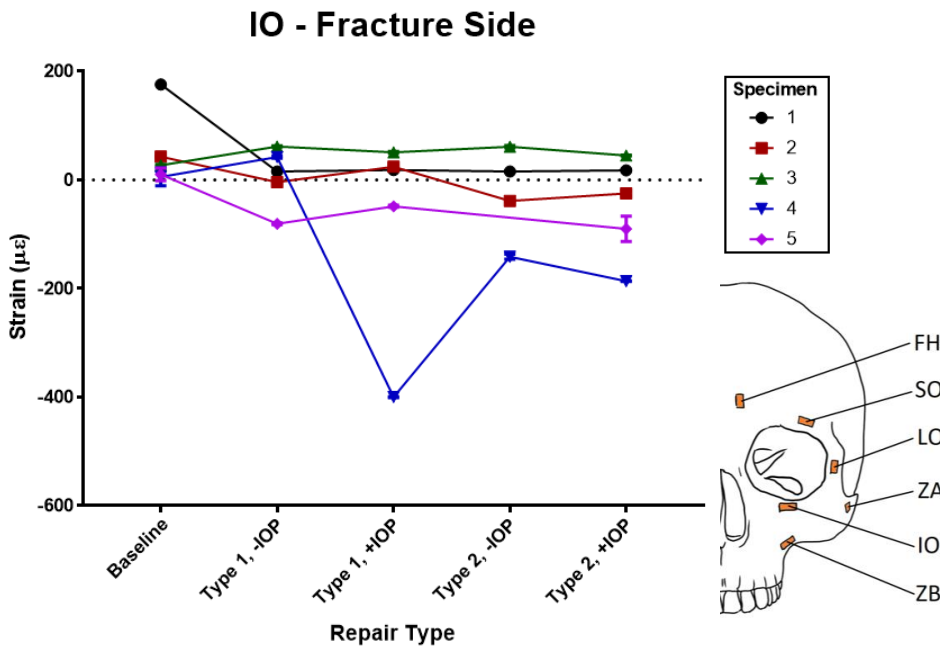

Figure D. 10. Strain measurements at location ZA on the fracture side by specimen and fracture repair type under internal load.

Figure D. 11. Strain measurements at location LO on the intact side by specimen and fracture repair type under internal load.

Figure D. 12. Strain measurements at location LO on the fracture side by specimen and fracture repair type under internal load.

Appendix E: Strain Measurements in Fracture Repairs under External Load

Figure E. 1. Strain measurements at location ZB on the intact side by specimen and fracture repair type under external load.

Figure E. 2. Strain measurements at location ZB on the fracture side by specimen and fracture repair type under external load. Measurements from type 2, -IOP of specimen 5 omitted because of bad gauge.
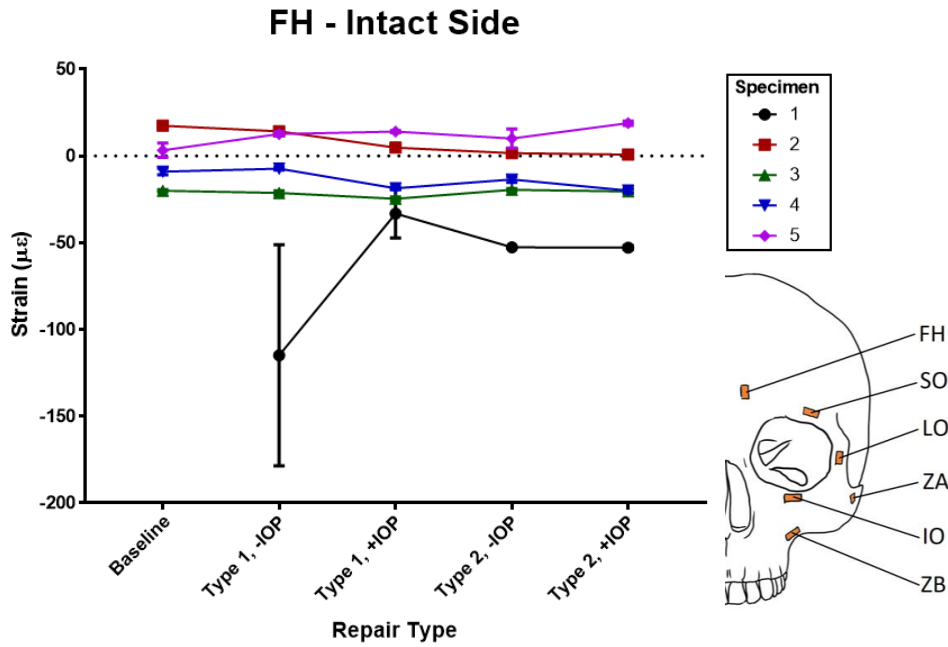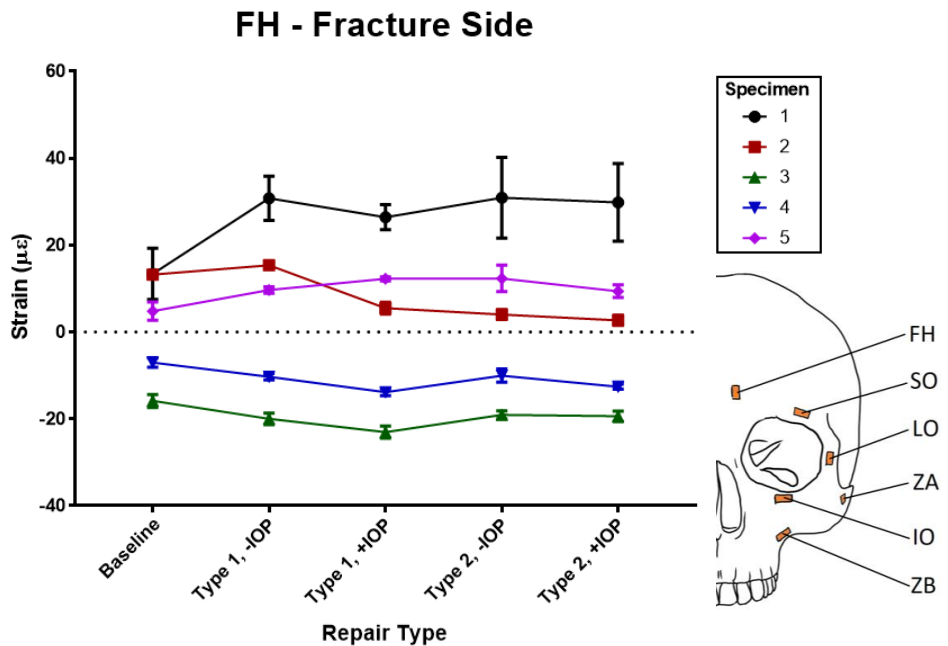
Figure E. 3. Strain measurements at location IO on the intact side by specimen and fracture repair type under external load.
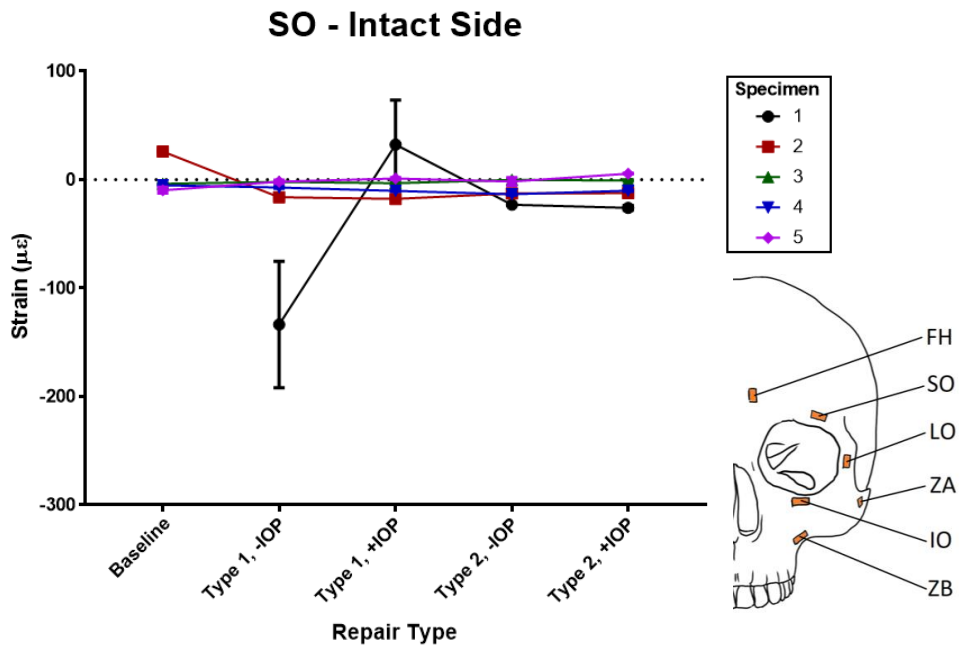

Figure E. 4. Strain measurements at location IO on the fracture side by specimen and fracture repair type under external load. Measurements from baseline of specimen 1 omitted because of bad gauge.
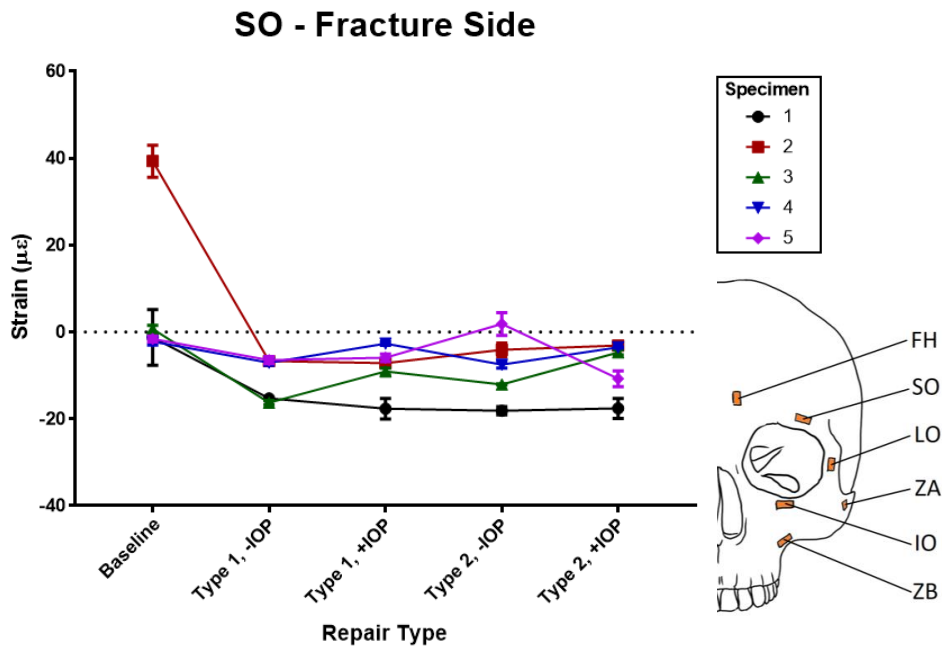
Figure E. 5. Strain measurements at location FH on the intact side by specimen and fracture repair type under external load. Measurements from baseline of specimen 1 omitted because of bad gauge.
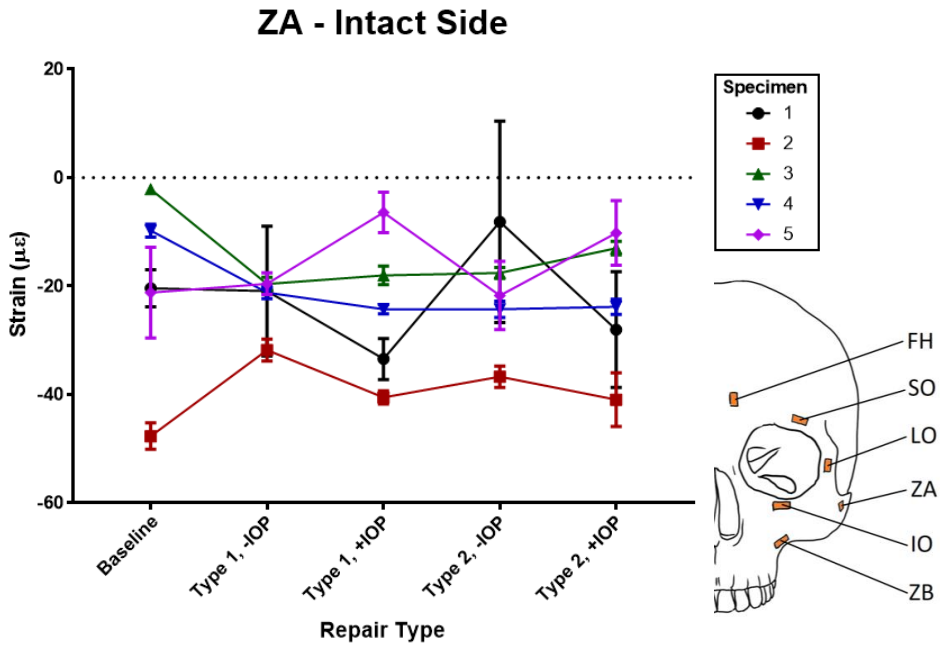

Figure E. 6. Strain measurements at location FH on the fracture side by specimen and fracture repair type under external load.
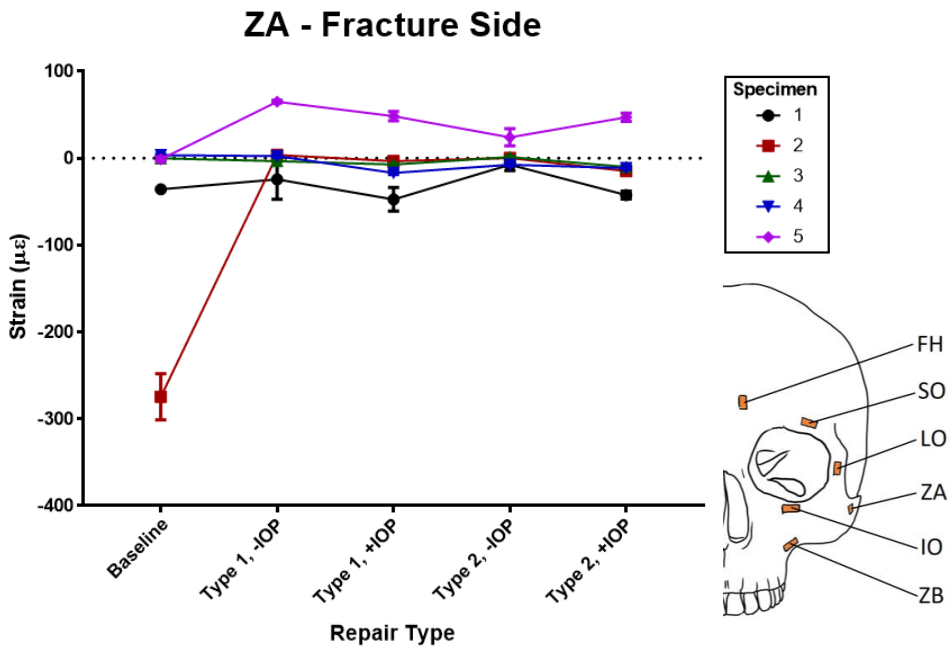
Figure E. 7. Strain measurements at location SO on the intact side by specimen and fracture repair type under external load. Measurements from baseline of specimen 1 omitted because of bad gauge.
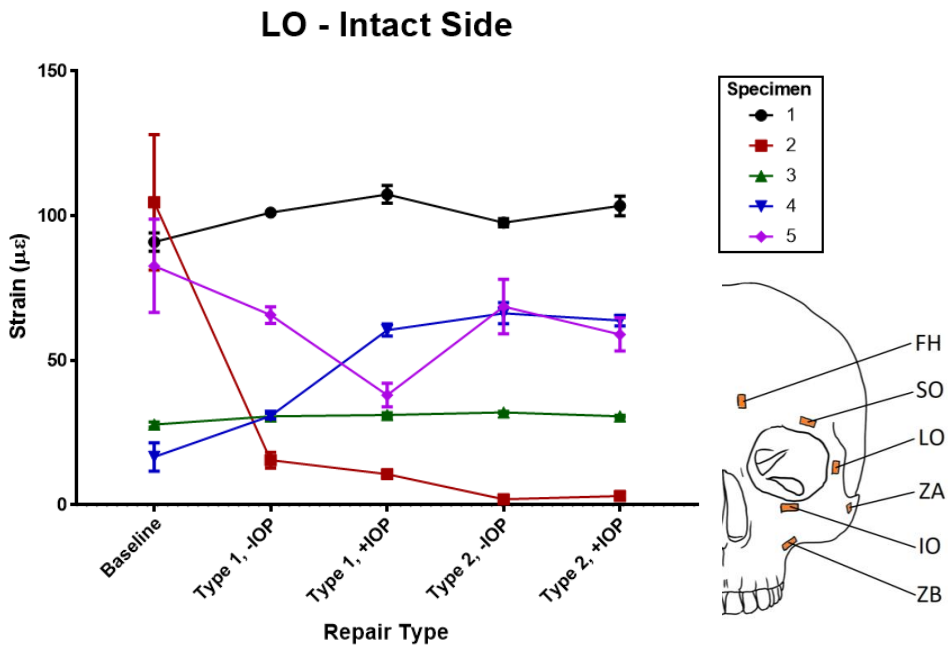

Figure E. 8. Strain measurements at location SO on the fracture side by specimen and fracture repair type under external load.

Figure E. 9. Strain measurements at location ZA on the intact side by specimen and fracture repair type under external load.

Figure E. 10. Strain measurements at location ZA on the fracture side by specimen and fracture repair type under external load.
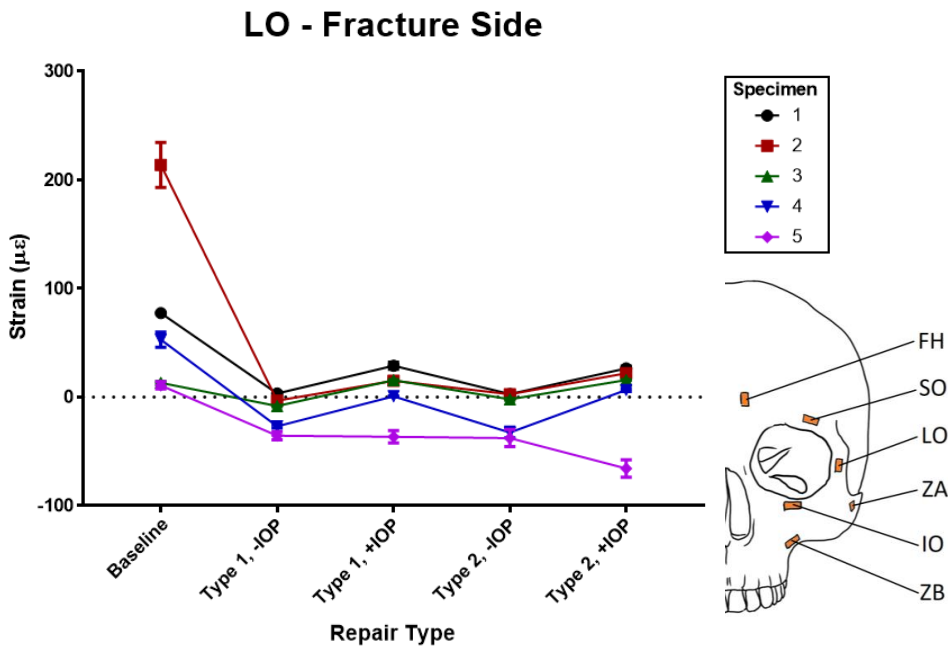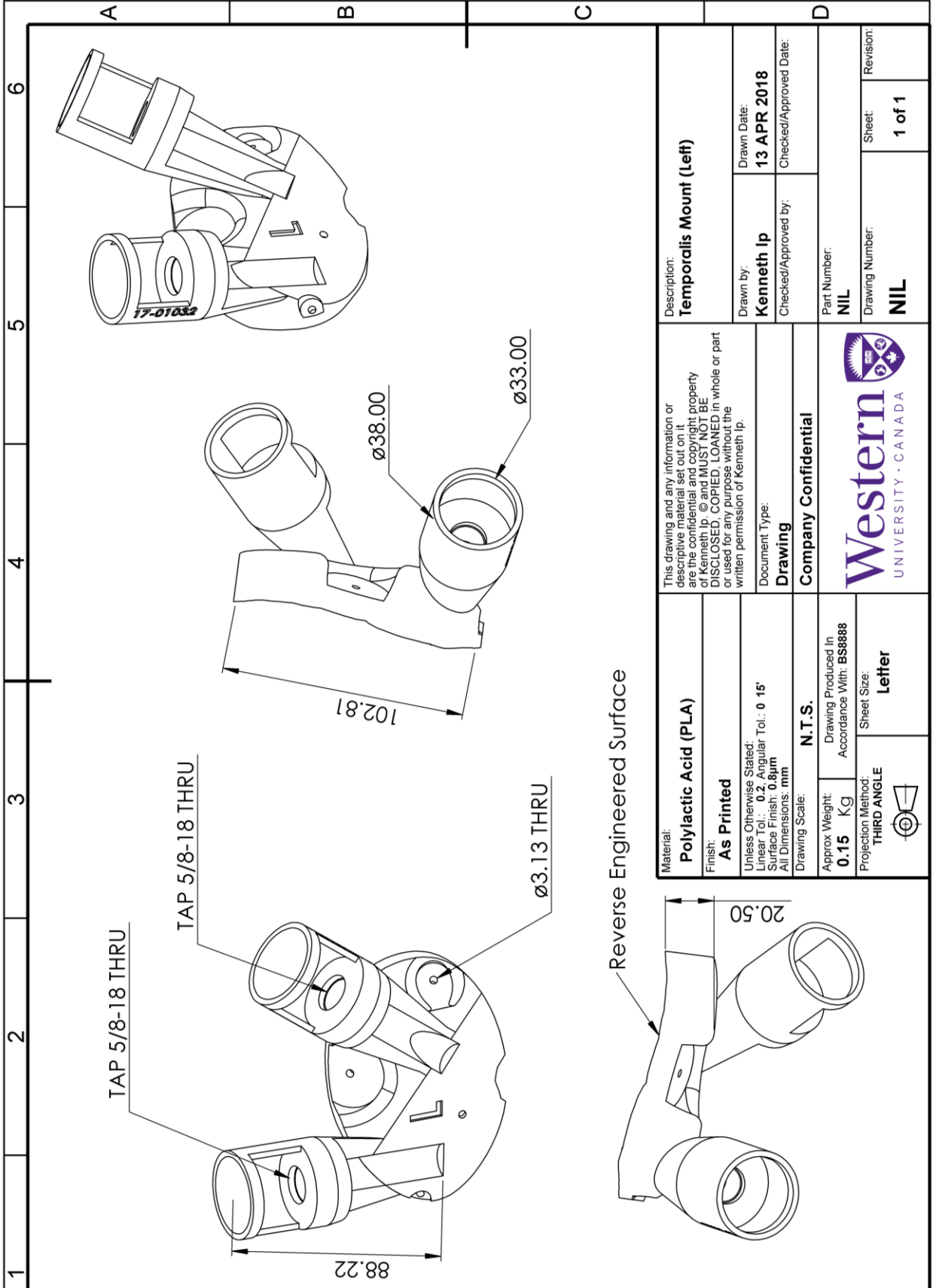
Figure E. 11. Strain measurements at location LO on the intact side by specimen and fracture repair type under external load.

Figure E. 12. Strain measurements at location LO on the fracture side by specimen and fracture repair type under external load.
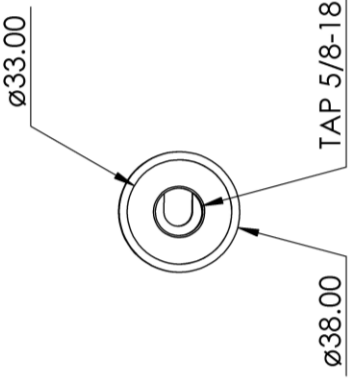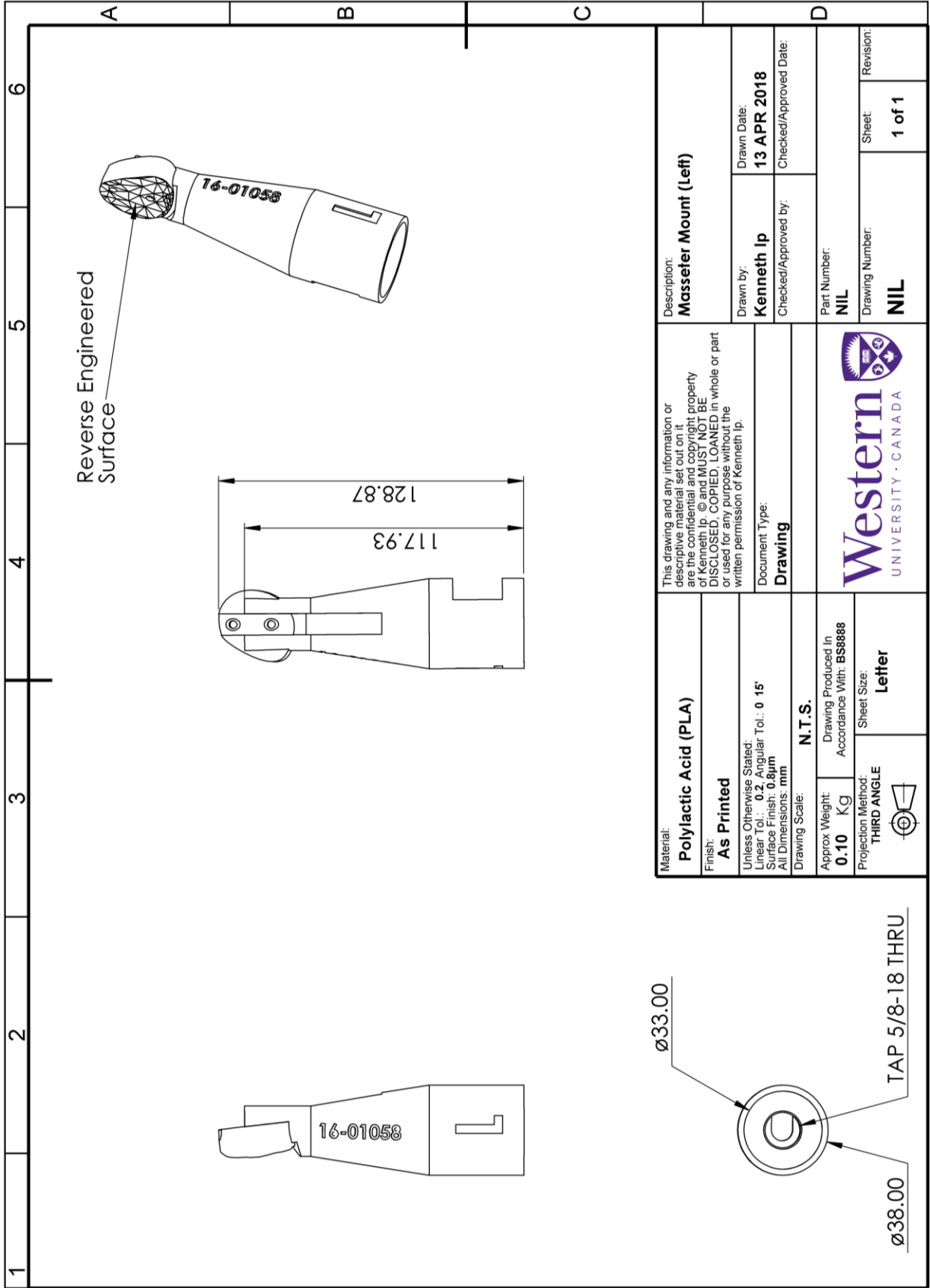
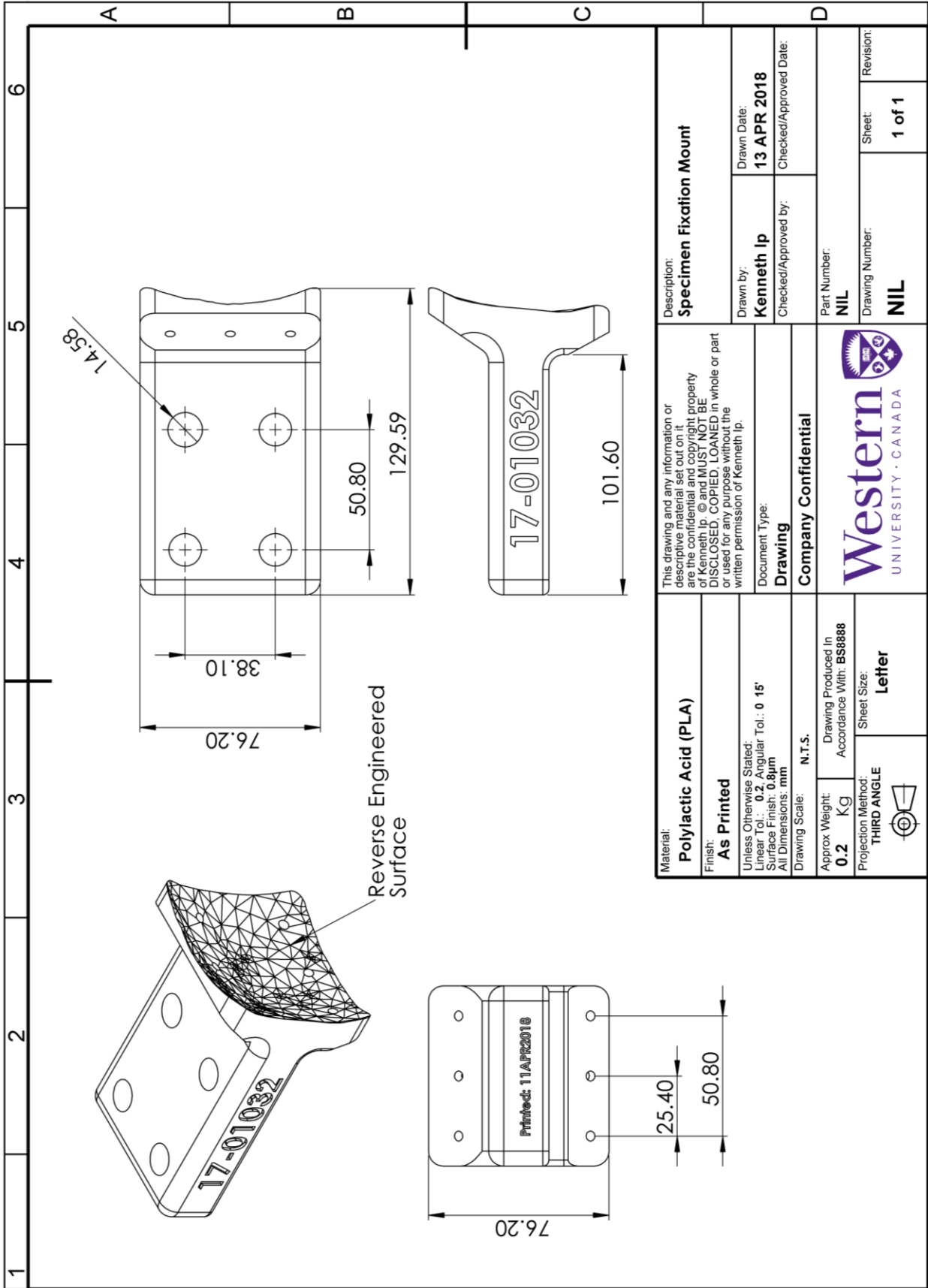# Appendix F: Drawings

(This Page Is Intentionally Left Blank)

TAP 5/8-18 THRU

TAP 5/8-18 THRU

ø3.13 THRU

Reverse Engineered Surface

102.81

ø38.00

ø33.00

88.22

20.50

17-01032

Material:	Description:
Polylactic Acid (PLA)	Temporalis Mount (Left)		
Finish:			
As Printed	Drawn by:	Drawn Date:
Unless Otherwise Stated:	Kenneth Ip	13 APR 2018
Linear Tol.: 0.2 Angular Tol.: 0 15'	Document Type:	Checked/Approved by:	Checked/Approved Date:
Surface Finish: 0.8µm	Drawing	
All Dimensions: mm	Company Confidential		
Drawing Scale: N.T.S.			
Approx Weight:	Drawing Produced In	Part Number:
0.15 Kg	Accordance With: BS8888	NIL
Projection Method:	Sheet Size:	Drawing Number:
THIRD ANGLE	Letter	NIL

This drawing and any information or descriptive material set out on it are the confidential and copyright property of Kenneth Ip, © and MUST NOT BE DISCLOSED, COPIED, LOANED in whole or part or used for any purpose without the written permission of Kenneth Ip.

Western
UNIVERSITY · CANADA

Sheet: 1 of 1

Revision:

Reverse Engineered
Surface

16-01058

16-01058

128.87

117.93

ø33.00

ø38.00

TAP 5/8-18 THRU

Material:
Polylactic Acid (PLA)

Finish:
As Printed

Unless Otherwise Stated:
Linear Tol.: **0.2**, Angular Tol.: **0 15'**
Surface Finish: **0.8µm**
All Dimensions: **mm**

Drawing Scale:
N.T.S.

Approx Weight:
0.10 Kg

Drawing Produced In
Accordance With: **BS8888**

Sheet Size:
Letter

Projection Method:
THIRD ANGLE

This drawing and any information or
descriptive material set out on it
are the confidential and copyright property
of Kenneth Ip. © and MUST NOT BE
DISCLOSED, COPIED, LOANED in whole or part
or used for any purpose without the
written permission of Kenneth Ip.

Document Type:
Drawing

Western
UNIVERSITY · CANADA

Description:
Masseter Mount (Left)

Drawn by:
Kenneth Ip

Drawn Date:
13 APR 2018

Checked/Approved by:

Checked/Approved Date:

Part Number:
NIL

Drawing Number:
NIL

Sheet:
1 of 1

Revision:

Reverse Engineered Surface

17-01032

14.58

50.80

129.59

38.10

76.20

101.60

25.40

50.80

76.20

Printed: 11APR2018

Material:		
Polylactic Acid (PLA)		Description:
Finish:		**Specimen Fixation Mount**
As Printed		

Unless Otherwise Stated:
Linear Tol.: **0.2**, Angular Tol.: **0 15'**
Surface Finish: **0.8µm**
All Dimensions: **mm**

Document Type:
Drawing

Drawn by: **Kenneth Ip**
Drawn Date: **13 APR 2018**

Checked/Approved by:
Checked/Approved Date:

Drawing Scale: **N.T.S.**

Company Confidential

Approx Weight: **0.2** Kg

Drawing Produced In Accordance With: **BS8888**

Part Number: **NIL**

Projection Method: **THIRD ANGLE**

Sheet Size: **Letter**

Drawing Number: **NIL**

Sheet: **1 of 1**

Revision:

This drawing and any information or descriptive material set out on it are the confidential and copyright property of Kenneth Ip. © and MUST NOT BE DISCLOSED, COPIED, LOANED in whole or part or used for any purpose without the written permission of Kenneth Ip.

Western
UNIVERSITY · CANADA

Kenneth Ip
MESc Candidate

Curriculum Vitae

EDUCATION

2016 –
Candidate for MESc (Biomedical Engineering)
Expected: 2018
Supervisors: Dr. Louis Ferreira, Dr. Corey Moore
The University of Western Ontario, London Canada

2013 – 2016
BESc (Mechanical Engineering)
Graduated with Distinction
The University of Western Ontario, London Canada

POSITIONS

2016 –
The University of Western Ontario, London Canada
Research Assistant to Dr. Louis Ferreira
Project: Temporomandibular Force Simulator

2014
The University of Western Ontario, London Canada
Research Assistant to Dr. Eric Savory
Summer research project on bio-deterioration of building walls

2013
Agriculture and Agri-Food Canada, Harrow Canada
Research Assistant to Dr. Xiuming Hao
Co-op research project on LED lighting in greenhouse

HONOURS AND AWARDS

2017
Ontario Graduate Scholarship (OGS), C$15,000
Province of Ontario

2016
Otolaryngology Graduate Research Stipend (OGReS), C$15,000
The University of Western Ontario

2016 – 2018
Western Graduate Research Scholarship (WGRS)
The University of Western Ontario

2015
Faculty Association Scholarship, C$1,000
University of Western Ontario Faculty Association

2013 – 2015
Queen Elizabeth II Aiming for the Top Scholarship
Province of Ontario

PUBLICATIONS AND PRESENTATIONS

Proceedings of Refereed Conferences

1. **Ip KKC**, You P, Knowles NK, Moore CC, Ferreira LM. Development of an In-vitro Intrinsically Loaded Temporomandibular Force Simulator and Fast Computational Model Based on Method of External Approximation. 15th International Symposium Computer Methods in Biomechanics and Biomedical Engineering. Lisbon, Portugal (2018, Podium)

2. **Ip KKC**, Knowles NK, Ferreira LM. A Comparison of the Mechanical Properties of Trabecular Bone Between Micro-Finite Element and Meshless Models. 3rd Biennial Canadian Bone and Joint Conference. London, Canada (2018, Poster)

Manuscript in Preparation

1. **Ip KKC**, You P, Hosein YK, Moore CC, Ferreira LM. Technical Note – The Development of a Temporomandibular Force Simulator to Study Craniofacial Strain In-Vitro. Journal of Cranio-Maxillo-Facial Surgery.

2. **Ip KKC**, Peng Y, Ferreira LM, Moore CC. *Biomechanical Impact of a Zygoma Complex Fracture using Human Cadaver*.